

The Role of Conformational Dynamics in Ground and Excited Ruthenium(II) Polypyridyl Complexes

by

© Mohammad Aminur Rahman

A thesis submitted to the School of Graduate Studies
in partial fulfillment of the requirements for the degree of

Master of Science

Department of Chemistry

Faculty of Science

Memorial University of Newfoundland

May, 2014

St. John's

Newfoundland

Canada

Abstract

Initially, the fluxional solution dynamics of the terpyridine (tpy) ligand in $[\text{Ru}(\text{bpy}-d_8)_2(\eta^2\text{-tpy})]^{2+}$ were studied by proton NMR spectroscopy, prior to a study of the excited state dynamics. Variable temperature ^1H NMR data reveals that the pendant pyridine ring of the tpy ligand wobbles or rotates rather than undergoing an exchange or tick-tock twist mechanism. Then, the excited state dynamics of $[\text{Ru}(\text{bpy})_2(\eta^2\text{-tpy})]^{2+}$ were studied. Protonation of the pendant pyridine ring of $[\text{Ru}(\text{bpy})_2(\eta^2\text{-tpy})]^{2+}$ demonstrates that intra ligand charge transfer (ILCT) occurs between the pendant pyridine and adjacent bpy ligand in the $[\text{Ru}(\text{bpy})_2(\eta^2\text{-tpy})]^{2+}$ complex. Thus, addition of trifluoroacetic acid (TFA) results in slight spectral changes which have been assigned to the protonation of the pendant pyridine of $[\text{Ru}(\text{bpy}-d_8)_2(\eta^2\text{-tpy})]^{2+}$. The protonation of the pendant pyridine increases the lifetime from 0.082 ns to 2.6 ns. Mulliken-Hush analysis of the ILCT of $[\text{Ru}(\text{bpy})_2(\eta^2\text{-tpy})]^{2+}$ has been done and compared with that of $[\text{Ru}(\text{bpy})_3]^{2+}$. The value for the electronic coupling element (H_{DA}) for $[\text{Ru}(\text{bpy})_2(\eta^2\text{-tpyH}^+)]^{3+}$ suggests that the electronic coupling between bpy and the pendant pyridine is quite strong.

A preliminary study on photoinduced ligand loss from $[\text{Ru}(\text{bpy})_2(\text{py})_2]^{2+}$ has been made. The photolysis of *cis*- $[\text{Ru}(\text{bpy})_2(\text{py})_2]^{2+}$ in the presence of trifluoroacetic acid, using broad band, white light excitation, leads to a shift in λ_{max} from 458 nm to 472 nm, consistent with a substitution reaction of the pyridine by THF. A flash photolysis study was also performed to investigate the excited state changes of $[\text{Ru}(\text{bpy})_2(\text{py})_2]^{2+}$ in THF.

Acknowledgments

I would first of all like to thank my supervisor Dr. David W. Thompson for giving me the opportunity to join his research group and for his proper guidance, thoughtful suggestions, encouragement and constructive supervision throughout the course of my study and research work. I express my gratitude to my co-supervisor Dr. Peter Pickup for his valuable suggestions during the progress of my dissertation. Thanks to Dr. Erika Merschrod for being my committee member and providing valuable suggestions.

I would also like to thank the Thompson group members both past and present for their help and cooperation. Especially, thanks to Dr. Li Wang for her time spent during the transient absorption experiments. Thank goes to Brent, Prateek, Steve and Alex for their valuable advice every now and then during my research.

I am thankful to Dr. Celine Schneider for helping me with the variable temperature NMR experiments.

I would like to thank the School of Graduate Studies and Department of Chemistry of Memorial University for their financial support.

I am very much pleased and express my heartiest thanks to my wife for her encouragement, patience and care she has shown during the course of my study. I am also grateful to my family members specially, to my parents and mother-in-law for their moral support during the course of my study. Thanks to Murad vai and Jesmin apu for their encouragement.

Finally, thanks to Allah for his blessing.

Dedicated to my Parents

Table of Contents

	Page no
TITLE	i
ABSTRACT	ii
ACKNOWLEDGMENTS	iii
TABLE OF CONTENTS	v
LISTS OF FIGURES	ix
LIST OF TABLES	xvii
LIST OF SCHEMES	xviii
LIST OF ABBREVIATION AND SYMBOLS	xx
Chapter 1 Background Review	1-34
1.1 Introduction	1
1.2 Principle of Photochemical Reactions	3
1.3 Bonding and Electronic Structure	5
1.4 Electronic Spectroscopy	7
1.5 Electronic Structure (Ground State)	10
1.6 Electronic Structure (Excited State)	12
1.7 Excited State Decay	16
1.8 Excited State Reactivity	18
1.9 Non-Radiative Decay	24

1.10	Photoinduced Ligand Loss	29
1.11	Thesis Overview	31
1.12	References	32
Chapter 2	The Fluxional Dynamics of Terpyridine in	
	$[\text{Ru}(\text{bpy}-d_8)_2(\eta^2\text{-tpy})]^{2+}$	35-58
2.1	Introduction	35
2.2	Literature Review	36
2.2.1	Crystal Structures	36
2.2.2	Ground State Solution Structures and Their Dynamics	40
2.3	Objective	49
2.4	Results and Discussion	50
2.4.1	Ground State Dynamics of $[\text{Ru}(\text{bpy}-d_8)_2(\eta^2\text{-tpy})]^{2+}$	50
2.4.2	Protonation of Pendant Pyridine	56
2.5	Conclusion	57
2.6	References	58
Chapter 3	Photoinduced Charge Transfer Dynamics in	
	$[\text{Ru}(\text{bpy}-d_8)_2(\eta^2\text{-tpy})]^{2+}$	59-128
3.1	Introduction and Review	59
3.1.1	Excited State Electron Transfer	59
3.1.2	Limitations of Bimolecular Reactions	61
3.1.3	Energy Transfer	64

3.1.4	Competition between Energy and Electron Transfer	67
3.1.5	Chromophore-Quencher Complexes	68
3.1.6	Ground and Excited State Proton Transfer	73
3.1.7	Proton Coupled Electron Transfer	79
3.2	Thermodynamics of PCET Reactions	86
3.3	Other Excited State Measurements	91
3.4	Effect of Deuteration on Radiative and Non-radiative Decay	92
3.5	Objectives	94
3.6	Results	95
3.6.1	Steady-State Absorption, Emission and Excited State Redox Potentials	95
3.6.2	Photochemistry	101
3.6.3	Time Resolved Spectroscopy	102
3.6.4	Protonation of Pendant Pyridine	104
3.7	Discussion	113
3.7.1	Spectroscopic Analysis	113
3.7.2	Transient Absorption Spectral Analysis	120
3.8	Conclusion	124
3.9	References	125
Chapter 4	Time Resolved Ligand Loss from cis-[Ru(bpy)₂(py)₂]²⁺	129-147
4.1	Introduction	129
4.2	Objectives	138

4.3	Results and Discussion	139
4.3.1	Steady State Absorption	139
4.3.2	Photolysis in THF	141
4.3.3	Charge Transfer	142
4.3.4	Flash Photolysis Study	143
4.4	Conclusion	146
4.5	References	147
Chapter 5	Experimental	148-164
5.1	Review of the Literature	148
5.2	Experimental Section	157
5.3	Sample Preparation	161
5.4	Measurements	162
5.5	References	164
Chapter 6	Future Work	165-166

List of Figures

Figure 1.1	Photosynthesis at the thylakoid membrane	2
Figure 1.2	Schematic representation of electron transfer upon photoexcitation	4
Figure 1.3	Deactivation pathways of excited state molecules in photochemical processes	4
Figure 1.4	Schematic representation of a Jablonski diagram	5
Figure 1.5	Schematic energy-level diagram for octahedral $[M(L)_6]$ where M is a 2 nd row d ⁶ metal center transition metal complex and L is a chromophoric ligand	6
Figure 1.6	Absorption spectrum of $[Ru(bpy)_3]^{2+}$ in CH ₃ CN at 298 (±3) K	7
Figure 1.7	Absorption spectrum of $[Ru(tpy)_2]^{2+}$ in CH ₃ CN at 298 (±3) K	9
Figure 1.8	(A) Octahedral coordinate system for $[M(bpy)_3]^{2+}$ (B) Symmetry coordinate system for $[M(bpy)_3]^{2+}$	10
Figure 1.9	Molecular Orbital Diagram for $[M(bpy)_3]^{2+}$	11
Figure 1.10	Energy level splitting for the ruthenium(II) cation	13
Figure 1.11	a) Electronic structure model for the localized excited state of $[M(bpy)_3]^{2+}$ (M = Fe, Ru, Os) complexes b) Relative energies of the excited and ground state	14
Figure 1.12	Emission spectra of $[Ru(tpy)_2]^{2+}$ as a function of temperature	15
Figure 1.13	Temperature dependence of the decay time of the emission of $[Ru(tpy)_2]^{2+}$	15
Figure 1.14	Energy level splitting for $[Ru(tpy)_2]^{2+}$	16

Figure 1.15	Energy level diagram for $[\text{Ru}(\text{bpy})_3]^{2+*}$	17
Figure 1.16	Molecular orbital diagram of $[\text{Ru}(\text{bpy})_3]^{2+}$	19
Figure 1.17	Redox potential diagram for $[\text{Ru}(\text{bpy})_3]^{2+*}$ in CH_3CN vs SCE	19
Figure 1.18	Molecular model of $[\text{Ru}(\text{bpy}-d_8)_2(2\text{-phenylphen})]^{2+}$	21
Figure 1.19	Arrangement of phenyl substitution in phenanthroline	22
Figure 1.20	Structures of 2-phenyl substituent in Ru(II) complexes	22
Figure 1.21	Temperature dependence of luminescence decay rate constants for $[\text{Ru}(\text{a})(\text{bpy})_2](\text{PF}_6)_2$ (Δ), $[\text{Ru}(\text{b})(\text{bpy})_2](\text{PF}_6)_2$ (\bullet), and $[\text{Ru}(\text{phen})(\text{bpy})_2](\text{PF}_6)_2$ (o)	23
Figure 1.22	Potential energy diagram and associated vibrational wave functions (A) illustrating the effects of energy gap (B) and changes in equilibrium displacement (C) on vibrational wave function overlaps	28
Figure 1.23	Schematic representation of MLCT and dd excited states	30
Figure 2.1	Various bonding modes of terpyridine with metals	35
Figure 2.2	ORTEP view for (a) $[\text{Ru}(\text{bpy})_3]^{2+}$, (b) $[\text{Ru}(\text{tpy})_2]^{2+}$ and (c) $[\text{Ru}(\text{bpy})_2(\eta^2\text{-tpy})_2]^{2+}$ unit	38
Figure 2.3	“Tick-tock twist” mechanism	40
Figure 2.4	Isokinetic plot for $[\text{Re}(\text{CO})_3(\eta^2\text{-tpy})\text{Cl}]$ (1), $[\text{Re}(\text{CO})_3(\eta^2\text{-tpy})\text{Br}]$ (2), $[\text{Re}(\text{CO})_3(\eta^2\text{-tpy})\text{I}]$ (3), $[\text{W}(\text{CO})_4(\eta^2\text{-tpy})]$ (4), $[\text{PtMe}_3(\eta^2\text{-tpy})\text{Cl}]$ (5), $[\text{PtMe}_3(\eta^2\text{-tpy})\text{Br}]$ (6), $[\text{PtMe}_3(\eta^2\text{-tpy})\text{I}]$ (7),	42

	[Mo(CO) ₄ (η^2 -tpy)] (8) and [Ru(CO) ₂ (η^2 -tpy)Cl ₂] (9), [Ru(CO) ₂ (η^2 -tpy)Br ₂] (10), [Ru(CO) ₂ (η^2 -tpy)I ₂] (11) complexes	
Figure 2.5	(a) Rotation and (b) Ring wobbling processes	45
Figure 2.6	Structures of substituted 1,10-phenanthroline ligands	46
Figure 2.7	Structure of the protonated [Ru(bpy) ₂ (dpp)] ²⁺ complex	47
Figure 2.8	Overlaid spectra of [Ru(bpy- <i>d</i> ₈) ₂ (η^2 -tpy)][PF ₆] ₂ (brown) and [Ru(bpy) ₂ (η^2 -tpy)][PF ₆] ₂ (blue)	50
Figure 2.9	500 MHz ¹ H NMR spectrum (aromatic region) of [Ru(bpy- <i>d</i> ₈) ₂ (η^2 -tpy)] ²⁺ in CD ₃ CN at 298 K	51
Figure 2.10	Structure of the [Ru(bpy- <i>d</i> ₈) ₂ (η^2 -tpy)] ²⁺ complex	52
Figure 2.11	Variable temperature ¹ H NMR spectra of [Ru(bpy- <i>d</i> ₈) ₂ (η^2 -tpy)] ²⁺ in CD ₃ CN over the temperature range 253-323 K	53
Figure 2.12	Wobbling of the pyridine ring	54
Figure 2.13	Rotation of the pyridine ring	55
Figure 2.14	Protonation of [Ru(bpy- <i>d</i> ₈) ₂ (η^2 -tpy)] ²⁺ with trifluoro acetic acid (TFA)	56
Figure 3.1	Structure of 10-methylphenothiazine (10-MePTZ) and methylviologen (MV ²⁺)	60
Figure 3.2	Parabolic dependence of the ET rate constant on the free energy driving force. The diffusion limit, signified by the horizontal solid line, truncates the parabola	63

Figure 3.3	The Förster mechanism for energy transfer	65
Figure 3.4	The Dexter mechanism for energy transfer	66
Figure 3.5	Structures of ferrocene and their methyl derivatives	68
Figure 3.6	Structure of $[(\text{bpy})_2\text{RuP}_2]^{4+}$ (P = N-Methyl bipyridinium group)	69
Figure 3.7	Structure of $[\text{Ru}(\text{dmb})(\text{bpyCH}_2\text{PTZ})(\text{bpy}(\text{CH}_2)_n\text{-MV})]^{4+}$	70
Figure 3.8	Dyads and Triads where the photosensitizer is $\text{M}(\text{ttpy})_2^{2+}$ (M = Ru, Os). X and Y indicate the groups, PTZ, DPAA, MV^{2+} etc	71
Figure 3.9	Energy-level diagram for the Ru based Fc-P dyads	72
Figure 3.10	Structure of dicarboxylic acid	75
Figure 3.11	Förster cycle	76
Figure 3.12	Structure of $[\text{Ru}(\text{bpy})_2(\text{dpp})]^{2+}$	77
Figure 3.13	Diagram for the PT, ET, and PCET reactions	79
Figure 3.14	Graphical presentations of two paraboloides I_μ and II_ν as a function of the solvent coordinates Z_p and Z_e . $\lambda_{\mu\nu}$ is the reorganization energy and $\Delta G_{\mu\nu}^o$ is the equilibrium free energy difference	83
Figure 3.15	Pourbaix diagram for Ru(IV/III) and Ru(III/II) couples of $[\text{Ru}^{\text{II}}(\text{bpy})_2(\text{py})(\text{H}_2\text{O})]^{2+}$	88
Figure 3.16	Pourbaix diagram for quinone/hydroquinone (Q/H ₂ Q) system	90
Figure 3.17	Quinone/hydroquinone (Q/H ₂ Q) system	90
Figure 3.18	Luminescence decay kinetics for $\text{Ru}(\text{tpy})_2^{2+}$ in a $\text{H}_2\text{SO}_4/\text{H}_2\text{O}$	92

- glass (at 77 K) in the presence of $[\text{Fe}(\text{OH}_2)_6]^{3+}$
- Figure 3.19 Structures for (a) $[\text{Ru}(\text{bpy})_2\text{dpp}]^{2+}$ (b) $[\text{Ru}(\text{bpy})_2(2\text{-phenylphenyl})]^{2+}$ (c) $[\text{Ru}(\text{bpy})_2(6\text{-Mebpy})]^{2+}$ and (d) $[\text{Ru}(\text{bpy})_2(6\text{-bpy-cyclamM})]$ ($M = \text{Ni}^{2+}$ or 2H^+) 95
- Figure 3.20 Overlaid UV-vis absorption spectra of $[\text{Ru}(\text{bpy})_2(\eta^2\text{-tpy})]^{2+}$ (blue) (1.1×10^{-6} M) and $[\text{Ru}(\text{bpy})_3]^{2+}$ (red) (1.3×10^{-6} M) in CH_3CN at 298 (± 3) K. Calculated difference spectrum (black) between $[\text{Ru}(\text{bpy})_3]^{2+}$ and $[\text{Ru}(\text{bpy})_2(\eta^2\text{-tpy})]^{2+}$ is shown in the inset 97
- Figure 3.21 The absorption (blue) and emission (red) spectra of $[\text{Ru}(\text{bpy})_2(\eta^2\text{-tpy})]^{2+}$ in acetonitrile at 298 (± 3) K, under 1 atm Ar 99
- Figure 3.22 Transient Absorption spectrum for $[\text{Ru}(\text{bpy})_2(\eta^2\text{-tpy})]^{2+}$ where $\lambda_{exc} = 405$ nm in CH_3CN at 298 (± 3) K. The spectra have been corrected for the group velocity dispersion 102
- Figure 3.23 Diagram for the excitation and relaxation of $[\text{Ru}(\text{bpy})_2(\eta^2\text{-tpy})]^{2+}$. 103
- Figure 3.24 Emission life time spectrum for $[\text{Ru}(\text{bpy})_2(\eta^2\text{-tpy})]^{2+}$, where $\lambda_{exc} = 365$ nm; $\lambda_{max} = 620$ nm in CH_3CN at 298 (± 3) K 104
- Figure 3.25 UV-vis spectra for $[\text{Ru}(\text{bpy})_2(\eta^2\text{-tpy})](2.49 \times 10^{-5}$ M), before (—) and after (⋯) the addition of two equivalents of TFA; $[\text{TFA}] = 0.1$ M in CH_3CN at 298 (± 3) K, under 1 atm N_2 105
- Figure 3.26 Difference spectrum for $[\text{Ru}(\text{bpy})_2(\eta^2\text{-tpyH}^+)]^{3+}$ relative to $[\text{Ru}(\text{bpy})_2(\eta^2\text{-tpy})]^{2+}$ 106

Figure 3.27	The emission spectra of $[\text{Ru}(\text{bpy})_2(\eta^2\text{-tpy})]^{2+}$ (red) and protonated complex(blue) in acetonitrile at 298 (± 3) K	107
Figure 3.28	Emission life time spectrum of protonated $[\text{Ru}(\text{bpy})_2(\eta^2\text{-tpy})]^{2+}$	108
Figure 3.29	Femtosecond transient absorption of $\text{Ru}(\text{bpy})_2(\eta^2\text{-tpy})^{2+} + 5$ equivalents H^+ in acetonitrile	109
Figure 3.30	(A) Femtosecond transient absorption of $[\text{Ru}(\text{bpy})_2(\eta^2\text{-tpy})]^{2+}$ in acetonitrile (blue line) and femtosecond transient absorption of $[\text{Ru}(\text{bpy})_2(\eta^2\text{-tpy})]^{2+} + 5$ equivalents H^+ in acetonitrile (purple circle). (B) Kinetic traces at 450 nm of $[\text{Ru}(\text{bpy})_2(\eta^2\text{-tpy})]^{2+}$ (blue) and $[\text{Ru}(\text{bpy})_2(\eta^2\text{-tpy})]^{2+} + 5$ equivalents H^+ (purple)	110
Figure 3.31	(A) Sub-ns transient absorption of $\text{Ru}(\text{bpy})_2(\eta^2\text{-tpy})^{2+} + 5$ equivalents H^+ in acetonitrile. (B) Kinetics at 375 nm and 450 nm	111
Figure 3.32	The effect of configuration interections for the pendant pyridine	117
Figure 3.33	Potential energy surface diagram illustrating the $^3\text{MLCT}$ state	118
Figure 3.34	Potential energy diagram for $[\text{Ru}(\text{bpy})_3]^{2+}$ and $[\text{Ru}(\text{bpy})_2(\eta^2\text{-tpy})]^{2+}$	119
Figure 3.35	Relation between the dihedral angle and the relative coupling	122
Figure 3.36	Structure of a) 4-methy bipyridine and b) 2-(2-pyridyl)pyrazine	123
Figure 4.1	Potential Energy Diagram for $(d\pi)^6$ MLCT excited states	128
Figure 4.2	Electron captured by $[\text{Ru}(\text{bpy})_3]^{2+}$ complex	130
Figure 4.3	Sequential two photo excitation of $[\text{Ru}(\text{bpy})_3]^{2+}$	131

Figure 4.4	Sequential two photo excitation of $[\text{Ru}(\text{bpy})_3]^{2+}$	132
Figure 4.5	Bonding pattern. a) η^1 b) three centered agostic c) π fashion	133
Figure 4.6	Diagram for the ultrafast dynamics of $[\text{Ru}(\text{bpy})_2(\text{CH}_3\text{CN})_2]\text{Cl}_2$ in H_2O	135
Figure 4.7	Diagram for the ultrafast dynamics of $[\text{Ru}(\text{bpy})_2(\text{CH}_3\text{CN})_2]\text{Cl}_2$ in CH_3CN	136
Figure 4.8	Photodissociation Scheme for $\text{cis}-[\text{Ru}(\text{bpy})_2(\text{py})_2]^{2+}$ in H_2O	137
Figure 4.9	Absorption spectrum of $[\text{cis}-[\text{Ru}(\text{bpy})_2(\text{py})_2]^{2+}$ in CH_3CN at 298 (± 3) K	139
Figure 4.10	Absorption spectrum of $[(\text{tpm})\text{Ru}(\text{bpy})(\text{py})]^{2+}$ in CH_3CN at 298 (± 3) K	140
Figure 4.11	Absorption spectra of $[\text{Ru}(\text{bpy})_2(\text{py})_2]^{2+}$; before (black) and after addition of TFA (4 eq)	142
Figure 4.12	Absorption spectra of $[\text{Ru}(\text{bpy})_2(\text{py})_2]^{2+}$; before (black) and after addition of pyridinium ion (pyH^+)	143
Figure 4.13	Exponential decay fit for the kinetic traces of $[\text{Ru}(\text{bpy})_2(\text{py})_2]^{2+}$ in THF	144
Figure 5.1	500 MHz ^1H NMR spectrum (aromatic region) of $\text{bpy}-d_8$ in CDCl_3 at 298 K	149
Figure 5.2	^1H NMR spectrum (aromatic region) of $[\text{Ru}(\text{bpy})_2(\text{py})_2][\text{PF}_6]_2$ in CDCl_3 at 298 K in 500 MHz	152
Figure 5.3	Structure of tpm and its geometry	152

Figure 5.4	^1H NMR spectrum for tris(1-pyrazoyl)methane in CD_3COCD_3	153
Figure 5.5	^1H NMR spectrum (aromatic region) of $[(\text{tpm})\text{Ru}(\text{bpy})(\text{H}_2\text{O})][\text{PF}_6]_2$ in D_2O at 298 K in 500 MHz	155
Figure 5.6	^1H NMR spectrum (aromatic region) of $[(\text{tpm})\text{Ru}(\text{bpy})(\text{py})][\text{PF}_6]_2$ in CD_3COCD_3 at 298 K in 500 MHz	156

List of Tables

Table 1.1	Comparison of Absorption band Energies, Intensity for Ru(II) polypyridyl complexes in CH ₃ CN	10
Table 1.2	Molecular orbital scheme analysis for [M(bpy) ₃] ²⁺	12
Table 1.3	Excited state properties of [Ru(bpy) ₃] ²⁺	13
Table 2.1	Selected bond lengths (Å) and bond angles for [Ru(bpy) ₃] ²⁺ , [Ru(tpy) ₂] ²⁺ and [Ru(bpy) ₂ (η ² -tpy)] ²⁺	39
Table 2.2	Activation parameters for fluxional tpy for d ⁶ complexes	41
Table 3.1	Absorption maxima for some dyads and triads of [Ru(tpy) ₂] ²⁺ and [Ru(tpy) ₂] ²⁺	71
Table 3.2	Proton Transfer Self-exchange rate constant for selected reactions	74
Table 3.3	Quenching reactions of excited ³ C ₆₀ and [Ru(bpy) ₃] ²⁺	82
Table 3.4	³ MLCT lifetime and k _{nr} values for substituted analogous of [Ru(bpy) ₃] ²⁺	93
Table 3.5	Physical properties of [Ru(bpy) ₂ (L)] ⁿ⁺	96
Table 3.6	Excited State Properties of [Ru(bpy) ₂ (L)] ⁿ⁺ complexes in CH ₃ CN	100
Table 3.7	Photophysical parameters and Radiative and Nonradiative Rate constants for ³ [Ru(bpy) ₂ (η ² -tpy)] ^{2+*} , ³ [Ru(bpy) ₂ (η ² -tpyH)] ^{3+*} and [Ru(bpy) ₃] ^{2+*}	112
Table 3.8	Spectroscopic parameters derived from a Mulliken-Hush analysis of the spectral band envelopes for the Ru→pyH ⁺ and MLCT	115

List of Schemes

Scheme 1.1	Excitation of a donor followed by an electron transfer	1
Scheme 1.2	The excited state dynamics of $[\text{Ru}(\text{bpy})_3]^{2+}$	20
Scheme 3.1	Charge transfer processes in a bimolecular system	59
Scheme 3.2	Electron transfer quenching of $[\text{Ru}(\text{bpy})_3]^{2+}$ (vs SCE in CH_3CN)	60
Scheme 3.3	Quenching of an excited-state via electron transfer	61
Scheme 3.4	The trivial energy transfer mechanism	64
Scheme 3.5	Schematic diagram for the competition of energy and electron transfer processes	67
Scheme 3.6	Energy or electron transfer process in a supramolecular system	70
Scheme 3.7	Mechanism for the proton self-exchange	74
Scheme 3.8	Excited state proton transfer of the carboxylic acid derivatives	77
Scheme 3.9	Excited state protonation of the $[\text{Ru}(\text{bpy})_2(\text{bpz})]^{2+}$ complex	78
Scheme 3.10	Quenching of ${}^3\text{C}_{60}$ in the presence (eq 3.20-3.22) and absence (eq 3.23) of base	80
Scheme 3.11	An example of proton coupled electron transfer	84
Scheme 3.12	HQ^\bullet radical in equilibrium in $\text{CH}_3\text{CN}/\text{H}_2\text{O}$ system	85
Scheme 3.13	H-bonded charge transfer in Hydroquinones	85
Scheme 3.14	Variation of $\text{p}K_a$ value with the change in oxidation number	86
Scheme 3.15	Excited state reaction of the $[(\text{bpy})\text{Re}(\text{CO})_3(\text{MQ}^+)]^{2+}$ complex	87
Scheme 3.16	Excited state reaction of 2-naphthol	87
Scheme 3.17	Reactions for Ru(III/II) couples of $[\text{Ru}^{\text{II}}(\text{bpy})_2(\text{py})(\text{H}_2\text{O})]^{2+}$	89

Scheme 3.18	Reactions for Ru(IV/III) couples of $[\text{Ru}^{\text{II}}(\text{bpy})_2(\text{py})(\text{H}_2\text{O})]^{2+}$	89
Scheme 3.19	Photoinduced ligand substitution reaction	101
Scheme 3.20	Proposed mechanism for the protonated excited state of $[\text{Ru}(\text{bpy})_2(\eta^2\text{-tpy})]^{2+}$	121
Scheme 4.1	Photosubstitution reaction of pyridine with H_2O	134
Scheme 4.2	Photosubstitution reactions of $[\text{Ru}(\text{bpy})_3]^{2+}$ and $\text{Ru}(\text{bpz})_3^{2+}$	135
Scheme 4.3	Photosubstitution reaction of the pyridine by THF	141
Scheme 4.4	Proposed mechanism for the photoinduced ligand loss of $[\text{Ru}(\text{bpy})_2(\text{py})_2]^{2+}$ in THF	145
Scheme 5.1	Preparation of $\text{bpy-}d_8$	149
Scheme 5.2	Preparation of $[\text{Ru}(\text{L})_2\text{Cl}_2]$ (Where L = bpy or $\text{bpy-}d_8$)	150
Scheme 5.3	Preparation of $[\text{Ru}(\text{bpy-}d_8)_2(\eta^2\text{-tpy})]^{2+}$	151
Scheme 5.4	Preparation of $[\text{Ru}(\text{bpy})_2(\text{py})_2]^{2+}$	151
Scheme 5.5	Preparation of tris(1-pyrazolyl)methane (tpm) ligand	153
Scheme 5.6	Preparation of $[(\text{tpm})\text{RuCl}_3] \cdot 1.5\text{H}_2\text{O}$	154
Scheme 5.7	Preparation of $[(\text{tpm})(\text{bpy})\text{RuCl}]\text{Cl} \cdot 2\text{H}_2\text{O}$	154
Scheme 5.8	Preparation of $[(\text{tpm})(\text{bpy})\text{Ru}(\text{H}_2\text{O})][\text{PF}_6]_2$	154
Scheme 5.9	Preparation of $[(\text{tpm})\text{Ru}(\text{bpy})(\text{py})][\text{PF}_6]_2$	155

List of Symbols and Abbreviations

δ	chemical shift (in NMR)
ϵ	molar absorption coefficient (in UV-vis)
λ_{\max}	maximum wavelength
CDCl_3	deuterated chloroform
CD_3CN	deuterated acetonitrile
CD_3COCD_3	deuterated acetone
d	doublet (in NMR)
h or hr	hour
H_2O	water
IR	infrared
K	kelvin
KBr	potassium bromide
L	litre
mg	milligram
M	Molar
MHz	megahertz
nm	nanometre
NMR	nuclear magnetic resonance
ORTEP	Oak Ridge Thermal ellipsoid plot
s	singlet (in NMR)

$^1\text{H NMR}$	proton NMR
t	triplet
m	multiplet (in NMR)
T	temperature
THF	tetrahydrofuran
UV	ultraviolet
VT	variable temperature
CT	charge transfer
ET	electron transfer
D	donor
A	acceptor
A	Absorbance
mM	millimolar
μM	micromolar
bpy	2,2'-bipyridine
tpy	2,2':6,2''-terpyridine
bpy- d_8	deuterated 2,2'-bipyridine
py	pyridine
tpm	tris(1-pyrazoyl)methane
Pd/C	palladium on carbon
k_{nr}	nonradiative decay constant
k_r	radiative decay constant

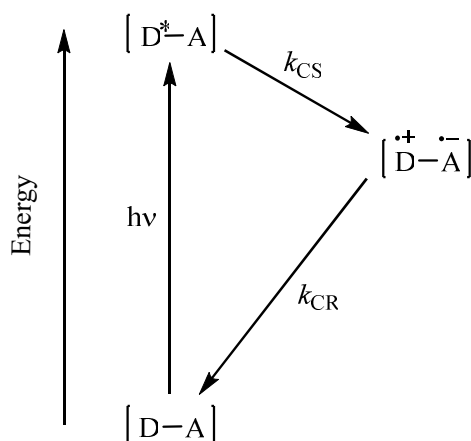
MLCT	metal-to-ligand charge transfer
MC	metal centre
LC	ligand centre
NEt ₃	triethylamine
Na ₂ CO ₃	sodium carbonate
AgNO ₃	silver nitrate
bpy-cyalam	1-(2,2'-bipyridin-6-ylmethyl)-1,4,8,11-tetraazacyclotetradecane

Chapter 1 Background Review

This chapter describes photoinduced electron transfer and its importance; the principles of photochemical reactions; molecular orbital diagrams of transition metal complexes; the photophysical and photochemical behavior of Ru(II) polypyridyl complexes; the energy gap law and the ligand field states of transition metal complexes. These topics are required to understand the role of proton transfer dynamics in ground and excited state Ru(II) polypyridyl complexes, which is the focus of this thesis.

1.1 Introduction

Photoinduced Electron Transfer (PET) reactions form the mechanistic basis of natural photosynthesis and a fundamental understanding of PET is a prerequisite for the development of artificial systems for the conversion and storage of solar energy.¹



Scheme 1.1 Excitation of a donor followed by electron transfer.

These PET reactions involve photoexcitation of molecules that can act as both strong oxidizing and reducing species. The free energy change to form $[D^+-A^-]$ is significantly

endogonic ($\Delta G \gg 0$), such that the rate constant for electron transfer is negligible in the ground state [D-A] adduct (Scheme 1.1). Photon capture by the [D-A] assembly is followed by an electron transfer from an electron donating species (D) to an electron accepting species (A). The photoinduced radical pair may be formed rapidly and efficiently when the quenching process is energetically favored.²

The sun is the main source of energy on the earth. Natural photosynthetic apparatus converts the sun light into chemical energy, where energy and electron transfer processes take place. Figure 1.1 demonstrates a natural photosynthesis system.

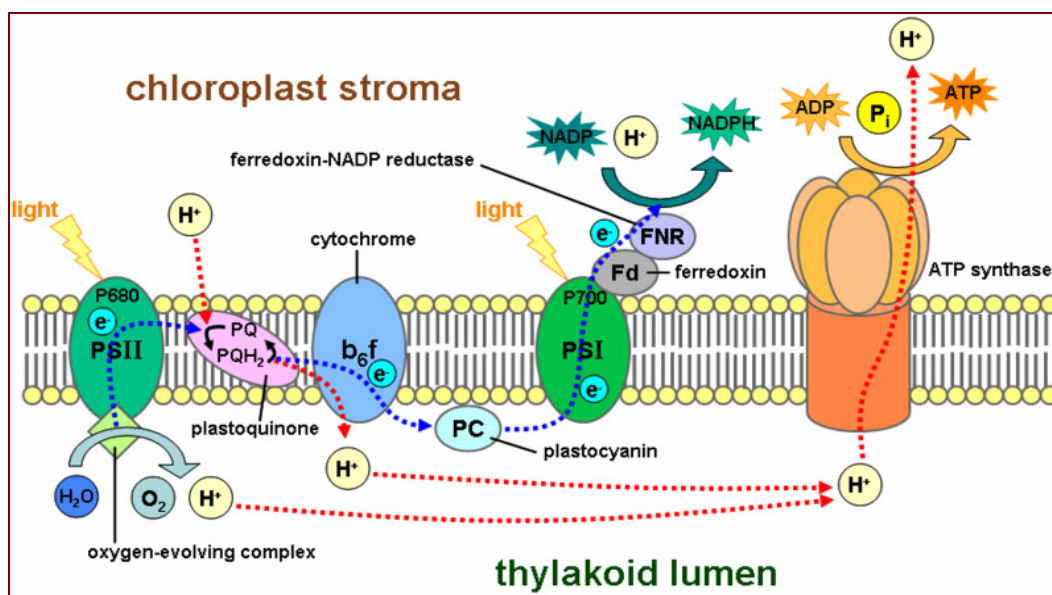


Figure 1.1 Photosynthesis at the thylakoid membrane. (Reprinted with permission from reference 3. Copyright © 2002, John Wiley & Sons, Inc.).

In the first step, sunlight is absorbed by an antenna, consisting of pigments, chlorophylls and carotenoids. This antenna array helps to enhance the light absorbing capacity of the photosynthetic apparatus. Thus, absorption of light and its conversion, results in the formation of molecular excited states. In a short time, the energy is

transferred between the chromophores and eventually reaches the reaction center. Consequently, the light energy is converted into chemical energy by multiple electron transfer steps in the reaction center.⁴ However, it is both difficult and challenging to design artificial photosynthetic assemblies similar to that of natural photosynthesis. Artificial photosynthesis is a concept to mimic the photosynthesis of plants and other photosynthetic organisms. In order to construct an efficient artificial photosynthetic device many points have to be considered, such as the efficiency of the device to collect light, conversion of light into chemical energy and transportation of that energy to where the reaction will take place. Moreover, the effectiveness of the artificial device depends on the donor-acceptor distance, orientation of the molecular orbitals, and excited state life time of the chromophores. Considering the vital role of electron-transfer (ET) in many processes and in photochemical applications it is very important.⁵

1.2 Principles of Photochemical Reactions

The most important part in a photophysical or photochemical process is the absorption of light by a molecule that usually generates an excited state species, which possesses a different electronic structure to the ground state species. For a two state system, the excited state of the molecule always remains higher in energy than the ground state. The interaction of the oscillating electric fields of the incident light interact with the electron density of the molecule and result in a redistribution of electron density of the ground state molecule thereby forming an excited state species, Figure 1.2.

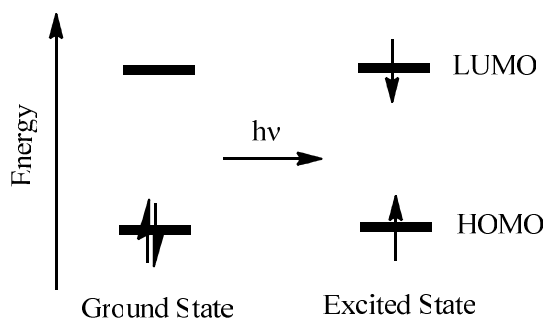


Figure 1.2 Schematic representation of electron transfer upon photoexcitation.

The excited electronic state that is formed, has an increased energy content and can undergo deactivation in a variety of different ways such as; photochemical reactions; radiationless deactivation; emission of light (luminescence); and other quenching processes to reform the ground state (Figure 1.3).⁶

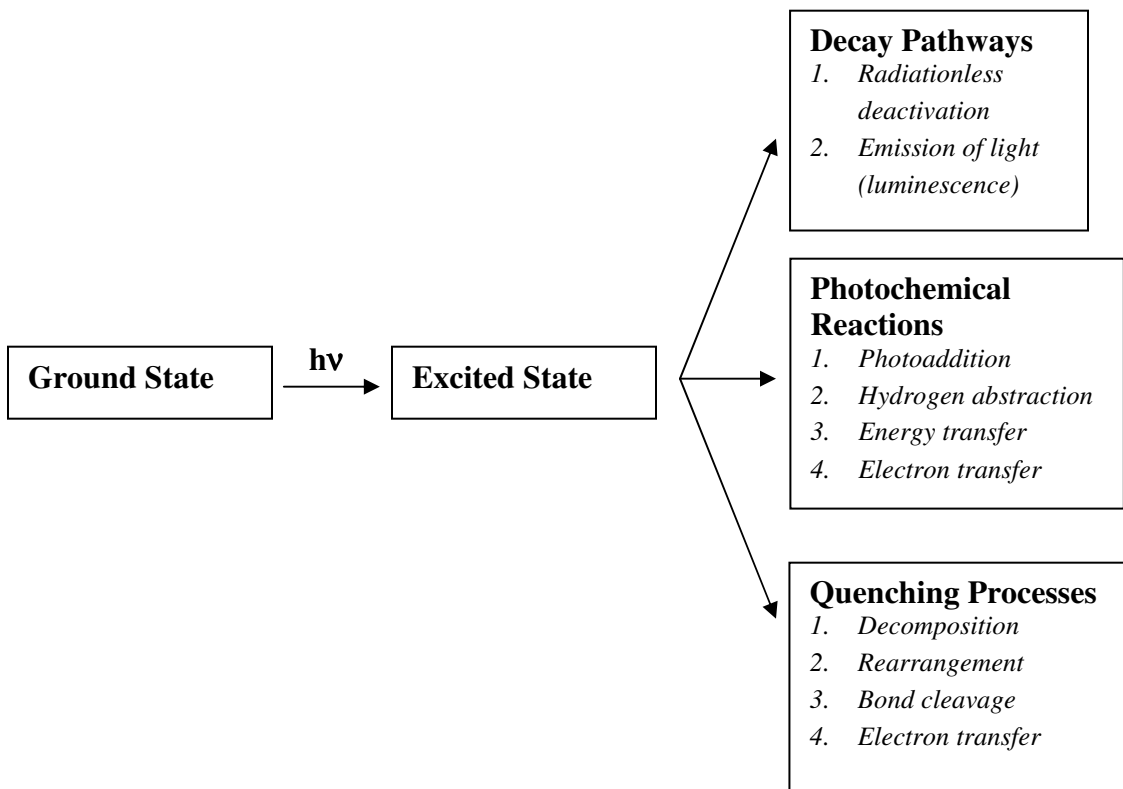


Figure 1.3 Deactivation pathways of excited state molecules in photochemical processes.⁶

The excited state intramolecular dynamics are illustrated by the Jablonski diagram shown in Figure 1.4.⁶ In the absence of spin orbit coupling, three states are involved in a photochemical process (the ground state, singlet excited state and triplet excited state). The lowest excited state (triplet) cannot be directly populated by light absorption as spin must be conserved during absorption of a photon. However, it can be indirectly populated via partial deactivation of a singlet excited state. The diagram shows various deactivation processes, where k_f , k_{ic} , k_{isc} , k_p and k'_{isc} are the rate constants for fluorescence, internal conversion, $S_1 \rightarrow T_1$ intersystem crossing, phosphorescence and $T_1 \rightarrow S_0$ intersystem crossing, respectively.⁶

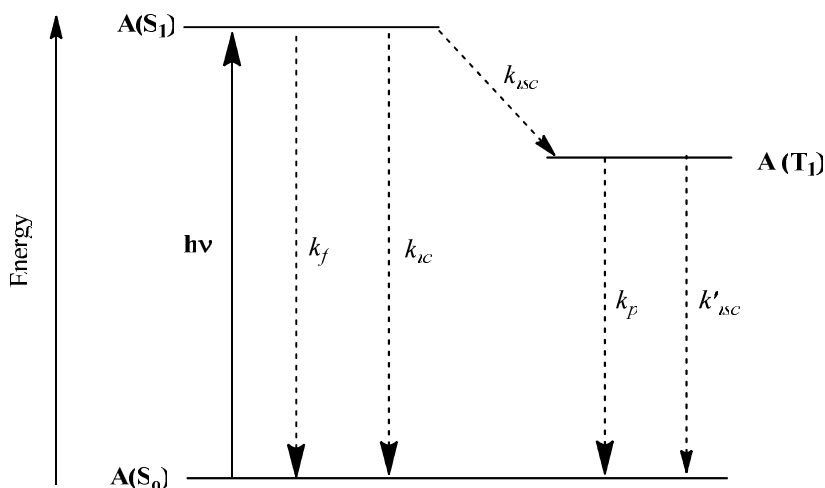


Figure 1.4 Schematic representation of a Jablonski diagram.⁶

1.3 Bonding and Electronic Structure

Transition metal complexes consist of metal ions and ligands. To understand the spectroscopic, redox and kinetic properties of transition metal complexes it is convenient to consider a schematic molecular orbital diagram as shown in the Figure 1.5.

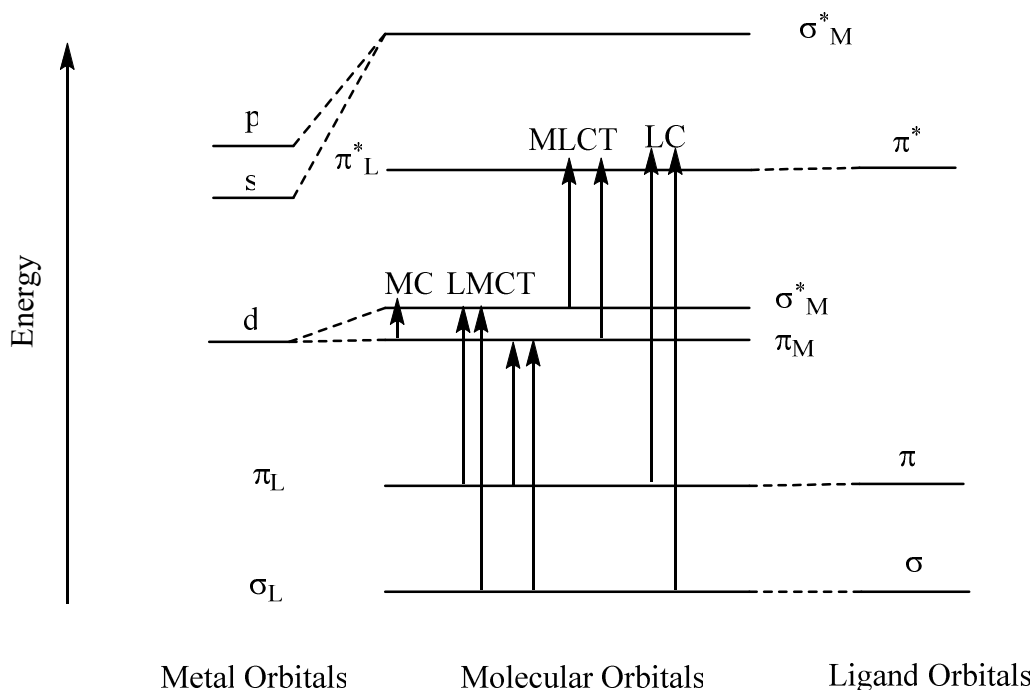


Figure 1.5 Schematic energy-level diagram for an octahedral $[M(L)_6]$ where M is a 2nd row d^6 metal center transition metal complex and L is a chromophoric ligand.⁷

As illustrated in Figure 1.5, the σ and π bonding orbitals of the ligands have lower energies than the metal d-orbitals. Combinations of metal and ligand orbitals result in the formation of bonding and antibonding molecular orbitals where the σ_L , π_L and π_M orbitals are entirely filled. However, the higher energy molecular orbitals remain empty. Absorption of light causes changes in population of the higher orbitals through electronic transitions, more accurately a redistribution of electron density. It is well-documented that three primary types of electronic transition occur in transition metal assemblies.⁷ i) Transitions between molecular orbitals localized on the central metal are called metal centered (MC), ligand-field or $d-d$ transitions. ii) Transitions between MOs localized on a ligand are called ligand-centered or intraligand transitions. iii) Transitions between MOs

localized on different parts of the complex, which cause a displacement of electronic charge between the metal and ligands, are called charge-transfer (CT) transitions or ligand-to-metal charge-transfer (LMCT) or metal-to-ligand charge transfer (MLCT) transitions.

1.4 Electronic Spectroscopy

$[\text{Ru}(\text{bpy})_3]^{2+}$ is one of the most studied and most used ruthenium polypyridyl complexes in the field of photochemical and photophysical research.⁸ The absorption spectrum of $[\text{Ru}(\text{bpy})_3]^{2+}$ at room temperature is shown in Figure 1.6.

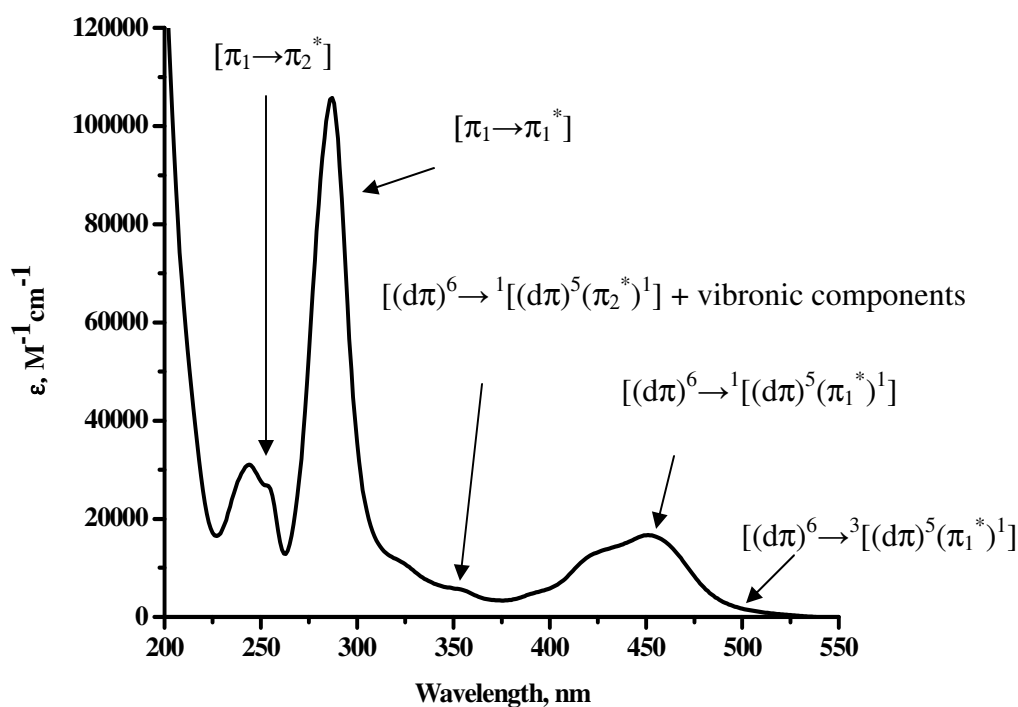


Figure 1.6 Absorption spectrum of $[\text{Ru}(\text{bpy})_3]^{2+}$ in CH_3CN at 298 ± 3 K.

The bands in the UV region at 244 and 287 nm are assigned to ligand-centered $\pi \rightarrow \pi^*$ transitions. The relatively intense and broad absorption band at 450 nm in the visible region is due to spin-allowed metal-to-ligand charge transfer (MLCT) $[(d\pi)^6 \rightarrow {}^1[(d\pi)^5(\pi_1^*)^1]]$ transitions and their vibronic components. The low energy tail is assigned to the $[(d\pi)^6 \rightarrow {}^3[(d\pi)^5(\pi_1^*)^1]]$ transition which arises from a direct MLCT transition from the ground state to the lowest-energy MLCT triplet state to give $[\text{Ru}(\text{bpy})_3]^{2+*}$ by direct excitation. The energy splitting between the lowest singlet and triplet states is 1700 cm^{-1} .^{9c} In addition, one set of MLCT bands appear between 300 to 350 nm. This MLCT is assigned to the π_2^* level on the bpy ligands $[(d\pi)^6 \rightarrow {}^1[(d\pi)^5(\pi_2^*)^1]]$. The presence of spin-forbidden $[(d\pi)^6] \rightarrow {}^3[(d\pi)^5(\pi_1^*)^1]$ transitions in the absorption spectrum of $[\text{Ru}(\text{bpy})_3]^{2+}$ is due to spin-orbit coupling. Spin-orbit coupling mixes orbital and spin character in the electronic wave functions with the extent of singlet character dictating absorptivity.^{9c}

Structurally, $[\text{Ru}(\text{tpy})_2]^{2+}$ is more attractive than $[\text{Ru}(\text{bpy})_3]^{2+}$, considering there is only one isomer for $[\text{Ru}(\text{tpy})_2]^{2+}$.^{9a} The absorption spectrum of $[\text{Ru}(\text{tpy})_2]^{2+}$ has been reported and is shown in Figure 1.7. The very intense bands in the UV region at 308, 270 and 230 nm are assigned to ligand-centered $\pi \rightarrow \pi^*$ transitions. The relatively intense and broad absorption band at 476 nm in the visible region, which is responsible for the deep red color, is due to a spin-allowed metal-to-ligand charge transfer (MLCT) $[(d\pi)^6 \rightarrow {}^1[(d\pi)^5(\pi_1^*)^1]]$ transition. The band envelopes are broad due to many underlying MLCT transitions and their vibronic components.^{9b} The low energy tail is assigned to a $[(d\pi)^6 \rightarrow {}^3[(d\pi)^5(\pi_1^*)^1]]$ transition which is formally spin forbidden, however spin-orbit

coupling mixes the $^1\text{MLCT}$ and $^3\text{MLCT}$ excited states such that the spin selection rule is relaxed. Therefore, the use of spin labels is an approximation.^{9c}

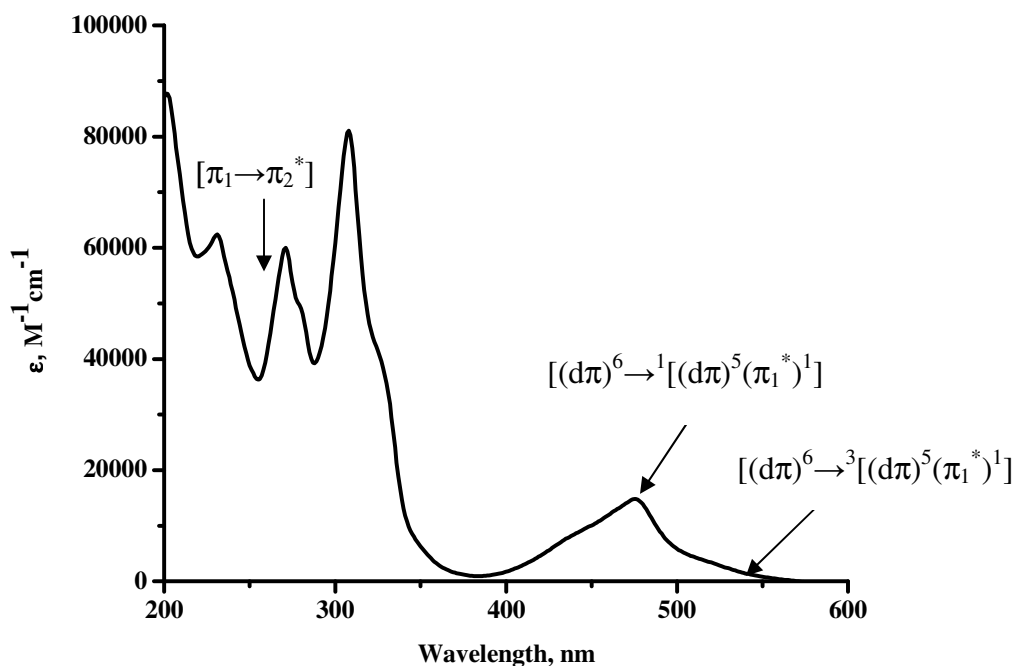


Figure 1.7 Absorption spectrum of $[\text{Ru}(\text{tpy})_2]^{2+}$ in CH_3CN at $298 \pm 3 \text{ K}$.

Comparison of the intensities and energetics for the $[(d\pi)^6 \rightarrow ^1[(d\pi)^5(\pi_1^*)^1]]$ and $[(d\pi)^6 \rightarrow ^3[(d\pi)^5(\pi_1^*)^1]]$ transitions in closely related systems of ruthenium polypyridyl are given in Table 1.1.

Table 1.1 Comparison of absorption band energies and intensities for Ru(II) polypyridyl complexes in CH₃CN

Transitions	$\lambda_{max}(\text{abs}), \text{nm} (\epsilon, \text{M}^{-1}\text{cm}^{-1})$ and Energies (cm^{-1})			
	[Ru(tpy) ₂] ²⁺	[Ru(tpy)(4-Etpy) ₃] ^{2+a}	[Ru(bpy) ₂ (η ² -tpy)] ²⁺	[Ru(bpy) ₃] ²⁺
$(d\pi)^6 \rightarrow {}^1[(d\pi)^5(\pi_1^*)^1]$	476 (14,931) 21010	504 (5,400) ^b 19840	449 (14,086) 22270	451 (16,636) 22170
$(d\pi)^6 \rightarrow {}^3[(d\pi)^5(\pi_1^*)^1]$	520 (3768) 19230	610 (560) ^b 16390	505 (663) 19800	510 (1245) 19608

^a In 4:1 EtOH/H₂O solution; 4-Etpy = 4-ethylpyridine, ^b Reference 9b.

1.5 Electronic Structure (Ground State)

Kober *et al.*^{10a} developed an electronic structure model for the absorption spectra of [M(bpy)₃]²⁺ (M = Fe^{II}, Ru^{II}, Os^{II}), incorporating spin-orbit coupling and assuming single electron transitions between molecular orbitals. The result of the electronic structure model depends on four parameters which were derived for [M(bpy)₃]²⁺ in D₃ symmetry using the coordinates shown in Figure 1.8.

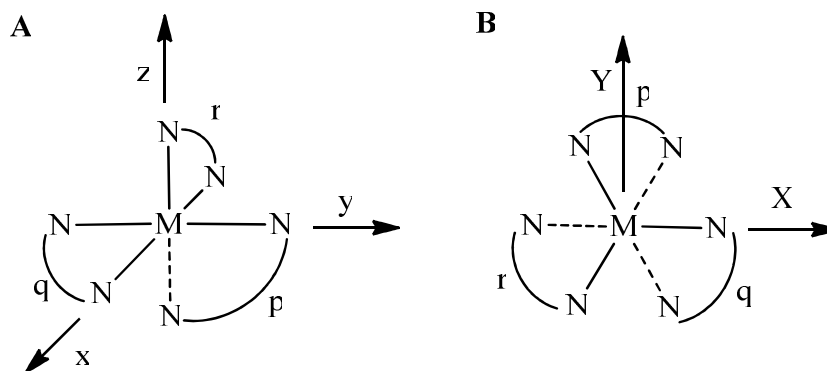


Figure 1.8 (A) Octahedral coordinate system for [M(bpy)₃]²⁺ (B) Symmetry coordinate system for [M(bpy)₃]²⁺. (Adapted from 10a)

The lower case letters x, y and z are assigned to the octahedral axes whereas the upper case letters X, Y and Z are selected as the symmetry axes in the point group of D_3 . The bipyridine ligands are designated by p, q and r. The metal M is in the origin at Z (C_3) symmetry axis which is perpendicular to the plane of the page and goes by the origin point M in the octahedral system.

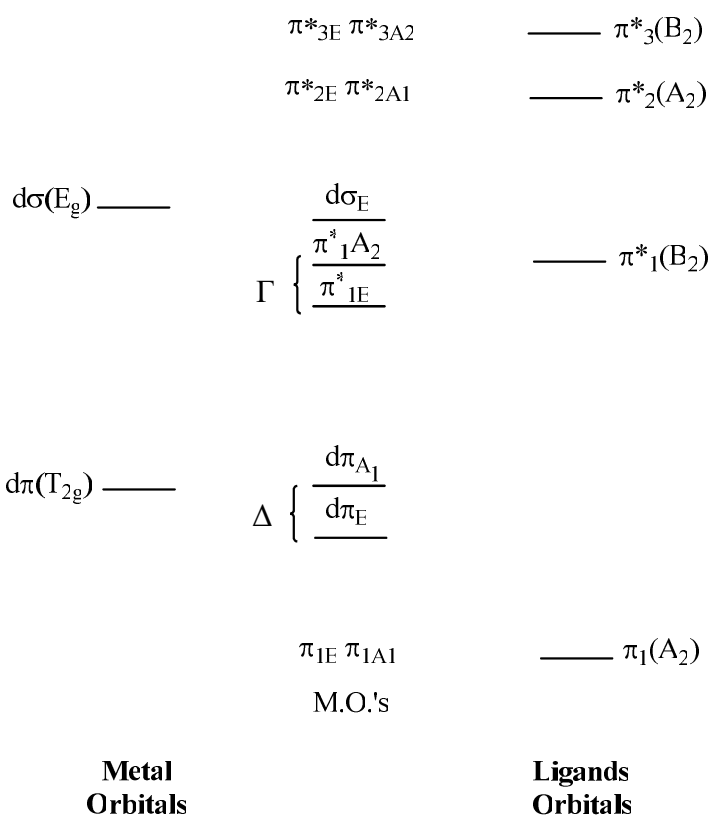


Figure 1.9 Molecular orbital diagram for $[M(\text{bpy})_3]^{2+}$. Δ is positive and Γ is negative. (Adapted from 10a)

The molecular orbital scheme derived from the analysis is shown above, and energetics which include the $d\pi$ splitting (Δ), π^* splitting (Γ), the magnitude of the exchange (K) and spin-orbit coupling (λ) are summarized in Table 1.2.^{10a}

Table 1.2 Molecular orbital scheme analysis for $[M(\text{bpy})_3]^{2+}$

M	Δ	Γ	K	λ^a
Fe ²⁺	100	-1500	800	440
Ru ²⁺	500	-1600	850	1200
Os ²⁺	800	-2100	850	3000

^aThe symbol for spin-orbit coupling is currently ξ

Following $[(d\pi)^6 \rightarrow {}^1[(d\pi)^5(\pi_1^*)]]$ excitation, the electron spin of the excited electron in the π_1^* orbital and the one electron in the $d\pi^5$ manifold will couple to yield a thermally equilibrated triplet excited state. The magnitude of the singlet-triplet splitting is governed by the electron exchange integral K_{nm} given by the following eqn. 1.1:^{10a}

$$K_{nm} = \int d\pi_n(1)\pi_{1m}^*(1) \left(\int \pi_{1m}^*(2)d\pi_n(2) \frac{1}{\Gamma_{12}} d\tau_2 \right) d\tau_1 \quad (1.1)$$

Where the subscripts n and m designate the orbitals where n = A₁, E and m = A₂, E and $d\tau_1$ and $d\tau_2$ are to indicate integration over the electron co-ordinates. The singlet-triplet energy difference E_{ST} ($E_{ST} = 2K_{nm}$) arises from the difference in exchange energies which is $\sim 1700 \text{ cm}^{-1}$.^{10b}

1.6 Electronic Structure (Excited State)

Experimentally, Crosby *et al.*¹⁴ determined the energy level splitting for the lowest excited $d\pi^*$ states for ruthenium(II) cations that range from 18 to 65 cm^{-1} . However, the manifold of ³MLCT states kinetically behave as a single state at 77 K as the states are Boltzmann populated. The ³MLCT excited state is split by low symmetry and spin-orbit coupling into three closely spaced states as shown in Figure 1.10.

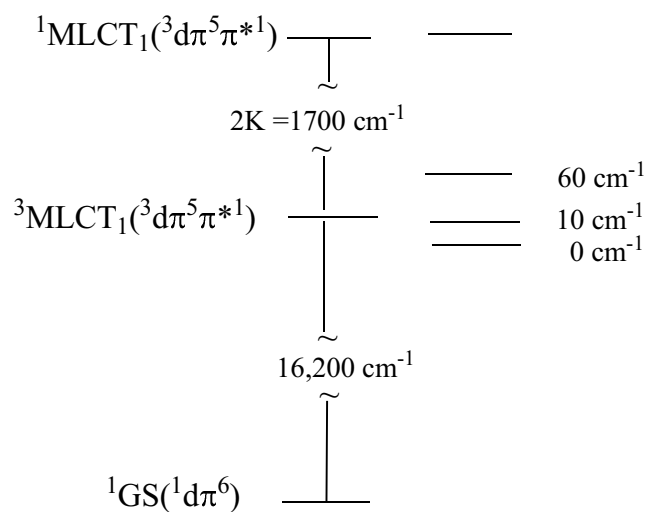


Figure 1.10 Energy level splitting for the ruthenium(II) cation.

Transient IR and transient resonance Raman studies have shown that the excited electron is localized on a single bpy ligand, $[\text{Ru}^{\text{III}}(\text{bpy}^{\bullet-})(\text{bpy})_2]^{2+*}$ rather than delocalized over all three bpy ligand, $[\text{Ru}^{\text{III}}(\text{bpy}^{\bullet-1/3})_3]^{2+*}$ in the thermally equilibrated excited state.¹¹ The excited-state properties of $[\text{Ru}(\text{bpy})_3]^{2+}$ are shown in the Table 1.3.¹⁵

Table 1.3 Excited state properties of $[\text{Ru}(\text{bpy})_3]^{2+}$

State	Energy cm^{-1}	k_{nr}, s^{-1}	k_r, s^{-1}	ϕ_{em}
3	61.2	1.0×10^6	5.9×10^5	0.404
2	10.1	4.1×10^4	1.2×10^4	0.230
1	0	4.8×10^3	9.2×10^2	0.167

Kober *et al.*¹⁵ also developed an electronic structure model for the localized excited states of $[\text{M}(\text{bpy})_3]^{2+}$ (M = Fe, Ru, Os) complexes. The coordinate system used for this analysis is shown in Figure 1.11(a). The promoted electron from the ground state

is considered to exist in the π^* orbital of bpy ligand p, that results in C_2 symmetry of the molecule.

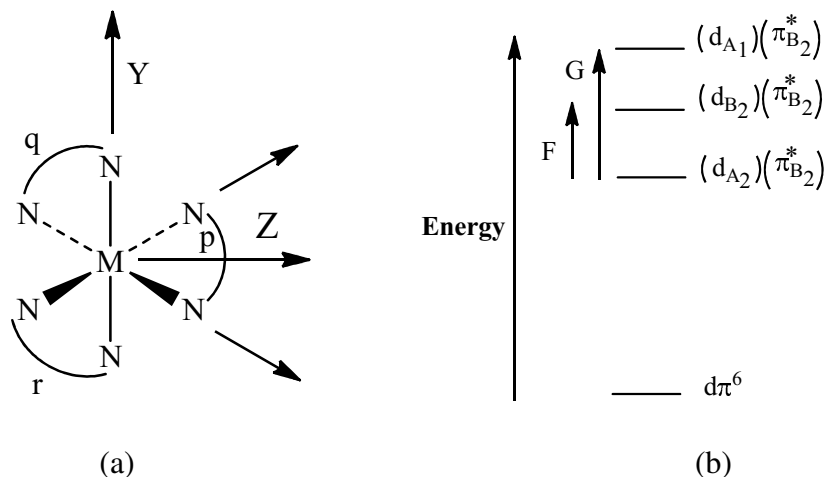


Figure 1.11 (a) Electronic structure model for the localized excited states of $[M(\text{bpy})_3]^{2+}$ ($M = \text{Fe}, \text{Ru}, \text{Os}$) complexes.¹⁵ (b) Relative energies of the $(d\pi)^5(\pi^*B_2)^1$ excited state and the $(d\pi)^6$ ground state. (Adapted from 15)

As an electron is promoted from the $(d\pi)^6$ ground state to the $(d\pi)^5(\pi^*B_2)^1$ excited state, three different configurations of excited states may exist as shown in Figure 1.11(b). Here, F and G are two parameters that describe the relative energies from $(d_{A_2})(\pi_{B_2}^*)$ to $(d_{B_2})(\pi_{B_2}^*)$ and $(d_{A_2})(\pi_{B_2}^*)$ to $(d_{A_1})(\pi_{B_2}^*)$, respectively.¹⁵

At room temperature, solutions of $[\text{Ru}(\text{tpy})_2]^{2+}$ are not luminescent and its excited state life time was reported as 250 ps from transient absorption laser flash photolysis experiments.¹¹ However, at 77 K in a rigid solvent glass matrix $[\text{Ru}(\text{tpy})_2]^{2+}$ exhibits a long-lived luminescence characteristic of a triplet metal to ligand charge transfer ($^3\text{MLCT}$) with $\phi_{\text{em}} = 0.48$ and $\tau = 11.0 \mu\text{s}$. The ϕ_{em} and τ are temperature dependent. As

the temperature increases, from 2 K to 77 K, the luminescence intensity increases (Figure 1.12).¹²

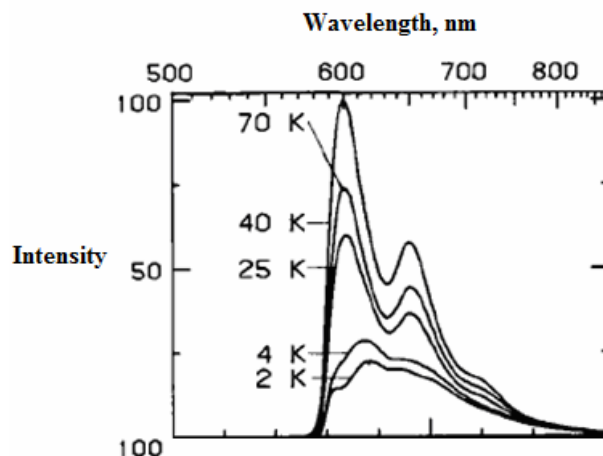


Figure 1.12 Emission spectra of $[\text{Ru}(\text{tpy})_2]^{2+}$ as a function of temperature. (Reprinted with permission from reference 12. Copyright ©1982, Elsevier).

The changes in lifetime with temperature are consistent with triplet MLCT states which kinetically behave as a single MLCT state at 77 K. Fitting the lifetime and temperature data give rise to splitting of the energy-level and intrinsic life-time (Figure 1.13).

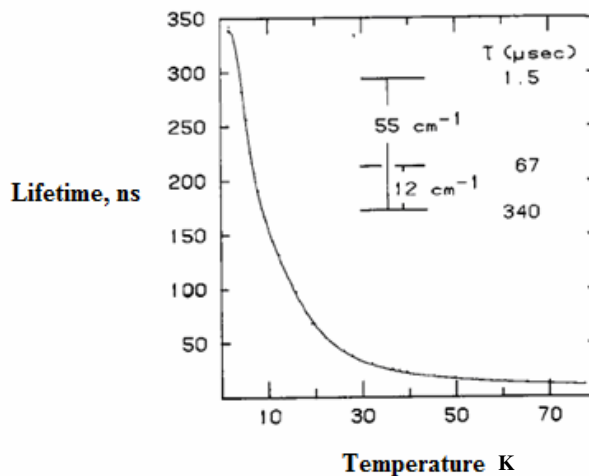


Figure 1.13 Temperature dependence of the decay time of the emission of $[\text{Ru}(\text{tpy})_2]^{2+}$. (Reprinted with permission from reference 12. Copyright ©1982, Elsevier).

The $^3\text{MLCT}$ excited state is split by low symmetry and spin-orbit coupling into three closely spaced states. The energy-level splitting of $[\text{Ru}(\text{tpy})_2]^{2+}$ (12 cm^{-1} , 55 cm^{-1}) with corresponding life-times $340\text{ }\mu\text{s}$, $67\text{ }\mu\text{s}$ and $1.5\text{ }\mu\text{s}$ are shown in Figure 1.14.¹²

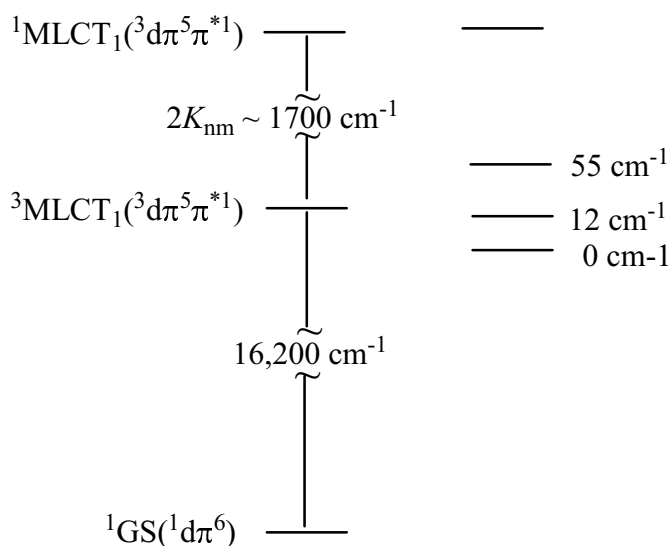


Figure 1.14 Energy level splitting for $[\text{Ru}(\text{tpy})_2]^{2+}$.

The temperature dependence of the emission of $[\text{Ru}(\text{tpy})_2]^{2+}$ from 77 K to 298 K is due to the intervention of the thermally activated $^3\text{MLCT}$ state to $^3[\text{d-d}]$ state interconversion. Meyer *et al.*¹³ suggested that the unfavorable bite angle of the tpy ligand results in a weak ligand field for $[\text{Ru}(\text{tpy})_2]^{2+}$. This situation allows a thermally activated surface crossing into low-lying MC states and also increases the magnitude of k_{nr} .

1.7 Excited State Decay

Light absorption is rapid on the time scale for nuclear motions. Photon capture leads to formation of Franck-Condon excited states. Thus, an excited state formed by

excitation has the electronic coordinates of the excited state but still possesses the nuclear and solvent coordinates of the ground state. Following photon capture, relaxation to the equilibrium nuclear coordinates via vibrational cooling in the excited state manifold occurs in tens of femtoseconds to picoseconds and in picoseconds for the solvent response. The absorption spectrum of $[\text{Ru}(\text{bpy})_3]^{2+}$ is dominated by manifold MLCT and π to π^* absorptions that occur from the singlet ground state, $d\pi^6$, to the lowest lying singlet $^1\text{MLCT}$ excited state which undergoes subpicosecond intersystem crossing to a long-lived $^3\text{MLCT}$ excited state. The dynamics of excited state decay for Ru(II) polypyridyl complexes have been extensively studied. An energy level diagram for $[\text{Ru}(\text{bpy})_3]^{2+*}$ is shown in Figure 1.15.

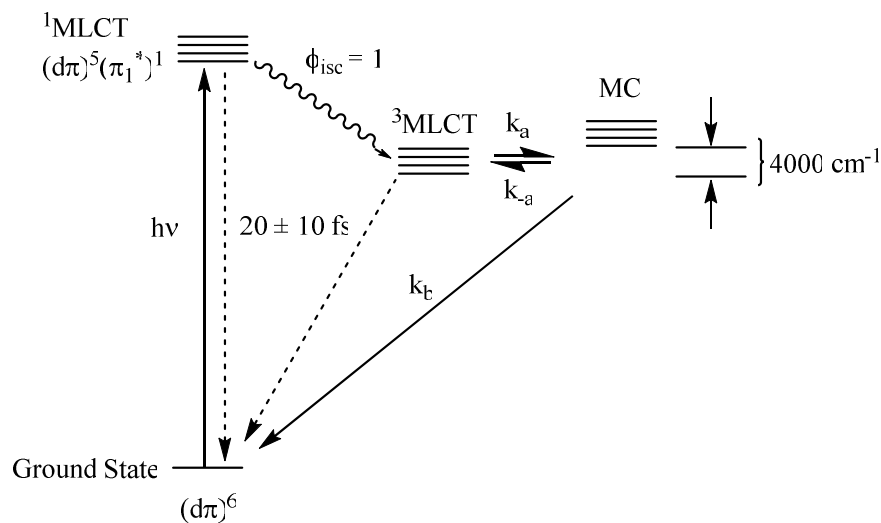


Figure 1.15 Energy level diagram for $[\text{Ru}(\text{bpy})_3]^{2+*}$.¹³

Following the MLCT excitation, the $^1[\text{MLCT}]$ excited state undergoes rapid intersystem crossing ($k_{isc} \sim (20 \pm 15\text{ fs}^{-1})$) to form the vibrationally hot $^3[\text{MLCT}]$ excited states. Thermally activated $^3\text{MLCT} \rightarrow ^3\text{dd}$ transitions are common for ruthenium polypyridyl

complexes. From the temperature dependent life time data it has been observed that for $[\text{Ru}(\text{tpy})_2]^{2+}$, the energy barrier between ^3MC and $^3\text{MLCT}$ states is 1500 cm^{-1} which is significantly smaller than that of 4000 cm^{-1} obtained for $[\text{Ru}(\text{bpy})_3]^{2+}$.¹³

1.8 Excited State Reactivity

Ruthenium(II) polypyridyl complexes are one of the most thoroughly investigated classes of all coordination compounds owing to their extremely rich photophysical and redox properties. They possess an exclusive combination of chemical stability, redox properties, excited state reactivity, luminescence and long excited state lifetimes.⁶ The combination of these properties has given rise to applications of ruthenium(II) polypyridyl complexes as photosensitizers, photocatalysts for the production of hydrogen, and in dye-sensitized solar cells, photon-induced switches, and molecular machines and devices.^{6, 16} For example, the most interesting feature of $[\text{Ru}(\text{bpy})_3]^{2+}$ is the presence of metal-to-ligand charge-transfer (MLCT) bands in the visible region.¹⁷ Here, the electronic transitions occur when an electron is promoted from a metal-based $d\pi$ orbital to a low-lying π^* level on a bpy ligand (Figure 1.16). The electronic structures of the ground and excited states have been described in sections 1.5 and 1.6.

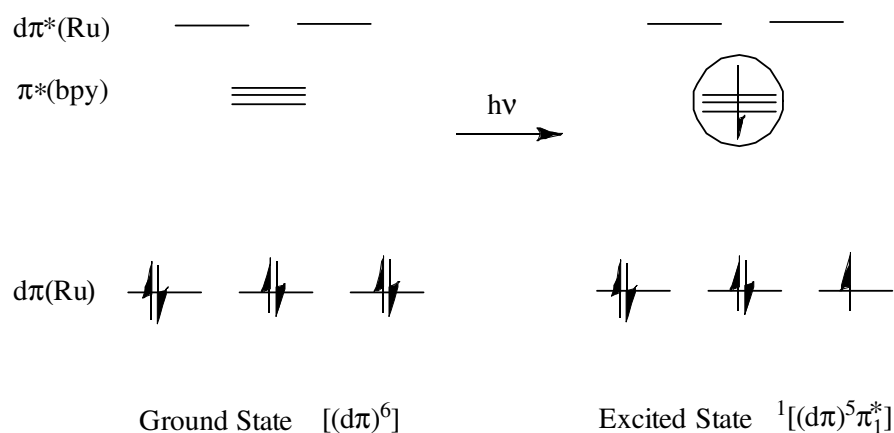


Figure 1.16 Molecular orbital diagram of $[\text{Ru}(\text{bpy})_3]^{2+}$.

$[\text{Ru}(\text{bpy})_3]^{2+}$ is both a good reductant and a good oxidant in its $^3\text{MLCT}$ excited state. The reduction potentials ($E^{o'}$) of $[\text{Ru}(\text{bpy})_3]^{2+*}$ can be calculated by using the following eqn.:^{9c}

$$E^{o'}([\text{Ru}(\text{bpy})_3]^{2+*/+}) = E^{o'}([\text{Ru}(\text{bpy})_3]^{2+/+}) + \Delta G_{\text{ES}}/nF = +0.85 \text{ V} \quad (1.2)$$

$$E^{o'}([\text{Ru}(\text{bpy})_3]^{3+/2+*}) = E^{o'}([\text{Ru}(\text{bpy})_3]^{3+/2+}) - \Delta G_{\text{ES}}/nF = -0.92 \text{ V} \quad (1.3)$$

The $E^{o'}$ values for $[\text{Ru}(\text{bpy})_3]^{2+*}$ in CH_3CN vs SCE are shown in the redox potential diagram in Figure 1.17

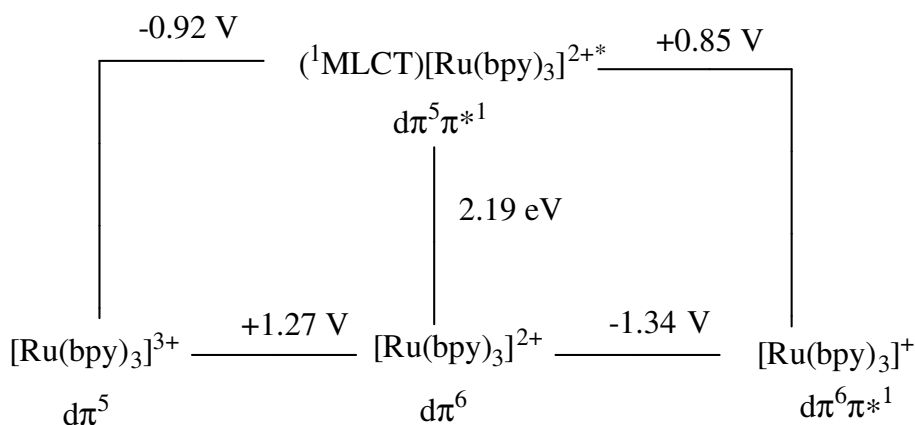
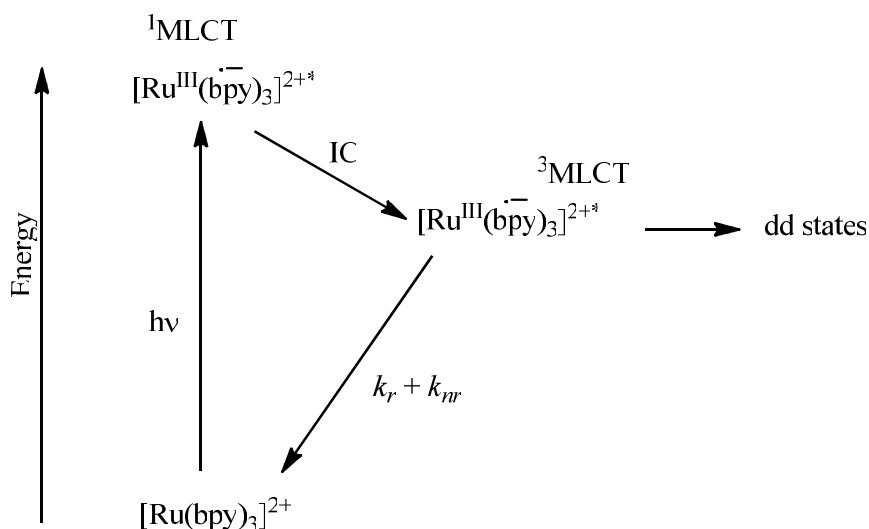


Figure 1.17 Redox potential diagram for $[\text{Ru}(\text{bpy})_3]^{2+*}$ in CH_3CN vs SCE.^{9c}

The redox and excited state properties of $[\text{Ru}(\text{bpy})_3]^{2+}$ can be tuned by synthetic modifications of the ligands or ligand substituents.¹⁸ The $^3\text{MLCT}$ excited state generally decays to the ground state $[\text{Ru}(\text{bpy})_3]^{2+}$ by radiative (k_r) and non-radiative (k_{nr}) processes. The radiative decay (k_r) involves spontaneous emission of a photon of light. Conversely, in non-radiative decay (loss of heat), the energy is distributed through internal molecular vibrations in the molecule by the population of the metal-centred ^3MC , ^3dd , or ligand-field state, which itself is non-emissive and can give rise to ligand loss.

The emission spectrum provides information about the efficiency of excited state formation, lifetime, and on the dynamics of consequent electron transfer events.¹⁹ An alternative deactivation process of the lowest lying $^3\text{MLCT}$ can also occur via metal centered ^3dd excited states. These thermally populated dd states may exist from ps to ns depending on the ligand and lead to the loss of ligands and decomposition of the complex as they are antibonding in nature.²⁰



Scheme 1.2 The excited state dynamics of $[\text{Ru}(\text{bpy})_3]^{2+}$.²⁰

Schmehl *et al.*,²¹ studied phenyl substituted $[\text{Ru}(\text{phen})(\text{bpy}-d_8)_2]^{2+}$ (phen = 1, 10-phenanthroline) complexes (Figure 1.20) which are structurally analogous to $[\text{Ru}(\text{bpy})_2(\eta^2\text{-tpy})]^{2+}$. Investigations on the crystal structures revealed that in Ru(II) complexes having 2-phenyl substituted phen ligands, the phenyl substituents of the phen ligand are oriented nearly perpendicular to the phen ring and π -stack with adjacent coordinated 2,2-bipyridyl ligands (Figure 1.18).

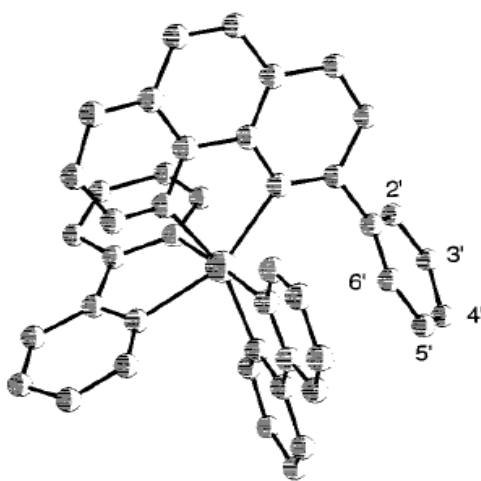


Figure 1.18 Molecular model of $[\text{Ru}(\text{bpy}-d_8)_2(2\text{-phenylphen})]^{2+}$. (Reprinted with permission from reference 21, Copyright © 1999 American Chemical Society).

At room temperature, these complexes (Figure 1.20) are nonluminescent. The temperature-dependent luminescence has been reported and suggests that the non-radiative relaxation in solution is dominated by rapid thermally activated internal conversion from the initially populated $^3\text{MLCT}$ state which decays through a low-lying 3dd state which decays rapidly to the ground state. The arrangement of the phenyl substituent in 2-phenylphen depends on the dihedral angle α . The phenyl group is

coplanar if α is 0° (Figure 1.19 A) and perpendicular if α is 90° (Figure 1.19 B) with phen.²¹

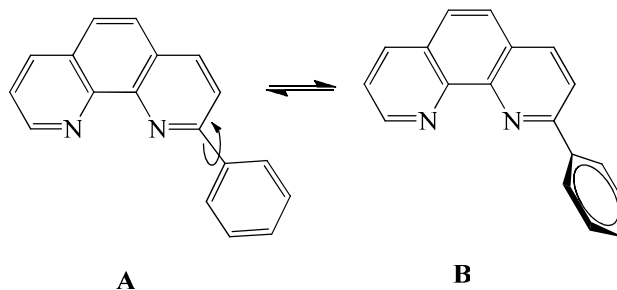


Figure 1.19 Arrangement of phenyl substituents in phenanthroline.

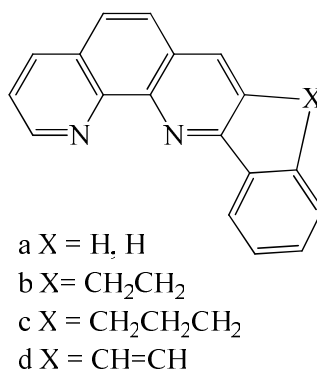


Figure 1.20 Structures of 2-phenyl substituent in Ru(II) complexes.

Room temperature absorption and emission properties for the ruthenium phenanthroline complexes are shown in Table 1.4.²¹

Table 1.4 Photophysical properties of Ruthenium Phenanthroline complexes.²¹

Complex	$\lambda_{\max}(\text{abs})$ nm	$\lambda_{\max}(\text{em})$ nm	ϕ_{em}	$\tau_{\text{em}}(\text{ns})$
[Ru(phen)(bpy) ₂] ²⁺	448	615	0.06	760
[Ru(a)(bpy) ₂] ²⁺	447	622	0.007	5
[Ru(b)(bpy) ₂] ²⁺	447	618	0.003	3
[Ru(c)(bpy) ₂] ²⁺	444	624	0.004	<1
[Ru(d)(bpy) ₂] ²⁺	444			

In CH_3CN solution the complexes have absorption maxima that range from 440 to 450 nm which are due to MLCT charge transfer transitions. The room temperature emission was observed for all the complexes within the range of 610 nm to 625 nm, except $[\text{Ru}(\text{d})(\text{bpy}-d_8)_2]^{2+}$. However, low temperature emission spectra for the ruthenium phenanthroline complexes do not differ much from the parent $[\text{Ru}(\text{phen})(\text{bpy}-d_8)_2]^{2+}$ complex. Hence, the steric and electronic environment introduced by phenyl substitution in the 2-position of the phenanthroline causes only slight changes in the spectroscopic parameters. Conversely, $[\text{Ru}(\text{d})(\text{bpy}-d_8)_2]^{2+}$ with the naphtho-fused phenanthroline derivative and the only ligand with extended unsaturation, behaves differently. The phenyl substituent in $[\text{Ru}(\text{a})(\text{bpy}-d_8)_2]^{2+}$ can rotate freely and allows the optimal π -stacking with the adjacent bpy ligand.

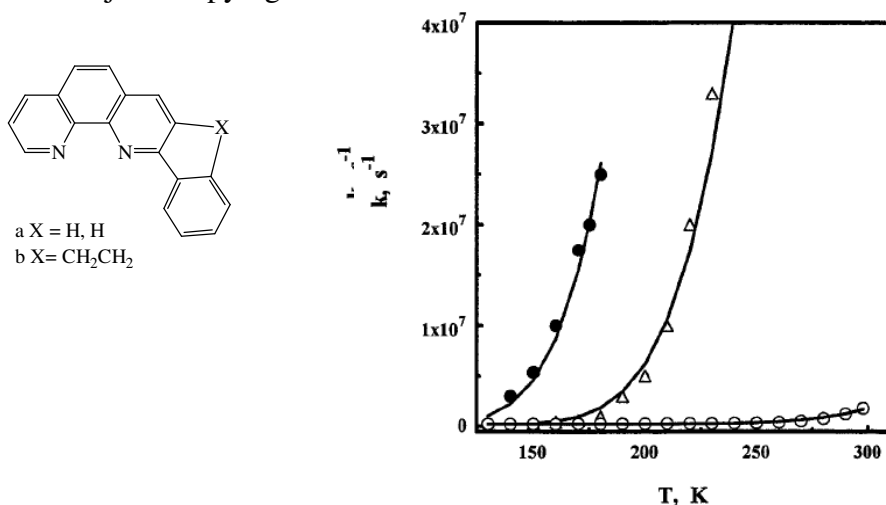


Figure 1.21 Temperature dependence of luminescence decay rate constants for $[\text{Ru}(\text{a})(\text{bpy})_2](\text{PF}_6)_2$ (Δ), $[\text{Ru}(\text{b})(\text{bpy})_2](\text{PF}_6)_2$ (\bullet), and $[\text{Ru}(\text{phen})(\text{bpy})_2](\text{PF}_6)_2$ (\circ). (Reprinted with permission from Reference 21, Copyright © 1999 American Chemical Society).

For other complexes, bridging between the 2-phenyl substituent and the phen hinders the rotation of the phenyl ring and the π -stacking interaction with bpy. The

temperature dependent luminescence study suggests (Figure 1.21) that introduction of phenyl moieties in the 2-position of phen lowers the energy of the LF excited states as the activation barrier for populating the LF state is lowered significantly relative to the parent complex $[\text{Ru}(\text{phen})(\text{bpy}-d_8)_2]^{2+}$.²¹ However, the ability of the 2-phenyl group to π -stack with adjacent bpy ligands serves to stabilize the LF state compared to the complexes having a sterically controlled 2-phenyl substituent.

1.9 Non-Radiative Decay

The photophysical properties of transition metal complexes displaying MLCT excited states are dominated by non-radiative decay processes.²² According to the energy gap law, the non radiative decay rate (k_{nr}) is found to decrease exponentially with increasing emission energy for a homogenous series of complexes. That increasing the energy gap for the $^3\text{MLCT} \rightarrow$ ground state transition results in attenuation of k_{nr} is counterintuitive. However, complexes with low energy absorption bands are weak emitters with short-lived excited states and high energy emitters possess longer lifetimes within a series of structurally related complexes. The idea of the energy gap law is quantified by the application of the Fermi Golden Rule given by the following eqn. (1.4):^{22d}

$$\langle \omega \rangle = \langle \psi'_{\text{el}} | e \sum \vec{r} | \psi_{\text{el}} \rangle^2 \langle \psi'_{\text{vib}} | \psi_{\text{vib}} \rangle^2 \delta(E' - E)(\chi) \quad (1.4)$$

where ω is the probability for the transition and $\delta(E'-E)$ is the Dirac delta function which is required to conserve energy. Application of the Born-Oppenheimer and Condon approximations allows the separation of the electronic (Ψ_{el}) wave functions and

vibrational (Ψ_{vib}) wavefunctions and (Ψ'_{el}) and (Ψ'_{vib}) are electronic and vibration wave function for the excited state, \bar{r} is the Hamiltonian operator which describes the radiative absorption or emission processes. Ψ_{el} also contains the wave functions that govern spin interconversion. It follows from equation (1.5) that the rate constant for the non-radiative decay is given by

$$k_{nr} = 2\pi / \hbar |V_k|^2 (FCWD) \quad (1.5)$$

where V_k is the vibrationally induced electronic coupling matrix element and FCWD is the Franck-Condon weighted density of states that contains the vibrational coupling and energy gap dependence for the $^3\text{MLCT} \rightarrow \text{ground state}$ transition. Assuming a single averaged promoting mode of quantum spacing $\hbar\omega_k$ and Q_k coordinate, V_k is given by

$$\begin{aligned} V_k &= \frac{\hbar}{M_k} \left\langle \Psi_{el,f} \left| \frac{\partial}{\partial Q_k} \right| \Psi_{el,i} \right\rangle \left\langle \chi^{v_{k,f}} \left| \frac{\partial}{\partial Q_k} \right| \chi^{v_{k,i}} \right\rangle \\ &= \frac{\hbar}{M_k^{1/2}} \left\langle \Psi_{el,f} \left| \frac{\partial}{\partial Q_k} \right| \Psi_{el,i} \right\rangle \left(\frac{\hbar\omega_k}{2} \right)^{1/2} = C_k \left(\frac{\hbar\omega_k}{2} \right)^{1/2} \end{aligned} \quad (1.6)$$

The mixing coefficient α , is introduced for a spin state change from triplet to ground state ($^3\text{MLCT} \rightarrow ^1\text{GS}$), which is technically spin forbidden, since spin-orbit coupling mixes singlet character into the spin wave function for the excited state allowing the transition to take place (eqn 1.7)

$$\begin{aligned} &\frac{\hbar}{M_k^{1/2}} \left\langle \Psi_{el,f} \left| \frac{\partial}{\partial Q_k} \right| \Psi_{el,i} \right\rangle \left(\frac{\hbar\omega_k}{2} \right)^{1/2} = \left\langle \Psi_{el,f} \left| \frac{\partial}{\partial Q_k} \right| \Psi_{el,i} \right\rangle \\ &= \alpha \left\langle {}^1\Psi_{el,f} \left| \frac{\partial}{\partial Q_k} \right| \Psi_{el,i} \right\rangle \end{aligned} \quad (1.7a)$$

$$\alpha = \left\langle {}^1\Psi_{el} | H_{SO} | {}^3\Psi_{el} \right\rangle / ({}^1E_{el} - {}^3E_{el}) \quad (1.7b)$$

$$\Psi_{el} = \alpha {}^1\Psi_{el} + (1 - \alpha^2)^{1/2} {}^3\Psi_{el} \quad (1.7c)$$

In the single mode approximation and if the energy gap law is restricted to the condition of $\hbar\omega_k \gg k_B T$ and $|\Delta E| / S\hbar\omega \gg 1$, then k_{nr} is given by eqn. 1.8

$$k_{nr} \approx \frac{\sqrt{\pi}\omega_k C_k^2}{(2\hbar\omega_M |\Delta E|)^{1/2}} \exp(-S_M) \exp\left(-\frac{\gamma|\Delta E|}{\hbar\omega_M}\right) \times \exp(S_o + Z_1 + Z_2) \quad (1.8a)$$

$$Z_1 = S_o \left(\frac{\langle \omega_o \rangle}{\omega_M} \right) (\gamma + 1) \quad (1.8b)$$

$$Z_2 = S_o \left[\left(\frac{\langle \omega_o \rangle}{\omega_M} \right) (\gamma + 1) \right]^2 \left[\exp\left(\frac{\hbar\langle \omega_o \rangle}{k_B T} \right) - 1 \right]^{-1} \quad (1.8c)$$

$$\gamma = \ln\left(\frac{|\Delta E|}{S_M \hbar\omega_M} \right) - 1 \quad (1.8d)$$

Where, ΔE is the internal energy change, $\omega_M (= 2\pi\nu_M)$ is the angular frequency of the acceptor vibration in the ground state, and $S_M = (1/2)\Delta_M^2$ is the electron-vibrational coupling constant or Huang-Rhys factor. Δ_M is the fractional displacement between the thermally equilibrated ground and excited states. $\langle \omega \rangle$ is the mean frequency for coupled low-frequency modes including the surrounding medium. $S_o = (1/2)\Delta_o^2$ is a dimensionless parameter that is related to the vibrational reorganization energy upon formation of the excited state, and Δ_o is the fractional bond displacement change between ground and excited state.²³

In the single-mode approximation, k_{nr} can be written as shown in eqn (1.9) with the parameters E_o , $\Delta v_{0,1/2}$, S_M and $\hbar\omega_M$ available by emission spectral fitting. The energy gap, E_o , is related to the experimentally observed emission energy E_{em} , by $|\Delta E| = E_o + \lambda_{o,L} \approx E_{em} + \lambda_{o,L}$ with the reorganization energy $\lambda_{o,L}$ defined in eqn (1.10)

$$k_{nr} = \frac{\sqrt{\pi}\omega_k C_k^2}{(2\hbar\omega_M E_o)^{1/2}} \exp\left[-S_M - \frac{\gamma E_{em}}{\hbar\omega_M} + \left(\frac{\gamma+1}{\hbar\omega_M}\right)\lambda_{o,L}k_B T\right] \quad (1.9a)$$

$$\gamma = \ln\left(\frac{|E_o|}{S_M \hbar\omega_M}\right) - 1 \quad (1.9b)$$

$$\frac{(\Delta v_{0,1/2})^2}{16 \ln 2} = \lambda_{o,L} k_B T \quad (1.9c)$$

$$\lambda_{o,L} = S_o \hbar \langle \omega_o \rangle \quad (1.10)$$

The logarithm of, k_{nr} is given by the following eqn.

$$\ln k_{nr} = \ln \beta_o + \ln[FC(calc)] \quad (1.11)$$

In a single mode approximation the eqn is

$$\ln k_{nr} = \ln \beta_o - S_M - \frac{\gamma E_o}{\hbar\omega_M} + \left(\frac{\gamma+1}{\hbar\omega_M}\right)\lambda_{o,L}k_B T \quad (1.12)$$

$$\beta_o = \left(\frac{\pi}{2}\right)^{1/2} \omega_k C_k^2 = \frac{\sqrt{2\pi}V_k^2}{\hbar} \quad (1.13)$$

$$\ln[FC(calc)] = -1/2 \ln(\hbar\omega_M E_o) - S_M - \frac{\gamma E_{em}}{\hbar\omega_M} + \left(\frac{\gamma+1}{\hbar\omega_M}\right)\lambda_{o,L}k_B T \quad (1.14)$$

Equation 1.12 is the famous ‘‘energy gap law’’ for excited-state non-radiative decay which relates non-radiative decay dynamics to the energy gap between excited and

ground states.^{22d} At room temperature, excited state decay of polypyridyl complexes is dominated by non-radiative processes where $\phi_{em} \ll 1$. This decay rate constant k_{nr} is related to the energy gap between the ground and excited state. k_{nr} increases as the energy gap decreases. Due to this effect, the compounds with low energy absorption bands usually have short-lived excited states with weak emission. Microscopically, non-radiative decay to a first approximation is a quantum mechanical tunnelling process.²³ The potential energy surfaces are shown in Figure 1.22. The energy gap has an influence over the vibrational overlap between the initial and final states as transfer of the excited electron results in a change in the equilibrium displacement (ΔQ_e) or frequency ($\nu = \omega/2\pi$) between the two electronic states. The rate constant for non-radiative decay (k_{nr}) increases with the increase of vibrational overlap. Figure 1.22 illustrates the influence of the energy gap and change in equilibrium displacement (ΔQ_e) on vibrational overlap. Thus, vibrational overlap and k_{nr} increase with increasing of ΔQ_e .²³

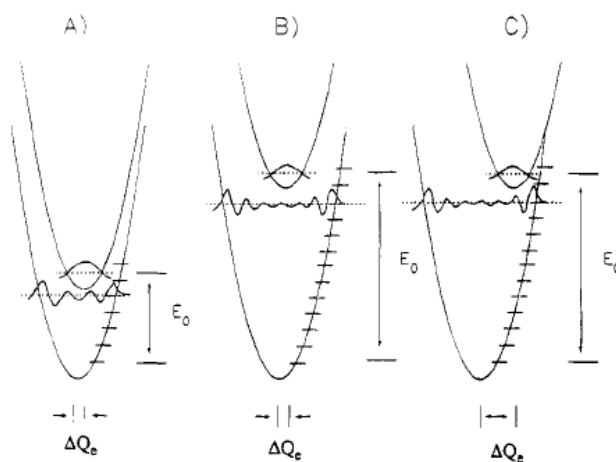


Figure 1.22 Potential energy diagram and associated vibrational wave functions (A) illustrating the effects of energy gap (B) and changes in equilibrium displacement (C) on vibrational wave function overlaps. (Reprinted with permission from reference 23, Copyright © 1995 American Chemical Society).

1.10 Photoinduced Ligand Loss

Photoinduced ligand loss reactions are well-known and have been extensively studied since the pioneering work done by Adamson.²⁴ These types of reactions involve loss of a ligand from a metal complex which can be replaced by a solvent, a counter ion or an added ligand.²⁵ Most ruthenium(II) complexes undergo ligand photolabilization reactions which are attributed to population of ligand field states. It is difficult to quantify the $d-d$ energetics as the transitions are masked by strong charge transfer transitions. The molecular orbital diagram for Ru(II) polypyridyl complexes with octahedral symmetry shows three main types of electronic transitions occurring at low energies. Promotion of an electron from a $d\pi$ metal orbital to a π^* ligand orbital gives rise to a metal-to-ligand charge transfer (MLCT) excited state. The excited states of d^6 octahedral complexes are strongly displaced with respect to the ground state along the metal-ligand vibration coordinates. When the lowest lying excited state is assumed to be a “ 3dd ” state, it is short-lived and undergoes fast radiationless deactivation to the ground state or causes ligand-loss photochemistry (Figure 1.23). As a result the luminescence emission does not decrease with increasing temperature. On the other hand, metal-to ligand charge transfer 3MLCT excited states are not strongly displaced compared to the ground state geometry. When the lowest excited state is 3MLCT , luminescence is observed. However, at high temperature, thermally activated radiationless deactivation via upper lying MC excited states may occur.⁶

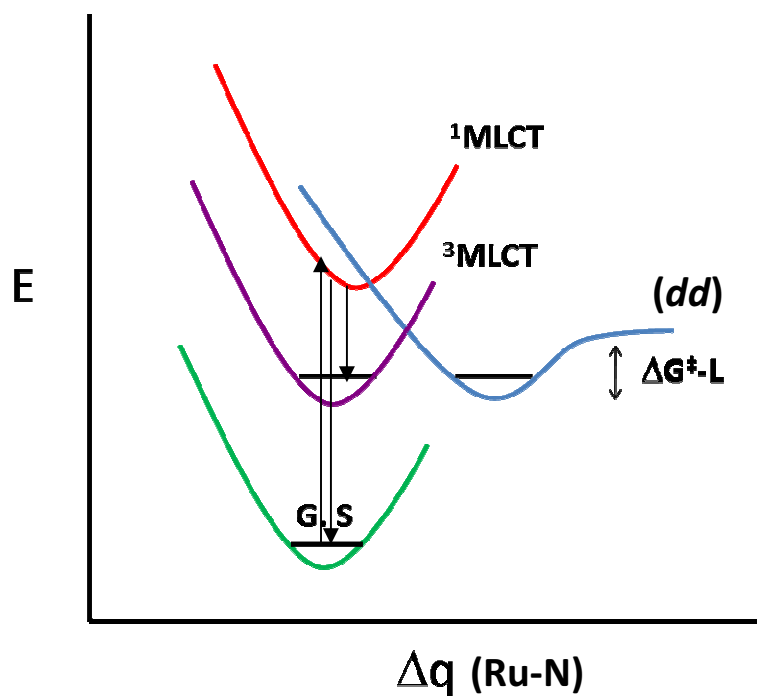


Figure 1.23 Schematic representation of MLCT and *dd* excited states.

The existence of low-lying *dd* states limits the use of polypyridyl complexes of Ru(II) for the studies of photoinduced electron and energy transfer in molecular assemblies in solution. However, complications arising from *dd* states can be avoided in several ways, such as, the use of analogous complexes like those of Os(II) or Re(II). For these metals $10 Dq$ is 20-30% greater than for Ru(II) complexes and *dd* states are not thermally accessible at room temperature or below.²⁶ Moreover, appropriate combinations of ligands can also reduce the *dd*-MLCT energy gap, increasing the MLCT→*dd* barrier. Rigid media such as cellulose acetate, poly(ethylene oxide), zeolites, poly(methyl methacrylate)(PMMA), and SiO₂ sol-gel monoliths are known to inhibit the reactivity of *dd* states.²⁶

1.11 Thesis Overview

This thesis consists of the following five chapters:

This chapter has briefly described an overview; dynamics of excited state processes; photoinduced electron transfer; and photoinduced ligand loss reactions.

Chapter 2 describes the ground state fluxional dynamics of the terpyridine ligand in the $[\text{Ru}(\text{bpy}-d_8)_2(\eta^2\text{-tpy})]^{2+}$ complex which is important to studies of the excited state dynamics of that complex.

Chapter 3 deals with the study of excited state charge transfer dynamics of the $[\text{Ru}(\text{bpy})_2(\eta^2\text{-tpy})]^{2+}$ complex.

Chapter 4 describes preliminary investigations into measuring rate constants for excited-state ligand loss.

Chapter 5 reviews the synthetic chemistry of metal polypyridyl complexes, and provides experimental details for the work described in this thesis.

1.12 References

1. a) Meyer, T. J. *Acc. Chem. Res.* **1989**, *22*, 163; b) Huynh, M. H. V.; Dattelbaum, D. M.; Meyer, T. J. *Coor. Chem. Rev.* **2005**, *249*, 457; b) Wasielewski, M. R. *Acc. Chem. Res.* **2009**, *42*, 60208; c) Carraro, M.; Sartorel, A.; Toma, F. M.; Puntoriero, F.; Scandola, F.; Campagna, S.; Prato, M.; Bonchio, M. *Top Curr Chem.* **2011**, *303*, 121. c) Concepcion, J. J.; House, R. L.; Papanikolas, J. M.; Meyer, T. J. *Proc. Natl. Acad. Sci. USA.* **2012**, *109*, 15560.
2. Gaillard, E. R.; Whitten, D. J. *Acc. Chem. Res.*, **1996**, *29*, 292.
3. Voet, D.; Voet, J. G.; Pratt, C. W. *Fundamentals of Biochemistry*, New York: Wiley, **2002**.
4. a) Sykora, M.; Maxwell, K. A.; DeSimone, J. M.; Meyer, T. J. *Proc. Natl. Acad. Sci. USA.* **2000**, *97*, 7687. b) Ferreira, K. N.; Iverson, T. M.; Maghlaoui, K.; Barber, J.; Iwata, S. *Science* **2004**, *303*, 1831.
5. a) Balzani, V. *Electron Transfer in Chemistry Vol 4*, Wiley-VCH, Weinheim, **2001**. b) Wasielewski, M. R. *Chem. Rev.* **1992**, *92*, 435. c) Gust, D.; Moore, T. A.; Moore, A. L. *Acc. Chem. Res.* **2001**, *34*, 40. d) Arakawa, H.; Aresta, M.; Armor, J. N.; Barteau, M. A.; Beckman, E. J.; Bell, A. T.; Bercaw, J. E.; Creutz, C.; et al. *Chem. Rev.* **2001**, *101*, 953.
6. a) Dixon, I. M.; Lebon, E.; Sutra, P.; Igau, A. *Chem. Soc. Rev.* **2009**, *38*, 1621. b) Lewis, N. S.; Nocera, D. G. *Proc. Natl. Acad. Sci. U. S. A.* **2006**, *103*, 15729. c) Juris, A.; Balzani, V. *Coor. Chem. Rev.* **1988**, *84*, 85.
7. Balzani, V.; Juris, A.; Campagna, M. V.; Serroni, S. *Chem. Rev.* **1996**, *96*, 759.

8. Thompson, D. W.; Fleming, C. N.; Myron, B. D.; Meyer, T. J. *J. Phys. Chem. B* **2007**, *111*, 6930.
9. (a) Fang, Y. Q.; Taylor, N. J.; Hanan, G. S.; Loiseau, F. R.; Passalacqua, R.; Campagna, S.; Nierengarten, H.; Dorsselaer, A. V. *J. Am. Chem. Soc.* **2002**, *124*, 7912. (b) Coe, B. J.; Thompson, D. W.; Culbertson, C. T.; Schoonover, J. R.; Meyer, T. J. *Inorg. Chem.* **1995**, *34*, 3385. (c) Thompson, D. W.; Ito, A.; Meyer, T. J. *Pure Appl. Chem.* **2013** in press.
10. (a) Kober, E. M.; Meyer, T. J. *Inorg. Chem.* **1982**, *21*, 3967. (b) Lever, A. B. P.; Gorelsky, S. I. *Coord. Chem. Rev.* **2000**, *208*, 153.
11. Winkler, J. R.; Netzel, T. L.; Creutz, C.; Sutin, N. *J. Am. Chem. Soc.* **1987**, *109*, 2381.
12. Agnew, S. F.; Stone, M. L.; Crosby, G. A. *Chem. Phys. Lett.* **1982**, *85*, 57.
13. Calvert, J. M.; Caspar, J. V.; Binstead, R. A.; Westmoreland, T. D.; Meyer T. J. *J. Am. Chem. Soc.* **1982**, *104*, 6620.
14. G. D. Hager, G. D.; Crosby, G. A. *J. Am. Chem. Soc.*, **1975**, *97*, 7031.
15. Kober, E. M.; Meyer, T. J. *Inorg. Chem.* **1984**, *23*, 3877.
16. Schramm, F.; Meded, V.; Fliegl, H.; Fink, K.; Fuhr, O.; Qu, Z.; Klopper, W.; Finn, S.; Keyes, T. E.; Ruben, M. *Inorg. Chem.*, **2009**, *48*, 5677.
17. Ballardini, R.; Balzani, V., Credi, A.; Gandolfi, M. T.; Venturi, M. *International Journal of Photoenergy*, **2001**, *3*, 63.
18. Bargawi, K. R.; Llobet, A.; Meyer, T. J. *J. Am. Chem. Soc.*, **1988**, *110*, 7751.
19. Thompson, D. W.; Wishart, J. F.; Brunschwig, B. S.; Sutin, N. *J. Phys. Chem. A*, **2001**, *105*, 8117.

20. a) Crosby, G. A. *Acc. Chem. Res.* **1975**, 8, 231. b) Kalyanasundaram, K. *Coord. Chem. Rev.* **1982**, 46, 159. c) Meyer, T. J. *Pure Appl. Chem.*, **1986**, 58, 1193 d) Thompson, D. W.; Fleming, C. N.; Myron, B. D.; Meyer, T. J. *J. Phys. Chem. B*, **2007**, 111, 6930.
21. Wu, F.; Riesgo, E.; Pavalova, A.; Kipp, R. A.; Schmehl, R. H.; Thummel, R. P. *Inorg. Chem.* **1999**, 38, 5620.
22. a). Caspar, J. V.; Kober, E. M.; Sullivan, B. P.; Meyer, T. J. *J. Am. Chem. Soc.*, **1982**, 104, 630; b) Kober, E. M.; Marshall, J. L.; Dressick, W. J.; Sullivan, B. P.; Caspar, J. V.; Meyer, T. J. *Inorg. Chem.*, **1985**, 24, 2755; c) Kober, E. M.; Caspar, J. V.; Lumpkin, R. S.; Meyer, T. J. *J. Phys. Chem.*, **1986**, 90, 3722. (d) Ito, A.; Meyer, T. J. *Phys. Chem. Chem. Phys.*, **2012**, 14, 13731.
23. Strouse, G. F.; Schoonover, J. R.; Duesing, R.; Boyde, S.; Jones, W. E. Jr.; Meyer, T. *J. Inorg. Chem.*, **1995**, 34, 473.
24. Adamson, A. W. *J. Phys. Chem.* **1967**, 71, 798.
25. Adelt, M.; Devenney, M.; Meyer, T. J.; Thompson, D. W.; Treadway, J. A. *Inorg. Chem.*, **1998**, 37, 2616.
26. Fleming, C. N.; Dattelbaum, D. M.; Thompson, D. W.; Ershov, A. Y.; Meyer, T. J. *J. Am. Chem. Soc.* **2007**, 129, 9622.

Chapter 2 The Fluxional Dynamics of Terpyridine in $[\text{Ru}(\text{bpy-d}_8)_2(\eta^2\text{-tpy})]^{2+}$

This chapter describes the fluxional dynamic behaviour of the terpyridine (tpy) ligand in the $[\text{Ru}(\text{bpy-d}_8)_2(\eta^2\text{-tpy})]^{2+}$ complex. Here, ground state dynamics and fluxional behaviour of tpy in $[\text{Ru}(\text{bpy-d}_8)_2(\eta^2\text{-tpy})]^{2+}$ have been documented as a prelude to the excited state measurements outlined in Chapter 3.

2.1 Introduction

The 2,2':6',2''-terpyridine (tpy) ligand was first isolated by Morgan and Burstall in 1932.¹ Usually, the tpy ligand is chelated in a tridentate fashion when sufficient coordination sites are available on a metal ion. Still, there are some complexes where tpy appears as monodentate, bidentate or as a bridging ligand (Figure 2.1).²

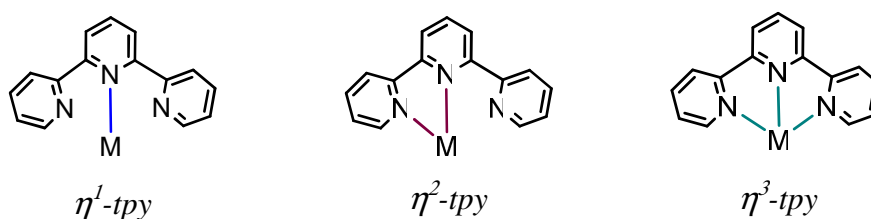
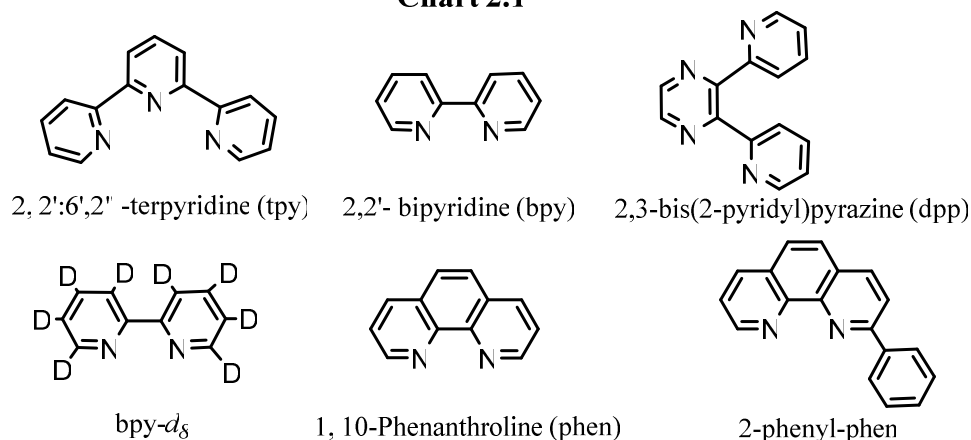


Figure 2.1 Various bonding modes of terpyridine with metals.

Here, the focus of this study will be on complexes where the tpy ligand acts as a bidentate ligand. The structures for the pertinent ligands for the systems discussed in this chapter are given in chart 2.1.

Chart 2.1



2.2 Literature Review

2.2.1 Crystal Structures

Crystal structures for $[\text{Ru}(\text{bpy})_3]^{2+}$, $[\text{Ru}(\text{tpy})_2]^{2+}$ and $[\text{Ru}(\text{bpy})_2(\eta^2\text{-tpy})]^{2+}$ have been published.³ The structures for the $[\text{Ru}(\text{bpy})_3](\text{PF}_6)_2$, $[\text{Ru}(\text{tpy})_2](\text{PF}_6)_2$ and $[\text{Ru}(\text{bpy})_2(\eta^2\text{-tpy})](\text{PF}_6)_2$ salts are shown in Figure 2.2 and pertinent bond lengths (Å) and bond angles (deg) are summarized in Table 2.1.

In $[\text{Ru}(\text{bpy})_3]^{2+}$, the average Ru-N bond distance is 2.056(2) Å. The N-Ru-N' (78.7(1)) and N-Ru-N'' (89.1(1)) bond angles are less than the ideal 90°. ^{3a} However, for N'-Ru-N'' (96.3(1)), the angle is greater than the ideal 90°. The angle N'-Ru-N''' (173.0(1)) is less than the ideal 180°. ^{3a} For $[\text{Ru}(\text{tpy})_2]^{2+}$, ^{3c} the bite angle for N1-Ru-N4 is 78.9°, significantly smaller than an ideal 90° bite. This structural feature has ramifications for non-radiative decay in the excited states of $[\text{Ru}(\text{tpy})_2]^{2+}$ (see below). In the case of $[\text{Ru}(\text{bpy})_2(\eta^2\text{-tpy})]^{2+}$, ^{3b} the Ru-N bond lengths range from 2.052(6) to 2.133(6) Å, longer

than those reported for $[Ru(bpy)_3]^{2+}$ [2.056(2) Å].^{3c} The pendant pyridine is within the Van der Waals contact distance of the adjacent bpy [2.1133(6) Å]. The dihedral angle between the pendant pyridyl substituent is 52.3° relative to the ligated portion of the tpy ligand. The dihedral angle is similar to those of $[Ru(bpy)_2(\text{phen-R})]^{2+}$ complexes [R is an aryl substituent] where the average dihedral angle is 54.6°.⁴ The staggered cofacial arrangement between the pendant pyridyl and adjacent bpy ligand results in a steric interaction giving rise to elongated Ru-N_{bpy} bonds.⁴

Table 2.1 Selected bond lengths (Å) and bond angles for $[\text{Ru}(\text{bpy})_3]^{2+}$, $[\text{Ru}(\text{tpy})_2]^{2+}$ and $[\text{Ru}(\text{bpy})_2(\eta^2\text{-tpy})]^{2+}$.

Selected Bond Length (Å) for $[\text{Ru}(\text{bpy})_3]^{2+}$		Selected Bond Angles (deg) for $[\text{Ru}(\text{bpy})_3]^{2+}$	
Ru-N	2.056(2)	N-Ru-N'	78.7(1)
N-C(1)	1.354(3)	N-Ru-N''	89.1(1)
N-C(5)	1.354(4)	N-Ru-N'''	173.0(1)
C(1)-C(2)	1.369(4)	N'-Ru-N''	96.3(1)
C(1)-C(1')	1.474(4)		
C(1)-C(3)	1.474(5)		
C(1)-C(4)	1.348(5)		
Selected Bond Length (Å) for $[\text{Ru}(\text{tpy})_2]^{2+}$		Selected Bond Angles (deg) for $[\text{Ru}(\text{tpy})_2]^{2+}$	
Ru-N(1)	2.07(1)	N(1)-Ru-N(4)	78.9(4)
Ru-N(4)	1.99(1)	N(4)-Ru-N(7)	79.3(4)
Ru-N(7)	2.05(1)	N(1)-Ru-N(19)	90.0(4)
Ru-N(19)	2.09(1)	N(1)-Ru-N(22)	101.4(4)
Ru-N(22)	1.96(1)	N(1)-Ru-N(25)	93.8(4)
Ru-N(25)	2.07(1)	N(4)-Ru-N(19)	102.7(4)
		N(4)-Ru-N(22)	177.5(4)
		N(4)-Ru-N(25)	98.6(4)
		N(7)-Ru-N(19)	94.2(4)
		N(7)-Ru-N(22)	101.0(4)
Selected Bond Length (Å) for $[\text{Ru}(\text{bpy})_2(\eta^2\text{-tpy})]^{2+}$		Selected Bond Angles (deg) for $[\text{Ru}(\text{bpy})_2(\eta^2\text{-tpy})]^{2+}$	
Ru-N(1)	2.064(6)	N(1)-Ru-N(3)	84.4(2)
Ru-N(2)	2.056(6)	N(1)-Ru-N(5)	97.3(2)
Ru-N(3)	2.088(5)	N(1)-Ru-N(4)	98.4(2)
Ru-N(4)	2.106(6)	N(2)-Ru-N(3)	97.6(2)
Ru-N(5)	2.052(6)	N(2)-Ru-N(5)	88.2(2)
Ru-N(6)	2.133(6)	N(3)-Ru-N(6)	99.8(2)
		N(2)-Ru-N(6)	101.9(2)
		N(4)-Ru-N(5)	95.3(2)
		N(4)-Ru-N(6)	81.3(2)
		N(1)-Ru-N(6)	175.6(2)
		N(1)-Ru-N(2)	78.7(2)

2.2.2 Ground State Solution Structures and Their Dynamics

Abel *et al.* first reported² that bidentate tpy ligands exhibit fluxional behavior. Temperature dependent ^1H NMR studies of the complexes *fac*- $[\text{ReBr}(\text{CO})_3(\eta^2\text{-tpy})]$, *cis*- $[\text{W}(\text{CO})_4(\eta^2\text{-tpy})]$ and *fac*- $[\text{PtClMe}_3(\eta^2\text{-tpy})]$ revealed a dynamic conformation process occurring on the NMR time scale in fluid solution. Analysis of the temperature dependent ^1H NMR data revealed an intramolecular ligand exchange process where the tpy ligand is bound in a bidentate fashion, but oscillates between two equivalent binding modes, through the formation of a seven coordinated transition state, as shown in Figure 2.3. This dynamic process was termed as the “tick-tock twist” mechanism.

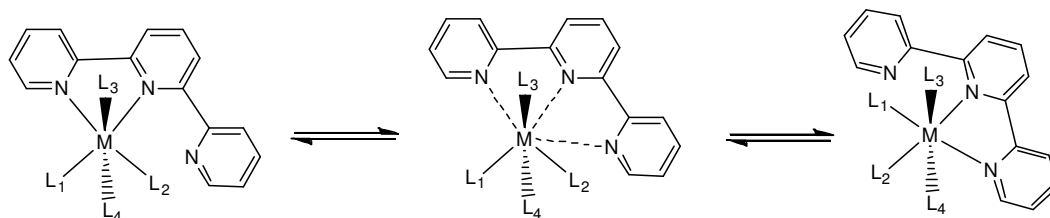


Figure 2.3 “Tick-tock twist” mechanism.

A summary of literature examples of analogous fluxional systems, activation parameters and free energies is given in Table 2.2. Also included are dihedral angles available from reported crystal structures. The activation energies have been calculated from the coalescence temperature, the temperature at which the appearance of the spectrum changes from that of two separate peaks to that of a single peak. The ΔS^\ddagger values are negative for the platinum complexes which is consistent with an associative (A) mechanism. However, the values are positive for other systems which may be

Table 2.2 Activation parameters for fluxional tpy for d⁶ complexes.

Complex	Dihedral Angle (°)	Coord. no in Transition State	ΔH^\ddagger kJmol ⁻¹	ΔS^\ddagger Jmol ⁻¹ K ⁻¹	ΔG^\ddagger , kJ mol ⁻¹ T= 298 K	T_c (K)
[ReCl(CO) ₃ (η^2 -tpy)] ^a	52.9	7	77.2±1.4	23.2±4.0	70.3±0.2	
[ReBr(CO) ₃ (η^2 -tpy)] ^a		7	79.8±1.7	27.5±4.8	71.6±0.3	343
[ReI(CO) ₃ (η^2 -tpy)] ^a		7	76.3±0.9	11.1±2.4	73.0±0.1	
[W(CO) ₄ (η^2 -tpy)] ^b		7	69.7±1.9	45.9±6.7	56.1±0.1	283
[PtClMe ₃ (η^2 -tpy)] ^b		7	57.90±1.41	-13.7±4.3	61.97±0.12	303
[PtBrMe ₃ (η^2 -tpy)] ^b		7	52.90±0.99	-28.8±3.0	61.48±0.10	
[PtMe ₃ (η^2 -tpy)] ^b	52.1	7	58.10±2.26	-14.8±6.9	62.53±0.20	
[Mo(CO) ₄ (η^2 -tpy)] ^c		7	52.4±1.6	13.3±6.6	48.4±0.4	
[RuCl ₂ (CO) ₂ (η^2 -tpy)] ^c		7	88.3±1.4	41.8±4.1	75.8±0.2	
[RuBr ₂ (CO) ₂ (η^2 -tpy)] ^c		7	86.2±2.6	29.4±7.5	77.4±0.3	
[RuI ₂ (CO) ₂ (η^2 -tpy)] ^c		7	83.1±0.9	14.8±2.6	78.7±0.1	

^a From Reference 5, ^b From Reference 6, ^c From Reference 7.

consistent with a dissociative (D) mechanism. Correlation of ΔH^\ddagger and ΔS^\ddagger in an isokinetic plot is given for the complexes in Figure 2.4.^{7d}

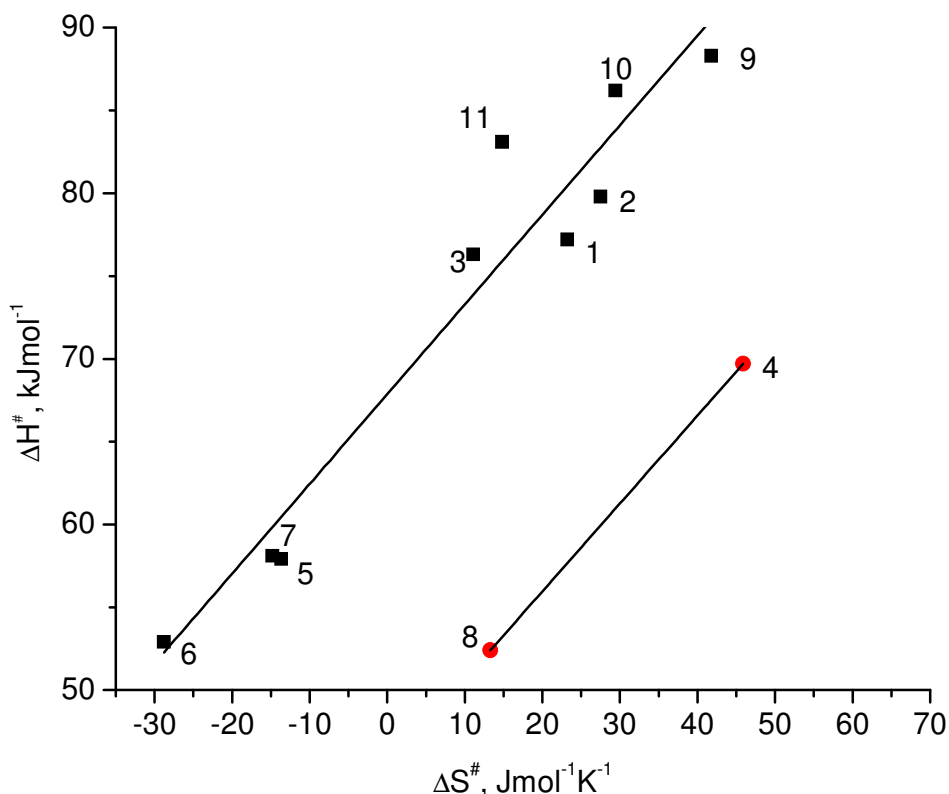


Figure 2.4 Isokinetic plot for $[\text{Re}(\text{CO})_3(\eta^2\text{-tpy})\text{Cl}]$ (1), $[\text{Re}(\text{CO})_3(\eta^2\text{-tpy})\text{Br}]$ (2), $[\text{Re}(\text{CO})_3(\eta^2\text{-tpy})\text{I}]$ (3), $[\text{W}(\text{CO})_4(\eta^2\text{-tpy})]$ (4), $[\text{PtMe}_3(\eta^2\text{-tpy})\text{Cl}]$ (5), $[\text{PtMe}_3(\eta^2\text{-tpy})\text{Br}]$ (6), $[\text{PtMe}_3(\eta^2\text{-tpy})\text{I}]$ (7), $[\text{Mo}(\text{CO})_4(\eta^2\text{-tpy})]$ (8) and $[\text{Ru}(\text{CO})_2(\eta^2\text{-tpy})\text{Cl}_2]$ (9), $[\text{Ru}(\text{CO})_2(\eta^2\text{-tpy})\text{Br}_2]$ (10), $[\text{Ru}(\text{CO})_2(\eta^2\text{-tpy})\text{I}_2]$ (11) complexes.^{7d}

The observation of a correlation between ΔH^\ddagger and ΔS^\ddagger is consistent with a common transition state.^{7d} The correlations are remarkable given the differing ligand sets for the compounds given in Table 2.2. There appear to be two separate correlations both possessing a slope of 0.5. It must be recognized that ΔS^\ddagger values determined from Eyring plots possess large errors due to an extrapolation of over 250 K. Even so the calculated ΔS^\ddagger values are statistically distinct. The formation of a seven coordinate transition state

involves the synchronous formation and cleavage of two bonds and the degree of bond cleavage as reflected by ΔH^\ddagger . However, the formation is difficult to assess since the transition state is not experimentally detectable.

The minimum energy required for the exchange of two equivalent nuclei by an intramolecular process is dictated by an activation energy (E_a), which is experimentally determined from the temperature dependence of the rate constant (k) using the Arrhenius eqn. given by

$$k = A \exp \frac{-E_a}{RT} \quad (2.1)$$

$$\ln k = -\frac{E_a}{R}(1/T) + \ln(A) \quad (2.2)$$

A plot of $\ln(k \times 1s)$ vs $1/T$ gives a straight line with slope = $-\frac{E_a}{R}$ (where R is the gas constant).

The Arrhenius equation is an empirical equation that describes the temperature dependence of the rate constant. As such, the equation does not provide microscopic information on the molecular dynamics. Eqn. 2.2 is useful in characterizing the temperature dependence of rate constants in complicated systems that are difficult to characterize at the molecular level, *i.e.* biological enzymatic processes where the structures may not be known. Transition state theory provides a theoretical scaffold to understand and quantify molecular properties that dictates the temperature dependence of the rate constant.

The temperature dependence of the rate constant interpreted using transition state theory provides parameters that allow an understanding of the dynamics at a molecular

level. Transition state theory requires the assumptions that the system is at thermal equilibrium at all points along a reaction coordinate and that the transition state is in equilibrium with the reactants. Under these conditions, the temperature dependence of the rate constant is given by

$$k = k'_o \exp^{\frac{-\Delta G^\ddagger}{k_B N_A T}} \quad (2.3)$$

where ΔG^\ddagger is Gibb's energy of activation, k'_o is the rate constant for the reaction in the absence of a kinetic barrier, k_B is Boltzman's constant, N_A is Avogadro's number, and T is the temperature. The product ($k_B N_A$) is equal to R , the ideal gas constant. The Gibb's energy of activation (ΔG^\ddagger) is related to ΔH^\ddagger , the enthalpy of activation and entropy of activation by

$$\Delta G^\ddagger = \Delta H^\ddagger - T\Delta S^\ddagger \quad (2.4)$$

The temperature dependence of the rate constant given by equation 2.2 can be expanded by substitution of equation 2.4 into 2.3 which yields

$$k = k'_o \exp\left(\frac{-\Delta H^\ddagger}{RT} + \frac{\Delta S^\ddagger}{R}\right) \quad (2.5)$$

Plots of $\ln k$ vs $1/T$ (Eyring plots) should be linear with a slope of $\frac{-\Delta H^\ddagger}{R}$ and an intercept of $\frac{\Delta S^\ddagger}{R}$.

The data given in Table 2.2 provide insight into the dynamic behaviour of molecular systems containing η^2 -tpy, as a function of the metal center. Values of ΔG^\ddagger ($T = 298 \text{ K}$) are 10 - 15 kJmol^{-1} larger for ruthenium and rhenium carbonyl complexes than

that of platinum, molybdenum and tungsten complexes. Transition states for all the systems listed in the Table 2.2 are thought to be seven coordinate.

Fluxionality of tpy has also been studied in ruthenium carbonyl halide complexes, $[\text{RuX}_2(\text{CO})_2(\text{tpy})]$ ($X = \text{Cl}, \text{Br}$ or I) and some metal tetracarbonyl complexes $[\text{M}(\text{CO})_4(\text{tpy})]$ ($M = \text{Cr}, \text{Mo}$ or W). Unfortunately, the ruthenium based complexes react to form the thermodynamically stable tridentate ligand species under the conditions of the reported experiments. However, in light of the isoelectronic nature of the metals ($M = \text{Ru}^{\text{II}}, \text{Cr}, \text{Mo}, \text{W}$) and structural similarity it has been concluded that the tick-tock twist mechanism is most likely to be functioning for these complexes.⁷

Constable *et al.*^{3b} studied a series of complexes containing bidentate tpy with the general formula $[\text{Ru}(\text{L})_2(\eta^2\text{-tpy})]^{2+}$ [$\text{L} = \text{bpy}$ or 1,10-phenanthroline] where the dynamic behavior of the tpy ligand was concluded to be a process analogous to the “ring wobbling”.

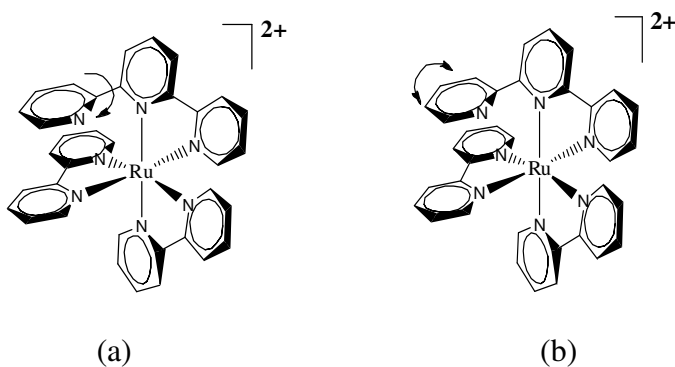


Figure 2.5 (a) Rotation and (b) Ring wobbling processes.

Schmehl *et al.* reported⁴ a series of $[\text{Ru}(\text{bpy}-d_8)_2(\text{L})]^{2+}$ complexes where L is a 2-phenyl- or 2,9-diphenyl substituted phenanthroline ligand. The use of $\text{bpy}-d_8$ instead of bpy , significantly reduces the complexity of the ^1H NMR spectra.

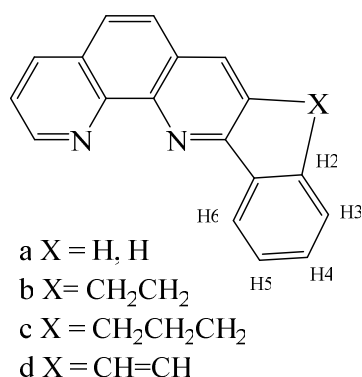


Figure 2.6 Structures of substituted 1,10-phenanthroline ligands.

The ^1H NMR data analysis revealed the temperature dependence of the NMR bands assigned to the 2-phenyl ring in the $[Ru(bpy-d_8)_2(a)]^{2+}$ complex. The dihedral angle for the ligated 2-phenylphen ring is close to 55° as determined from the crystal structure, significantly larger than that of 28° calculated for the free ligand. Moreover, the twisted conformation that is stabilized by the noticeable π -stacking between the 2-phenyl ring and one of the adjacent $bpy-d_8$ ligands, is evident from the upfield shifted signals of the five protons of the pendant ring. At 298 K, the ^1H NMR spectrum shows broadening of signals for these five protons which indicates the restricted movement of the 2-phenyl ring. As the temperature is increased to 338 K, the phenyl ring freely rotates on the NMR time scale and the signals become sharper as the protons H2, H3, H5 and H6 start to coalesce. The H4 proton remains unaffected due to its position. However, the free rotation of the phenyl ring can be restricted by adding a bridging substituent as shown in Figure 2.6.

Gafney *et al.*^{8a} extensively studied the protonation chemistry of $[Ru(bpy)_2(dpp)]^{2+}$ (dpp = 2,3-bis(2-pyridyl)pyrazine) in the ground and excited states. Figure 2.7 shows the

protonated structure of $[\text{Ru}(\text{bpy})_2(\text{dpp})]^{2+}$ and the steric repulsion between the 3C and 3B protons. It has been reported that in the excited state, MLCT increases the basicity of the dpp peripheral nitrogen in $[\text{Ru}(\text{bpy})_2(\text{dpp})]^{2+}$.^{8a} In the ground state, protonation of the peripheral N of dpp pendant pyridine takes place as evident from the ^1H NMR data.^{8a} The ^1H NMR spectrum of $[\text{Ru}(\text{bpy})_2(\text{dpp})]^{2+}$ shows signals for 26 protons as expected. However, increasing the acidity with the addition of D_2SO_4 , changes the chemical shift of five protons to a lower field. Four of them have been assigned to the protons from the dpp pendant pyridyl rings (3C-6C) and one from the coordinated pyridyl ring in dpp (3B).

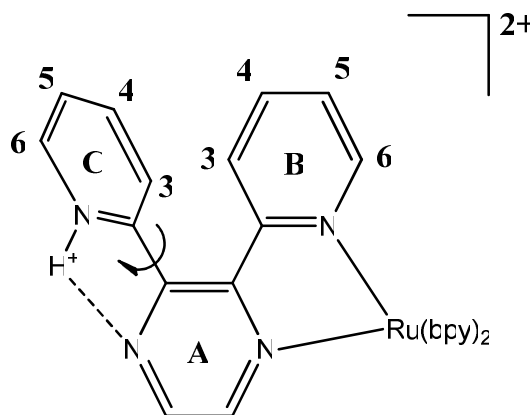


Figure 2.7 Structure of protonated $[\text{Ru}(\text{bpy})_2(\text{dpp})]^{2+}$.^{8a}

Ground-state protonation of the dpp peripheral pyridine is also evident from the emission and absorption spectra, as changes occur in the emission spectra of the complex. Initially the pendant pyridine remains perpendicular to the dpp ligand. Protonation twists the pendant pyridine into the plane of the coordinated pyridine and pyrazine portions of the coordinated dpp. The protonated $[\text{Ru}(\text{bpy})_2(\text{dpp})]^{2+}$ then takes on a cyclic structure as the proton bridges both peripheral dpp nitrogens (Figure 2.7). This might be due to the

electron accepting ability of the protonated pyridine.^{8b} However, the proton is not equally shared and is more closely associated with the dpp peripheral pyridine rather than the peripheral pyrazine nitrogen which is evident from the NMR spectrum.

2.3 Objectives

Recently, tpy-based ruthenium polypyridyl complexes have received much more attention as they exhibit important photochemical and electrochemical properties. Related investigations performed as a part of this thesis will be described in chapter 3.

The properties of tpy as an acceptor ligand in excited states have been characterized by resonance Raman, emission spectral fitting, temperature-dependent lifetimes and quantum yields. To address the excited states in bidentate tpy based complexes, it is a prerequisite to characterize the ground state properties. The purpose of our present study is to investigate the ground state dynamics and the fluxional behavior of tpy in a stable octahedral ruthenium polypyridyl complex, prior to studying the excited states of $[\text{Ru}(\text{bpy}-d_8)_2(\eta^2\text{-tpy})]^{2+}$.

A previously published study was completed with the $[\text{Ru}(\text{bpy})_2(\eta^2\text{-tpy})]^{2+}$ complex where ^1H NMR spectra were too complicated for the detailed evaluation of temperature dependent torsional and other conformational changes.^{3b} In this study, $[\text{Ru}(\text{bpy}-d_8)_2(\eta^2\text{-tpy})]^{2+}$ has been used to obtain simplified ^1H NMR spectra. Thus, deuteration of bpy assisted the interpretation of the fluxional dynamics as the signals due the tpy ligand only appear in the ^1H NMR spectrum.

2.4 Results and Discussion

2.4.1 Ground State Dynamics of $[\text{Ru}(\text{bpy-}d_8)_2(\eta^2\text{-tpy})]^{2+}$

Deuteration of polypyridyl ligands is a powerful approach to simplify the complexity of ^1H NMR spectra to facilitate the characterization of complexes and possible dynamic conformational processes.⁹ In this work, the replacement of bpy with $\text{bpy-}d_8$ was made to render the bpy ligands NMR silent in the ^1H NMR of $[\text{Ru}(\text{bpy-}d_8)_2(\eta^2\text{-tpy})]^{2+}$ derivatives. The synthetic protocols are described in Chapter 5.

At ambient temperature the ^1H NMR spectrum of the $[\text{Ru}(\text{bpy})_2(\eta^2\text{-tpy})]^{2+}$ complex in CD_3CN solution is exceedingly complicated because all the protons are non-equivalent giving rise to 27 peaks, all of which are coupled, Figure 2.8.

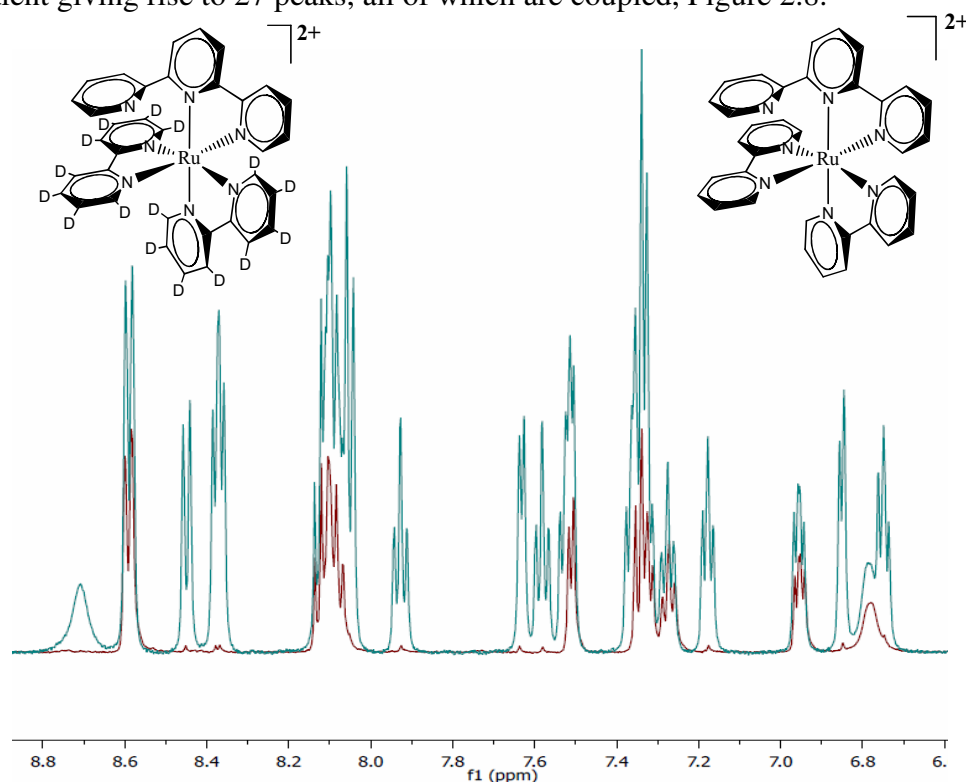


Figure 2.8 Overlaid spectra of $[\text{Ru}(\text{bpy-}d_8)_2(\eta^2\text{-tpy})][\text{PF}_6]_2$ (brown) and $[\text{Ru}(\text{bpy})_2(\eta^2\text{-tpy})][\text{PF}_6]_2$ (blue).

The aromatic region of the ^1H NMR spectrum of $[\text{Ru}(\text{bpy-}d_8)_2(\eta^2\text{-tpy})]^{2+}$ and assignments are shown in Figure 2.9.

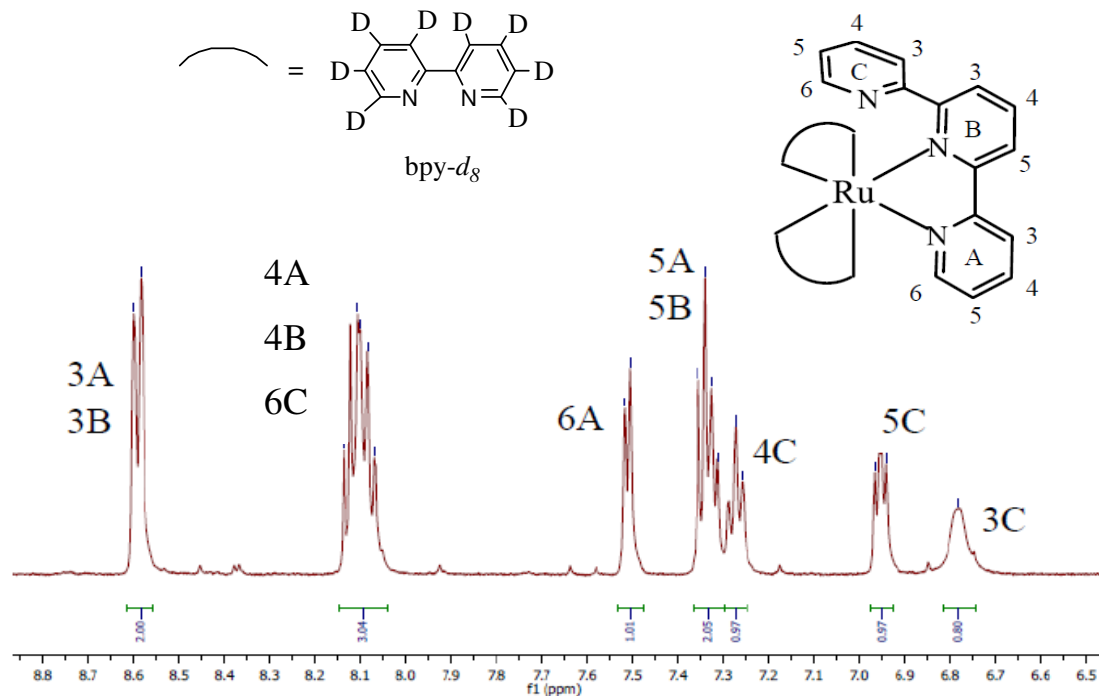


Figure 2.9 500 MHz ^1H NMR spectrum (aromatic region) of $[\text{Ru}(\text{bpy-}d_8)_2(\eta^2\text{-tpy})]^{2+}$ in CD_3CN at 298 K.

Since the bpy ligands are deuterated, only the resonances associated with the tpy ligand are observed in the ^1H NMR spectrum of the $[\text{Ru}(\text{bpy-}d_8)_2(\eta^2\text{-tpy})]^{2+}$ complex together with small signals from bpy- d_8 impurities (NMR spectrum for bpy- d_8 is shown in Chapter 5, section 5.2).

Overlaid ^1H NMR spectra for $[\text{Ru}(\text{bpy})_2(\eta^2\text{-tpy})]^{2+}$ and $[\text{Ru}(\text{bpy-}d_8)_2(\eta^2\text{-tpy})]^{2+}$ complexes are shown in Figure 2.8. It is apparent that the tpy resonances are identical for the $[\text{Ru}(\text{bpy})_2(\eta^2\text{-tpy})]^{2+}$ and $[\text{Ru}(\text{bpy-}d_8)_2(\eta^2\text{-tpy})]^{2+}$ complexes. The ^1H NMR spectrum for $[\text{Ru}(\text{bpy-}d_8)_2(\eta^2\text{-tpy})]^{2+}$ consists of one broad singlet, two doublets, two triplets, one

doublet of doublets and one multiplet. The assignments were made by comparison to the $[\text{Ru}(\text{bpy})_2(\eta^2\text{-tpy})]^{2+}$ complex. The doublet at $\delta 8.59$ ($J = 10$ Hz) is due to the 3A and 3B protons of the tpy ligand. Another doublet at $\delta 7.51$ ($J = 5$ Hz) is caused by the 6A proton of the tpy ligand. Triplets at $\delta 7.27$ ($J = 10$) and 6.95 ($J = 5$ Hz) can be attributed to the 4C and 5C protons, respectively. The multiplet at $\delta 8.10$ is as a result of the 4A, 4B and 6C protons. The doublet of doublets at $\delta 7.33$ can be assigned to the 5A and 5B protons. The broad singlet at $\delta 6.78$ is due to the 3C proton of the tpy ligand.

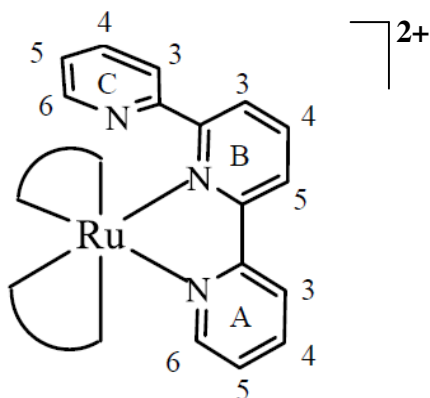


Figure 2.10 Structure of the $[\text{Ru}(\text{bpy}-d_8)_2(\eta^2\text{-tpy})]^{2+}$ complex.

The ^1H NMR data are dynamic in the $\delta 6.4$ to $\delta 8.8$ ppm region. Temperature dependent ^1H NMR spectra, recorded for $[\text{Ru}(\text{bpy}-d_8)_2(\eta^2\text{-tpy})][\text{PF}_6]_2$ are shown in Figure 2.11.

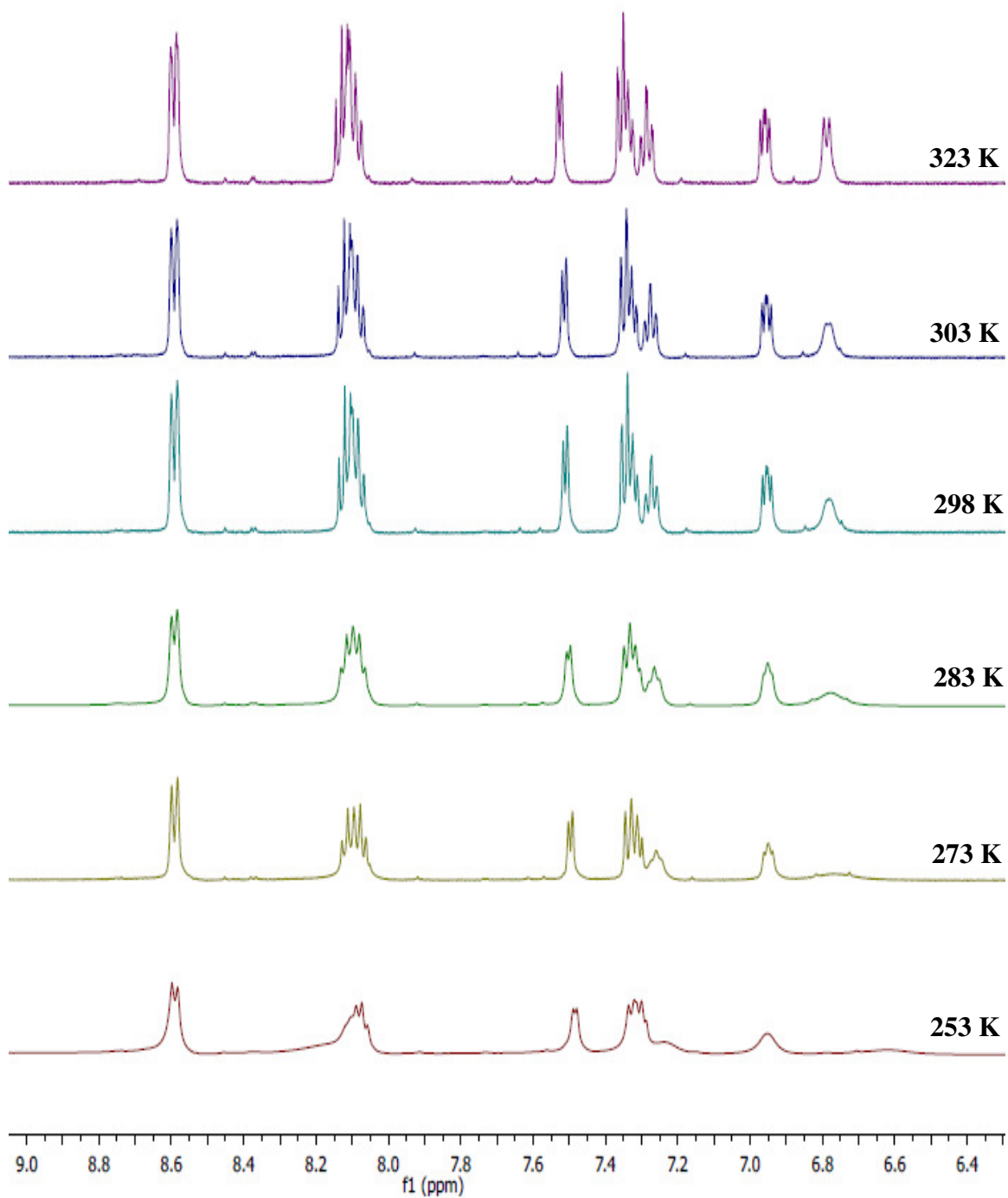


Figure 2.11 Variable temperature ^1H NMR spectra of $[\text{Ru}(\text{bpy-}d_8)_2(\eta^2\text{-tpy})]^{2+}$ in CD_3CN over the temperature range 253-323 K.

At room temperature the ^1H NMR spectrum of $[\text{Ru}(\text{bpy-d}_8)_2(\eta^2\text{-tpy})]^{2+}$ shows one broad signal (δ 6.78) assigned to the 3C proton of the tpy ligand which was shifted upfield at lower temperatures. Upon cooling to 0 °C the band width of this resonance increased whereas the resolution of the room temperature spectrum is consistent with a process which is rapid on the NMR time scale. By -20 °C, the upfield signal is fully broadened, and is barely observable and there is a large upfield shift (δ 6.66), together with significant changes in the positions and bandwidths of the bands assigned to the 4C and 5C protons at δ 7.27 and 6.95 ppm, respectively. These changes can be attributed to the wobbling (Figure 2.12) of the pendant pyridine ring of the tpy ligand at low temperature based on comparison with the $[\text{Ru}(\text{bpy-d}_8)_2(\text{phen-R})]$ systems (see section 2.1.2) where the rotation is restricted.

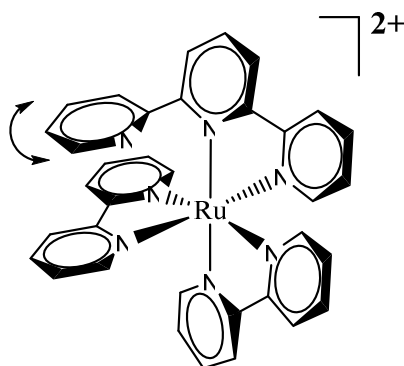


Figure 2.12 Wobbling of the pyridine ring.

The 3C signal keeps broadening since the 3C proton moves far away from the 3B proton to which it is coupled. At $T = 253$ K, there exists a broad resonance at δ 6.66, that is barely perceptible and slightly shifted to upfield. This shift is caused by transient

electron shielding of the 3C proton as it rotates close to the electron rich adjacent bpy ligand.^{7a} The change in the 3C proton position affects the signals assigned to the 5C, 4C, and 6C protons, Figure 2.11. Increasing the temperature above 298 K, the signal intensity increases rapidly with temperature. At 323 K, the broad singlet due to 3C becomes a doublet. Pseudo triplets due to the 4C and 5C protons become sharp triplets and the intensity of other signals increases slightly which indicates free rotation of pendant pyridine on the NMR time scale. The broad signal at $\delta 6.78$ ppm which is assigned to the 3C proton, changes as the pyridine ring rotates from position A to B at high temperature (Figure 2.13).

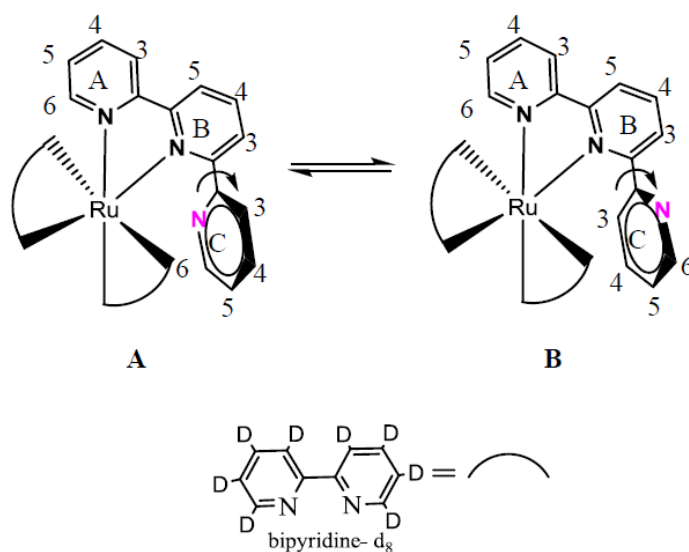


Figure 2.13 Rotation of the pyridine ring.

For the exchange or tick-tock mechanism, the signals that appear in the variable temperature ^1H NMR due to the central ring proton 4B, would remain unaltered and the exchange dynamics between the ring A and C of the tpy ligand would change the proton

signals that are due to ring A and C. However, we do not observe any change in the signals for the 3A and 3B protons, even with the variation of temperature. This important observation suggests that the dynamics associated with this system do not follow the exchange or tick-tock mechanism described in section 2.2.2. The data suggest that for $[\text{Ru}(\text{bpy}-d_8)_2(\eta^2\text{-tpy})]^{2+}$ the ligation remains constant and cleavage of Ru-N₁ and Ru-N₂ bonds is not an important process in this family of complexes.

2.4.2 Protonation of the Pendant Pyridine

Excess trifluoroacetic acid (TFA) (0.1M) was added to a CD₃CN solution of $[\text{Ru}(\text{bpy}-d_8)_2(\eta^2\text{-tpy})]^{2+}$ and the NMR spectra before and after addition of TFA are shown in Figure 2.14.

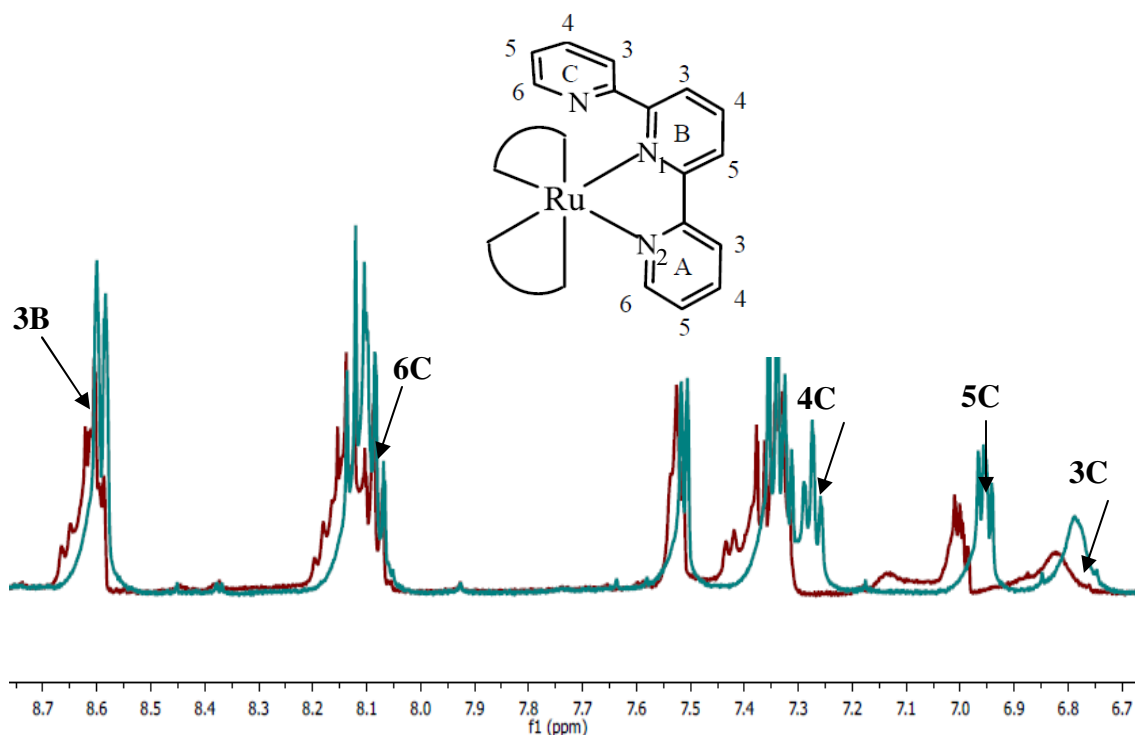


Figure 2.14 Protonation of $[\text{Ru}(\text{bpy}-d_8)_2(\eta^2\text{-tpy})]^{2+}$ with trifluoroacetic acid (TFA).

The ^1H NMR spectrum of the $[\text{Ru}(\text{bpy}-d_8)(\eta^2\text{-tpy})][\text{PF}_6]_2$ complex in CD_3CN shows signals for 11 protons as expected. However, five of the eleven protons shift to lower field (0.01- 0.1 ppm) with the addition of TFA. The changes in the ^1H NMR spectrum are consistent with the formation of the cationic species, $[\text{Ru}(\text{bpy}-d_8)_2(\eta^2\text{-tpy}-\text{H})]^{3+}$. Four of the five protons correspond to the protons on the pendant pyridyl ring (3C-6C) and one to the 3B proton on the metal coordinated pyridyl ring of tpy.

2.5 Conclusion

The fluxional solution dynamics of the tpy ligand in the $[\text{Ru}(\text{bpy}-d_8)(\eta^2\text{-tpy})]^{2+}$ complex were studied by ^1H NMR spectroscopy. Variable temperature ^1H NMR data reveal that the pendant pyridine ring of the tpy ligand in $[\text{Ru}(\text{bpy}-d_8)_2(\text{tpy})]^{2+}$ rotates, rather than undergoing an exchange or “tick-tock” twist mechanism. The ^1H NMR spectra illustrate that protonation of the peripheral N on the pendant pyridyl ring of the tpy ligand affects the chemical shifts of protons on the tpy pendant pyridyl ring rather than the protons on the metal coordinated pyridyl ring of the tpy.

2.6 References

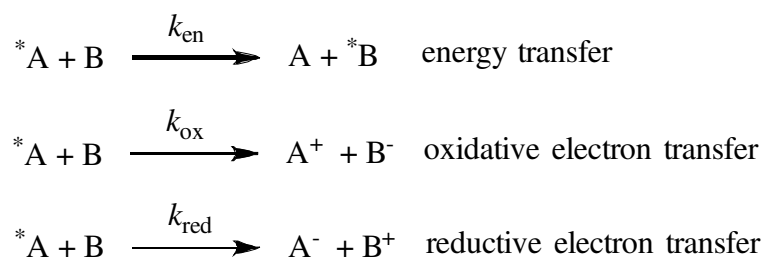
1. Morgan, G. T.; Burstall, F. H. *J. Chem. Soc.* **1932**, 20.
2. Abel, E. W.; Long N. J.; Orrell, K. G.; Osborne, A. G.; Pain, H. M.; Sik, V. *J. Chem. Soc., Chem, Commun.* **1992**, 303.
3. a) Rillema, D. P; Jones, D. S.; Woods, C.; Levy, A. *Inorg. Chem.* **1992**, *31*, 2935. b) Chotali, R.; Constable, E. C.; Hannonbn, M. J.; Tocher, D. A. *J. Chem. Soc. Dalton Trans.* **1995**, 3571. c) Pyo, S.; Pe´rez-Cordero, E.; Bott, S. G.; Echegoyen, L. *Inorg. Chem.*, **1999**, *38*, 3337.
4. Wu, F.; Riesgo, E.; Pavalova, A.; Kipp, R. A.; Schmehl, R. H.; Thummel, R. P. *Inorg. Chem.* **1999**, *38*, 5620.
5. Abel, E. W.; Dimitrov, V. S.; Long, N. J; Orrell, K. J.; Osborne, A. G; Sik, V.; Hursthouse, M. B.; Mazid, M. A. *J. Chem. Soc. Dalton Trans.* **1993**, 291.
6. Abel, E. W., Dimitrov, V. S.; Long, N. J; Orrell, K. J.; Osborne, A. G; Pain, H. M; Sik, V.; Hursthouse, M. B.; Mazid, M. A. *J. Chem. Soc. Dalton Trans.* **1993**, 597.
7. (a) Abel, E. W., Orrell, K. J.; Osborne, A. G; Pain, H. M; Sik, V. *J. Chem. Soc. Dalton Trans.* **1994**, 111. (b) Observation of the fluxional behaviour in substituted $\eta^2\text{-tpy}$ systems have been reported.^{7c} (c) Gelling, A.; Orrell, K. G.; Osborne, A. G.; Sik, V. *J. Chem. Soc., Dalton Trans.*, **1998**, 937. (d) Macartney, D. H.; Mcauley, A., *Inorg. Chem.* **1979**, *18*, 2891.
8. (a) Zambrana, J. L.; Ferloni, J. E. X.; Gafney, H. D. *J. Phys. Chem. A.* **2009**, *113*, 13457. (b) Huynh, M. H. V.; Meyer, T. *J. Chem. Rev.* **2007**, *107*, 5004.
9. Glazer, E. C.; Belyea, B.; Tor Y., *Inorg. Chem. Commun.*, **2005**, *8*, 517.

Chapter 3 Photoinduced Charge Transfer Dynamics in $[\text{Ru}(\text{bpy})_2(\eta^2\text{-tpy})]^{2+}$

3.1 Introduction and Review

3.1.1 Excited State Electron Transfer

Photoinduced electron- and energy-transfer reactions are important considering their applications in artificial photosynthesis; the conversion of light into electricity or fuels; and other photonic devices, *i. e.* sensors, molecular motors etc.^{1, 2} In a bimolecular process, an electron transfer reaction occurs when an electron, upon excitation, is transferred from an electron donating species to an electron accepting species and a charge transfer state is created. The charge transfer excited state can undergo many different processes through energy and electron transfer, with appropriate donors and acceptors as shown in Scheme 3.1.¹



Scheme 3.1 Charge transfer processes in a bimolecular system.

Photoinitiated electron transfer reactions of ruthenium(II) polypyridyl complexes have been extensively studied to establish a fundamental understanding of electron transfer and its utility in applications in solar energy conversion and many other processes.² The

excited state electron-transfer quenching of $^3[\text{Ru}(\text{bpy})_3]^{2+*}$ by several donors and acceptors is well-documented.³ For example, excited state electron transfer quenching of $^3[\text{Ru}(\text{bpy})_3]^{2+*}$ by electron donors such as 10-methylphenothiazine (10-MePTZ) or electron acceptors such as methylviologen (MV^{2+}) are known.

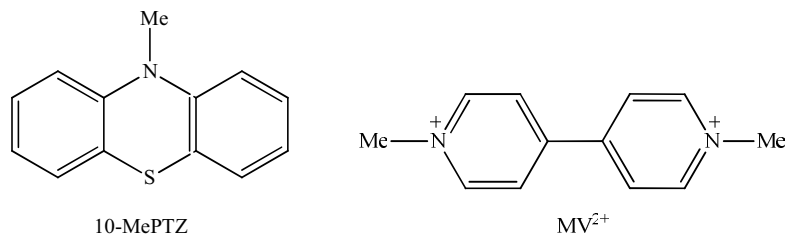
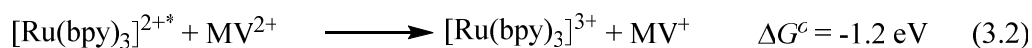
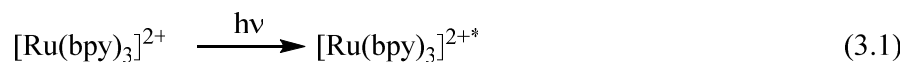


Figure 3.1 Structure of 10-methylphenothiazine (10-MePTZ) and methylviologen (MV^{2+}).

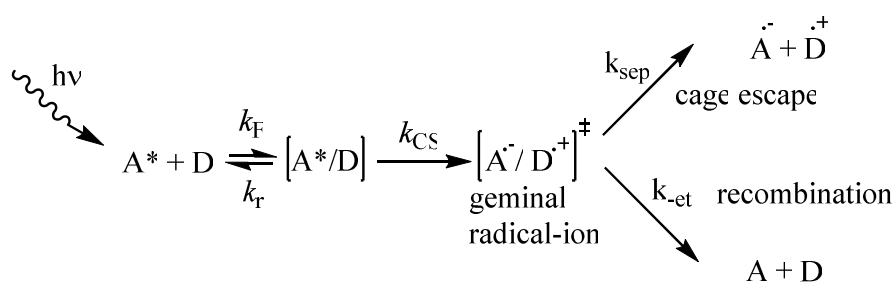


Scheme 3.2 Electron transfer quenching of $[\text{Ru}(\text{bpy})_3]^{2+*}$.

Scheme 3.2 illustrates the fundamental concept of artificial photosynthesis where $[\text{Ru}(\text{bpy})_3]^{2+}$ can act as a chromophore and a sensitizer. For the oxidative process ΔG° is -1.2 eV (eqn. 3.2), whereas for the reductive process the value is +2.5 eV (eqn. 3.3). However, the value of ΔG° is +1.3 eV for the overall reaction (eqn. 3.4).

3.1.2 Limitations of Bimolecular Reactions

There are a number of limitations of bimolecular electron transfer reactions. These reactions do not have any vectorial control, as well as no control over special orientation adduct (D||A) complexes. Following photoinduced electron-transfer to create a redox separated state, the products are formed within a solvent cage. If back electron-transfer ($k_{\text{-et}}$) is competitive with cage escape (k_{sep}), as outlined in Scheme 3.3 the photonic energy stored in the transient geminal radical-ion pair is wasted.⁴



Scheme 3.3 Quenching of an excited-state via electron transfer.⁴

As a result, the efficiency of the product formation is decreased by competing with the separation of the radical ions. The rate of electron transfer reactions from a donor molecule to an acceptor in a solvent is controlled by several factors such as:⁴ the Gibb's energy change of the reaction (ΔG), the total reorganization energy λ , and the electron transfer distance (d) between the donor and acceptor groups. The electron transfer rate constant k_{et} is given by

$$k_{\text{et}} = \kappa_{\text{el}} \nu_{\text{n}} \exp[-\Delta G^*/RT] \quad (3.5)$$

where κ_{el} = electronic transmission coefficient ($\kappa_{\text{el}} \leq 1$), ν_{n} is the nuclear frequency that is coupled to electron transfer between a donor/acceptor and ΔG^* is the Gibb's energy of

activation. When the electron transfer distance d and λ_t are kept constant, the Gibb's energy of activation ΔG^* is given by

$$\Delta G^* = (\lambda_t + \Delta G^\circ)^2 / (4\lambda_t) \quad (3.6)$$

Then, the equation [3.5] can be expanded to give

$$k_{et} = \kappa_{el} \nu_n \exp[-(\lambda_t + \Delta G^\circ)^2 / (4\lambda_t RT)] \quad (3.7)$$

Marcus theory predicts that k_{et} will follow a bell-shaped energy dependence as a function of ΔG° under conditions where λ_t is held constant.⁴ The maximum of the bell-shaped curve occurs when λ_t equals $-\Delta G^\circ$. When $-\Delta G^\circ > \lambda_t$, the rate constant for electron transfer is attenuated as the driving force is increased. This is illustrated in Figure 3.2. The parabolic dependence is not often observed in bimolecular reactions due to diffusional masking $k_{diff} \sim 10^{10} \text{ M}^{-1}\text{s}^{-1}$. This is a consequence that accrues from the reorganization energetics for electron transfer that tend to be large, and $-\Delta G^\circ / \lambda_t \gg 1$ exceeds the diffusional limits.⁴

Figure 3.2 shows^{4b} that as the reaction progresses from reactants (heavy potential energy curve) to products (light potential energy curve) via thermal activation where $\Delta G^\circ \ll \lambda_t$ (where, λ_t = total reorganization energy) in the Marcus normal region, k_{et} increases as ΔG° increases.

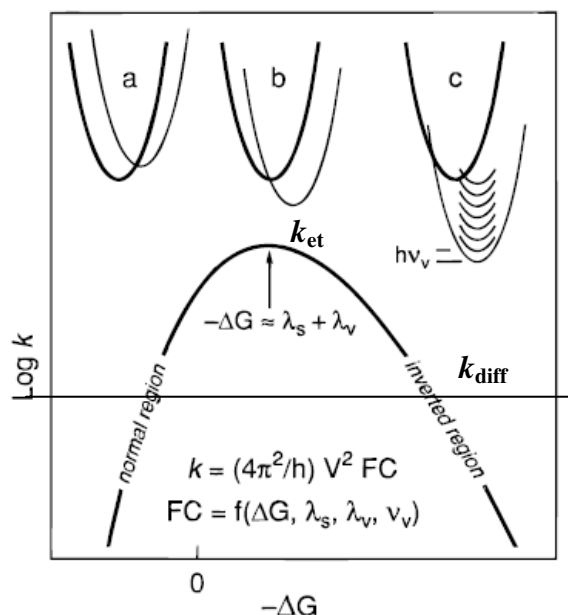


Figure 3.2 Parabolic dependence of the ET rate constant on the free energy driving force. The diffusion limit, signified by the horizontal solid line, truncates the parabola. (Reprinted with permission from reference 4b, Copyright © 1996 American Chemical Society).

When ΔG^0 approaches λ_t , ΔG^0 decreases, Figure 3.2(a). When $\Delta G^0 = \lambda_t$, there is no barrier to electron transfer and the dependence of ΔG^0 on λ_t is temperature independent, Figure 3.2 (b). In the limit where $\Delta G^0 > \lambda_t$, Figure 3.2(c), the potential energy surfaces become nested and the mechanism for electron transfer between the redox partners changes from thermally activated surface crossing to a quantum mechanical tunnelling process, which can be described using the Fermi Golden Rule given by

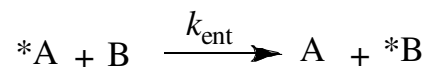
$$k = (4\pi^2 / h) V^2 FC \quad (3.8)$$

Where V^2 is the vibrationally induced electron coupling between A and D and FC is the weighted density of vibronic states that couple the initial and final states. In the limit where $\Delta G^0 \gg \lambda_t$, the Born-Oppenheimer and Condon approximations are not applicable

as electron motion occurs on the time scale of vibrational motion.⁴ The electronic states are then mixed by coupling to vibrations, leads to new wave functions that are no longer orthogonal.

3.1.3 Energy Transfer

Three types of mechanism are known for energy transfer processes. The trivial mechanism is related to the radiative transfer between an emitting molecule and an absorbing molecule and considered as an indirect photon hopping mechanism.



Scheme 3.4 The trivial energy transfer mechanism.

This occurs when there is a significant overlap of the emission and absorption spectra between the uncoupled emitting and absorbing molecules. Scheme 3.4 shows the trivial energy transfer mechanism where k_{ent} is the rate constant for energy transfer. In addition to the trivial mechanism, there are two other mechanisms by which energy is transferred between a donor and an acceptor.⁵ The Förster mechanism requires resonance dipole-dipole interaction between the donor and acceptor. The Dexter mechanism involves exchange coupling between the donor and acceptor.

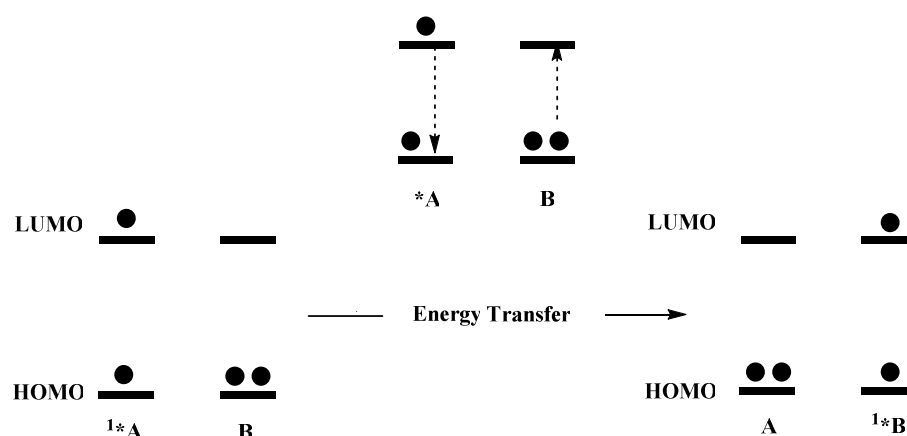


Figure 3.3 The Förster mechanism for energy transfer.⁵

In the Förster mechanism, energy is transferred via singlet states and direct orbital overlap is not required for the donor and acceptor (Figure 3.3).⁵ However, in this mechanism energy transfer requires resonance dipole-dipole interaction *i.e.* the energy emitted by the donor must match that absorbed by the acceptor. Here, energy transfer is induced by the transition dipoles of the donor and acceptor and from the donor and the acceptor coulombic interactions yields the rate of energy transfer as equation 3.9.

$$k_{ET}^{Förster} = \alpha D_A^2 D_B^2 \frac{1}{R^6} \quad (3.9)$$

where α is a proportionality constant, D_A is the transition dipole of the donor, D_B is the transition dipole of the acceptor, and R is the distance between the donor and the acceptor.

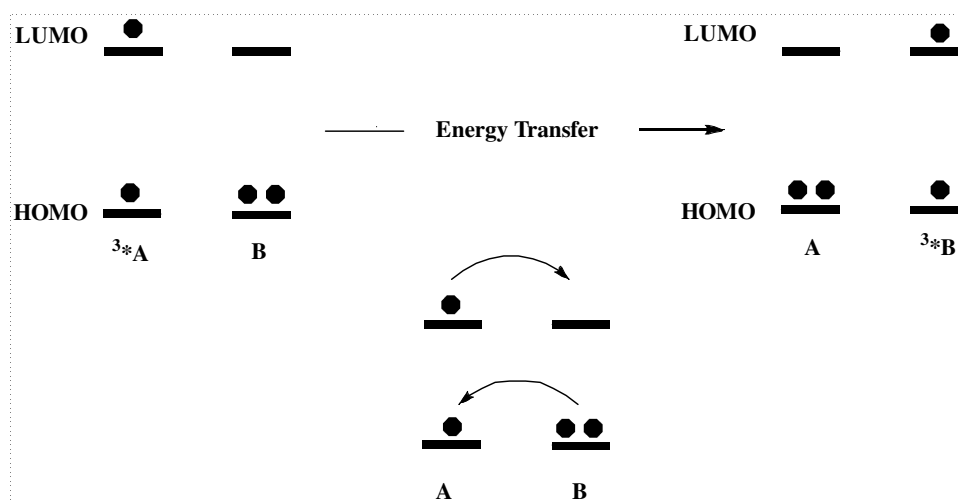


Figure 3.4 The Dexter mechanism for energy transfer.⁵

In the Dexter mechanism, energy transfer takes place after the electron exchange interactions between the donor and acceptor, Figure 3.4.⁵ This interaction results in a rate constant for energy transfer via the Dexter mechanism given by equation 3.10.

$$k_{ET}^{Dexter} = KJ' \exp\left(\frac{-2R}{L}\right) \quad (3.10)$$

where J' is the overlap integral reflecting the extent to which the donor and acceptor absorption spectrums overlap, K is an experimental constant which relates to the magnitude of the orbital interaction for electron exchange, R is the distance between the donor and acceptor, and L is the sum of the Van Der Waals radii of the donor and acceptor. The efficiency of energy transfer via the exchange mechanism decreases exponentially with donor-acceptor distance.⁵

The Dexter mechanism requires direct orbital overlap of the donor and the acceptor for an electron exchange interaction to occur. The Förster mechanism, on the other hand, does not require direct orbital overlap between the donor and the acceptor.

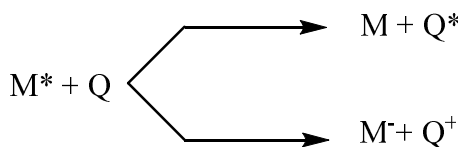
However, both of these mechanisms exist to some extent in reactions. Thus, the observed rate of energy transfer is given by:

$$k_{obsd} = k_{F\ddot{o}rster} + k_{Dexter} \quad (3.11)$$

where $k_{F\ddot{o}rster}$ is the rate constant for F\ddot{o}rster energy transfer and k_{Dexter} is the rate constant for Dexter energy transfer.

3.1.4 Competition between Energy and Electron Transfer

Energy and electron transfer are two primarily important processes for the quenching of molecular excited states (Scheme 3.1). In the excited states, the molecule differs electronically from the ground states.⁶ Quenching of excited states by either electron transfer or energy transfer is well known and a competition between these two quenching processes is an active area of research.⁷ Wrighton *et al.*,⁸ reported the quenching of excited $[Ru(bpy)_3]^{2+}$ and $[Ru(bpz)_3]^{2+}$ by ferrocene and its methyl derivatives through both energy and electron transfer (Scheme 3.5).



Scheme 3.5 Schematic diagram for the competition of energy and electron transfer processes.

The $E_{1/2}$ values for the methyl derivatives of ferrocene range from 0.38 to -0.11 V vs SCE in CH_3CN . Variation of the ferrocene quencher or excited state reagent allows the driving force to be changed in favour of electron transfer rather than energy transfer as

the lowest excited state energies of ferrocene and $[\text{Ru}(\text{bpy})_3]^{2+}$ are very close, 1.8 eV and 2.15 eV, respectively. The quenching of $[\text{Ru}(\text{bpy})_3]^{2+}$ by ferrocene occurs with a driving force of ~ 0.4 eV, which is inadequate for energy transfer. However, it was established that an electron transfer driving force of ~ 1.5 eV allows equal quenching of $[\text{Ru}(\text{bpy})_3]^{2+}$ by ferrocene through electron and energy transfer.⁷

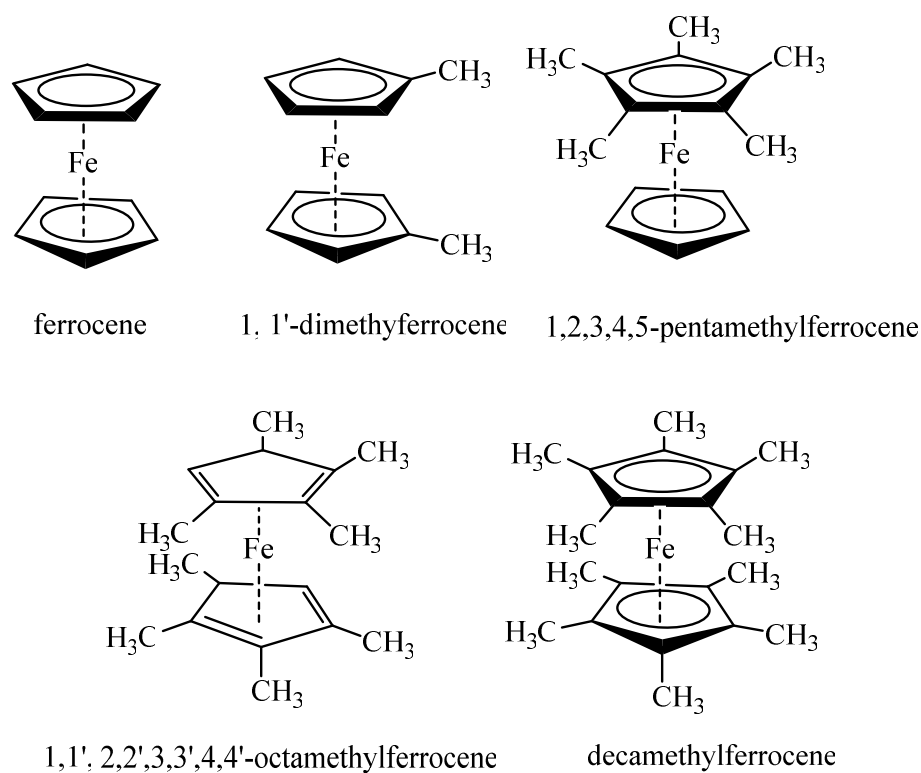


Figure 3.5 Structures of ferrocene and its methyl derivatives.⁷

3.1.5 Chromophore-Quencher Complexes

Ruthenium(II) polypyridyl complexes have dominated research into excited state electron and energy transfer due to their long-lived excited states which can undergo both oxidative and reductive quenching reactions. The first chromophore-quencher dyad

$[(bpy)_2RuP_2]^{4+}$ (here P = 1, 1'-dimethyl-4,4'-bipyridinium) was reported by Sullivan *et al.*,⁹ Figure 3.6. This is similar to the $[Ru(bpy)_3]^{2+}$ -paraquat system as it contains attached pyridinium redox sites.

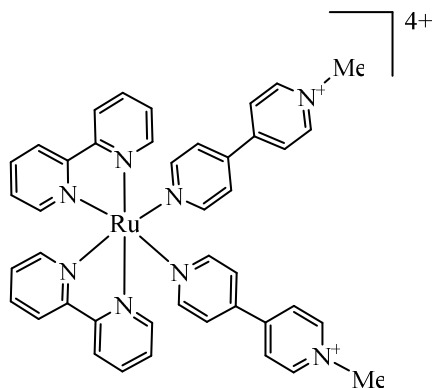


Figure 3.6 Structure of $[(bpy)_2RuP_2]^{4+}$ (P = 1, 1'-dimethyl-4,4'-bipyridinium).

Photoexcitation of chromophore-quencher complexes (such as $[Ru(dmb)(bpyCH_2PTZ)(bpyCH_2-MV^{2+})]^{4+}$ (dmb = 4,4'-dimethyl-2,2'-bipyridine) (Figure 3.7) is known where oxidative or reductive intramolecular electron transfer quenching takes place. Photoexcitation of the $Ru \rightarrow bpy$ charge transfer in $[Ru(dmb^-(bpy^-CH_2PTZ)(bpy^-CH_2-MV^{2+})]^{4+}$ with sequential intramolecular process leads to the formation of the charge separated state $(PTZ^{\bullet+})Ru(MV^{2+\bullet})$ with relatively high efficiency for which the transiently stored free energy is ~ 1.3 eV and which has a lifetime of 127 ns in CH_3CN , well below the diffusion limit in CH_3CN ($k_{diff} \sim 10^{-10} s^{-1}$).¹⁰

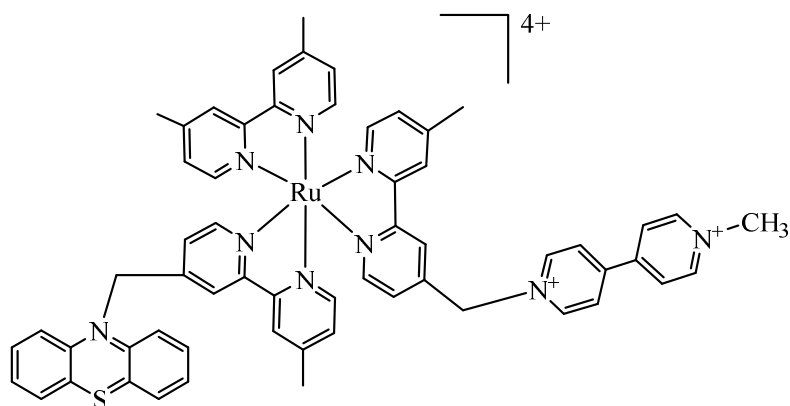
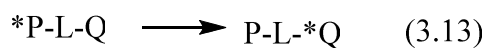


Figure 3.7 Structure of $[Ru(dmb)(bpyCH_2PTZ)(bpy(CH_2)_n\text{-MV})]^{4+}$.

In the supramolecular system P-L-Q, excitation of P leads either to energy transfer (eq 3.13) or electron transfer (eq 3.14), where P is a photosensitizer and Q is a quencher, covalently bound by a tether L.



Scheme 3.6 Energy and electron transfer processes in a supramolecular system.

Photoinduced charge separation is known for P-A and D-P dyads and in D-P-A triads where the photosensitizer P is $[M(\text{ttpy})_2]^{2+}$ ($M = Ru, Os$) (ttpy = 4'-p-toly1)-2,2':6',2''-terpyridine).^{11,12} These systems contain an organo or metallo-organic photosensitizer (P) that is covalently linked to electron acceptor (A) and electron donor (D) groups, Figure 3.8.

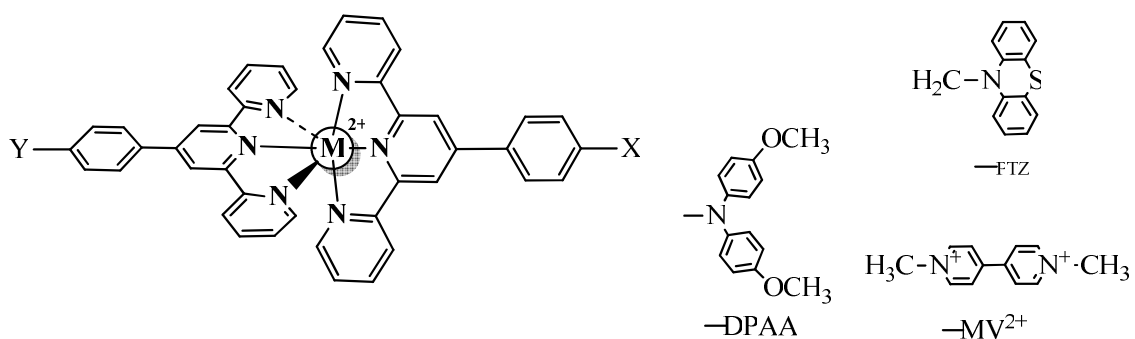


Figure 3.8 Dyads and triads where the photosensitizer is $M(tpy)_2^{2+}$ ($M = Ru, Os$). X and Y indicate the groups, PTZ, DPAA, MV^{2+} etc.

The absorption spectral data for $[Ru(tpy)_2]^{2+}$ and some dyads and triads of $[Ru(tpy)_2]^{2+}$ complexes are shown in Table 3.1.

Table: 3.1 Absorption maxima for some dyads and triads of $[Ru(tpy)_2]^{2+}$ and $[Ru(tpy)_2]^{2+}$.¹²

Complex	$\lambda_{\max}(\text{abs})$ (nm) (ϵ , M^{-1} , cm^{-1})
$[Ru(tpy)_2]^{2+}$	476 (17700)
$[Ru(tpy)_2]^{2+}$	490 (28000)
$Ru(tpy)_2^{2+}-MV^{2+}$	491 (32000)
PTZ- $Ru(tpy)_2^{2+}$	490 (31000)
DPAA- $Ru(tpy)_2^{2+}$	502 (39000)
PTZ- $Ru(tpy)_2^{2+}-MV^{2+}$	491 (32000)
DPAA- $Ru(tpy)_2^{2+}-MV^{2+}$	504 (43000)

The absorption band envelopes for $[Ru(tpy)_2]^{2+}$ and $[Ru(tpy)_2]^{2+}$ are similar except that $\lambda_{\max}(\text{abs})$ is found at longer wavelengths for $[Ru(tpy)_2]^{2+}$. However, the larger molar absorption coefficient for $[Ru(tpy)_2]^{2+}$ compared to $[Ru(tpy)_2]^{2+}$ implies

that light absorption actually leads to a larger degree of charge transfer character and possible delocalization over a larger molecular framework of the accepting ligand.¹² Similarly, electron-withdrawing and electron-donating groups attached to remote positions of ttpy in $[Ru(tpy)_2]^{2+}$ complexes have influence on the intensity of the absorption bands.

Ferrocene (Fc) is expected to act as an electron donor in multicomponent systems designed for the study of charge-separation processes as it is a useful redox agent. Systems like D-P (dyads) and D-P-A (triads), where P is the $[Ru(tpy)(phtpy)]^{2+}$ chromophore, D is ferrocene, and A is an electron acceptor, MV^{2+} have been synthesized with the purpose of utilizing these excited states for photoinduced charge separation. The energy level diagram for Ru based Fc-P dyads in Figure 3.9 shows the deactivation of the excited Fc-*P dyads.¹³

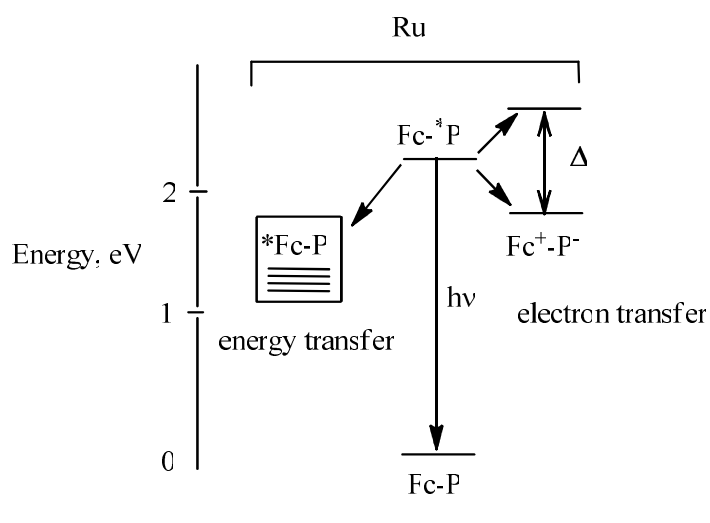


Figure 3.9 Energy-level diagram for the Ru based Fc-P dyads.¹³

The competition between electron and energy transfer is an important issue in molecular engineering. Here, electron transfer leads to a Fc^+-P^- state where the driving force is -0.34 eV for Ru based Fc-P dyad systems. In contrast, the energy-transfer step which involves the 3MLCT state of P as a donor and the triplet of Fc as an acceptor is complicated to estimate, as there are some uncertainties on the energy level of the latter.¹³ It has been observed that luminescence of the lowest-lying excited state of Fc, which is considered to be metal centered (MC) in nature and therefore highly distorted, as ΔQ is increased due to the population of a σ^* orbital in the excited MC state. However, the diagram shows that for Ru-based dyads both electron and energy-transfer are expected to be energetically allowed as the lowest triplet energy level of Fc ranges between 1.8 to 1.1 eV.¹³

3.1.6 Ground and Excited State Proton Transfer

Proton transfer plays an important role in many chemical and biological processes. Therefore, it is necessary to understand the mechanism of proton transfer reactions. Proton transfer is rapid with electronegative centers like oxygen or nitrogen as the process involves formation of hydrogen bonded dimers.¹⁴ However, for carbon centers, the exchange rate is slow. In the case of transition metal centers, the proton exchange is slower than nitrogen centered exchange and faster than carbon centered exchange. Bimolecular rate constants for proton transfer self-exchange reactions are given in Table 3.2.¹⁴ The proton exchange rate constants for the amines are considerably higher than for the transition metal complexes.

Table 3.2 Proton transfer self-exchange rate constants for selected reactions:¹⁴

	Solvent	$k_{ex}, M^{-1}s^{-1}$
$NH_4^+ + NH_3$	H_2O	1.3×10^9
$CH_3NH_3^+ + CH_3NH_2$	H_2O	0.4×10^9
$PhNH_3^+ + PhNH_2$	CH_3CN	$\geq 10^8$
$HM(cp)(CO)_3 + M(cp)(CO)_3^-$	CH_3CN	
M = Cr		1.8×10^4
M = Mo		2.5×10^3
M = W		6.5×10^2
Dimethyl sulfoxide (DMSO)		8 ± 2
H_2O		1.0×10^{-14}

Scheme 3.7 shows the mechanism for the proton self-exchange in solution.¹⁴ In the beginning, the acid and conjugated base diffuse together to form a precursor complex (eqn. 3.15) where the distance between the metals is r . Exchange of a proton takes place within this complex (eqn. 3.16), followed by dissociation that results in the formation of separated products in the final step (eqn. 3.17).

**Scheme 3.7** Mechanism for the proton self-exchange.¹⁴

When the value of r is small, proton transfer is favoured and occurs rapidly in the second step (eqn. 3.16). However, electron-electron repulsion (as well as other factors) hinders the close attraction of the reactants by a repulsive interaction U^r . Therefore the proton transfer of a given system will occur over a range of distances, with a bimolecular rate constant k as given below:¹⁴

$$k(M^{-1}s^{-1}) = \int_0^\infty \frac{4\pi Nr^2}{1000} [\exp(-U^r / RT)] S k_p^r dr \quad (3.18)$$

Here, the statistical orientation factor $S \leq 1$, $N =$ Avogadro's number; $R =$ Gas constant; T is the temperature and r is expressed in cm. k_p^r is the proton transfer rate constant.

Wrighton *et al.*,¹⁵ first reported the excited state proton transfer of a metal complex which gave them access to determine the pK_a of the electronically excited metal complex, pK_a^* . They examined the equilibrium constant for protonation of carboxylic acid derivatives of Ru(II) complexes. The ground state pK_a was determined by absorption spectroscopy as a function of pH in aqueous solution.

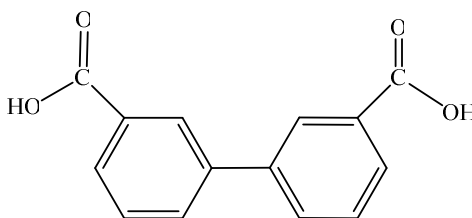


Figure 3.10 Structure of dicarboxylic acid.

The excited state equilibrium constant was measured by luminescence spectroscopy as a function of pH . The following equation can be used to estimate the pK_a^* by using the Förster cycle.

$$pK_a^* = pK_a^0 + \frac{2.86\Delta\nu}{2.3RT} \quad (3.19)$$

where $\Delta\nu$ in cm^{-1} is the difference in emission maxima of the fully protonated and deprotonated forms; R is the gas constant and T is the temperature. Equation (3.19) is derived from a Förster cycle, which is an indirect method for determining excited state equilibria. Knowledge of the ground state pK_a and the emission energies of A^* and A^*H allows an estimate of pK_a^* from the Förster cycle shown in Scheme 3.11.

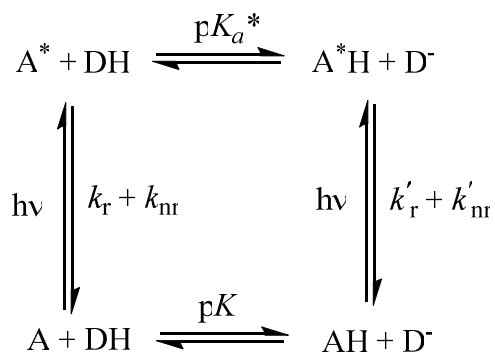
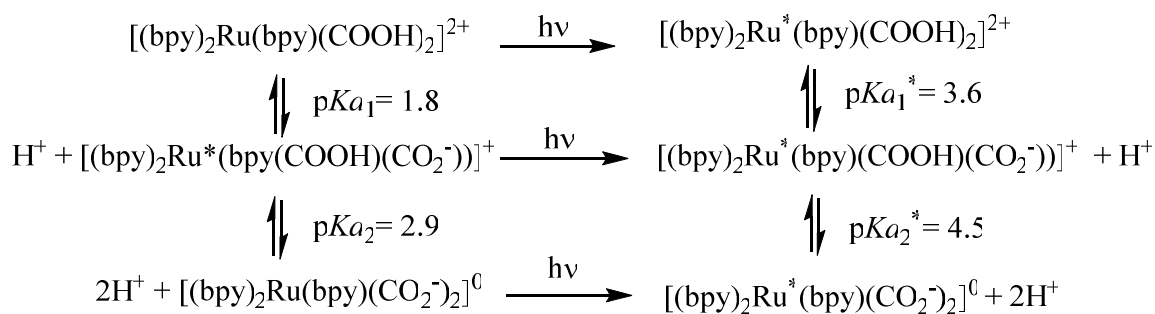


Figure 3.11 Förster cycle.¹⁵

Sasse *et al.*¹⁶ investigated the excited state proton transfer of the carboxylic acid derivatives of Ru(II) complexes. However, the results were not similar to those reported by Wrighton, previously, as only one ground state and one excited state pK_a value were observed.¹⁵ Sasse found two pK_a values for carboxylic acid derivatives of Ru(II) complexes in the ground (1.8 and 2.9) and excited states (3.6 and 4.5). This variation in pK_a in the ground and excited state might be due to the increased electron density towards the carboxylate substituents which make the O-H bond of $-\text{COOH}$ stronger in the excited state. Variation in pK_a in the ground and excited state indicate that none, one or two protons transfers take place in the excited states (Scheme 3.8).¹⁶



Scheme 3.8 Excited state proton transfer of the carboxylic acid derivatives.¹⁶

The hydrogen ion dependence of the absorption and emission spectra of bis(2,2'-bipyridyl)2,3-bis(2-pyridyl)pyrazine) ruthenium(II), $[\text{Ru}(\text{bpy})_2(\text{dpp})]^{2+}$, is evidence of the differences in the acid-base properties of the ground and emissive MLCT state of the complex.¹⁷

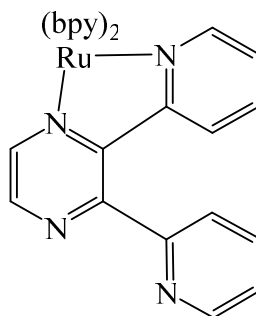
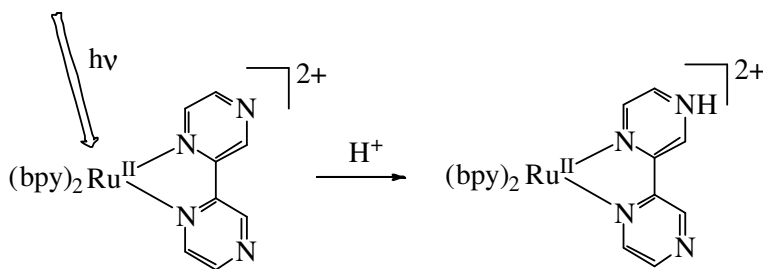


Figure 3.12 Structure of $[\text{Ru}(\text{bpy})_2(\text{dpp})]^{2+}$.

The absorption and emission spectra of $[\text{Ru}(\text{bpy})_2(\text{dpp})]^{2+}$ established that the population of the dpp localized MLCT state increases the basicity of the peripheral dpp nitrogens where most of the transferred charge resides and which take part in the excited state acid-base chemistry. Ground state protonation of the dpp peripheral pyridine of $[\text{Ru}(\text{bpy})_2(\text{dpp})]^{2+}$ is evident from the emission centered at 735 nm. In the excited state, the second protonation occurs at the dpp pyrazinyl nitrogen which shows emission

centered at 705 nm. The shortened lifetime and weaker $^3\text{MLCT}$ emission in $[\text{Ru}(\text{bpy})_2(\text{dppH}_{\text{py}})]^{3+*}$ is an expected consequence due to the energy gap law. In most cases protonation of a chromophoric ligand lowers the energy gap resulting in a red-shifted emission maximum and an increase in k_{nr} . Protonation of the $[\text{Ru}(\text{bpy})_2(\text{dppH}_{\text{py}})]^{3+}$ (ground state) yields diprotonated complexes $[\text{Ru}(\text{bpy})_2(\text{dppH}_2)]^{4+}$ which is evident from nominal changes in the absorption and emission spectra.¹⁷

Hoffman *et al.*¹⁸ studied the quenching of mixed ligand complexes $[\text{Ru}(\text{bpy})_{3-m}\text{-(bpm)}_m(\text{bpz})_z]^{2+}$ (bpy is 2,2'-bipyridine; bpm is 2,2'-bipyrimidine; bpz is 2,2'-bipyrazine; $m, z = 0-3$; $m + z \leq 3$), by H^+ in aqueous solution.



Scheme 3.9 Excited state protonation of $[\text{Ru}(\text{bpy})_2(\text{bpz})]^{2+}$.¹⁸

The one electron reduced bpm and bpz complexes can be protonated in the excited states and the $\text{p}K_a$ values are within the range of 6.3 to 9.2. It was apparent from the protonation of MLCT excited states that the lifetime and the intensities of the emissions of $[\text{Ru}(\text{bpz})_2(\text{bpm})]^{2+}$ and $[\text{Ru}(\text{bpm})_2(\text{bpz})]^{2+}$ decreased as the solution became more acidic.

3.1.7 Proton Coupled Electron Transfer

Proton transfer (PT) and electron transfer (ET) are the basis of most reactions in chemistry. Joint involvement of electron and proton transfer is termed as electron proton transfer (EPT) reactions. In the case of proton coupled electron transfer (PCET) reactions, proton and electron transfer take place together. Both PCET and EPT reactions have important roles in various types of chemical and biological processes.¹⁹⁻²³ They provide reaction pathways in which electron and proton motion are coupled, hence avoiding high energy intermediates. When the electron and proton transfer occur together as a hydrogen atom, this is known as hydrogen atom transfer (HAT) and is a common mechanism for organic free radical chemistry.²⁴ However, Savéant introduced the term CPET instead of PCET where “coupled” also means the proton transfer accompanies electron transfer in a stepwise reaction.²⁵ The coupling of electron and proton transfer influences both the energetics and dynamics of charge transfer reactions. Figure 3.13 shows a general overview of PT, ET and PCET reactions.

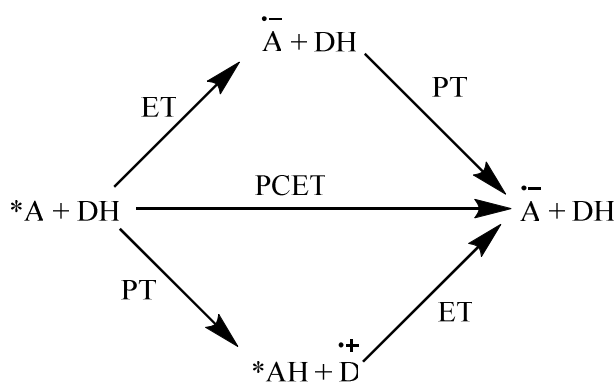
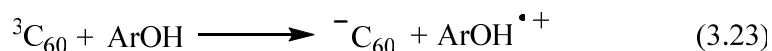
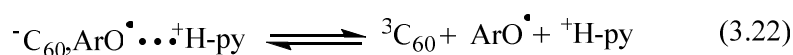
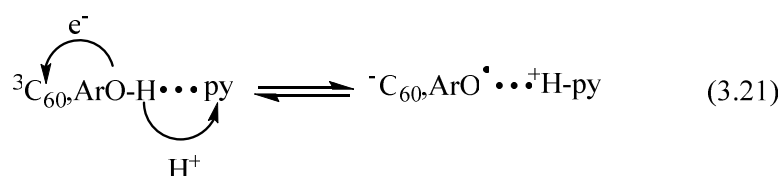
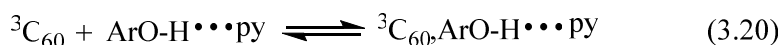


Figure 3.13 Diagram for the PT, ET, and PCET reactions.¹⁹

It is apparent from the diagram that when PT and ET reactions occur separately, there is formation of a high energy intermediate. On the other hand, proton transfer followed by an electron transfer circumvents the formation of a high energy intermediate.

For example, reduction of the triplet excited state of C_{60} , ${}^3C_{60}^*$ by phenol in the presence of base such as trimethylpyridine (TMP) (eq 3.20-3.22) can be considered.²⁶



Scheme 3.10 Quenching of ${}^3C_{60}^*$ in presence (eq 3.20-3.22) and absence (eq 3.23) of base.

In this multiple site electron proton transfer (MS-EPT) reaction, where more than one site is involved, concerted proton and electron transfer occurs in the presence of base with $k_{obs} = 6 \times 10^8 \text{ M}^{-1} \text{ s}^{-1}$. However, in the absence of base, a high-energy intermediate phenol radical is formed and $k_{obs} = 1 \times 10^6 \text{ M}^{-1} \text{ s}^{-1}$ (eqn. 3.22), which is a factor of 600 lower than that found in the presence of pyridine (eqn. 3.20). Table 3.3 shows a list of excited state quenching reactions of ${}^3C_{60}$ with various phenols, pyridine and solvent systems together with the excited state quenching of $[Ru(bpy)_3]^{2+}$ by phenol in the absence and presence of base. Also, reductive quenching of a hydrogen-bonded adduct between H_2Q and the excited state of $[Ru^{III}(bpy)_2(\text{bpz}^-)]^{2+}$, $[Ru^{III}(bpy)_2(\text{bpz}^-)]^{2+*} \cdot H_2Q$

is shown. It is evident from the table that the rate constants for the quenching reactions of the excited states of ${}^3\text{C}_{60}$ and $[\text{Ru}(\text{bpy})_3]^{2+}$ are significantly higher in presence of base than in the absence of base.²⁶

Table 3.3 Quenching reactions of excited ${}^3\text{C}_{60}$ and $[\text{Ru}(\text{bpy})_3]^{2+}$

Reaction	Solvent	$-\Delta G_{\text{app}}$	$k_{\text{qB}}, 10^7 \text{ M}^{-1} \text{ s}^{-1}$
${}^3\text{C}_{60}^* + \text{PhOH}$	Benzonitrile (PhCN)		$\leq 0.1^a$
${}^3\text{C}_{60}^* + \text{PhOH} + \text{TMP}$	PhCN	-0.07	$6.0 (\pm 0.3)^a$
${}^3\text{C}_{60}^* + \text{H}_2\text{Q}$	PhCN	-0.01	$1.2 (\pm 0.2)^a$
${}^3\text{C}_{60}^* + \text{H}_2\text{Q} + \text{TMP}$	PhCN	0.66	$270 (\pm 10)^a$
${}^3\text{C}_{60}^* + \text{H}_2\text{Q} + \text{py}$	PhCN	0.59	$330 (\pm 40)^a$
${}^3\text{C}_{60}^* + \text{catechol}$	PhCN	-0.01	$2 (\pm 0.5)^a$
${}^3\text{C}_{60}^* + \text{catechol} + \text{py}$	PhCN	0.42	$220 (\pm 30)^a$
$[\text{Ru}(\text{bpy})_3]^{2+*} + 4\text{-methyl phenol}$	MeCN		0.42^b
$[\text{Ru}(\text{bpy})_3]^{2+*} + 4\text{-methyl phenol} + \text{OH}^-$	H_2O		150^c
$[\text{Ru}(\text{bpy})_3]^{2+*} + 4\text{-(tert-butyl)phenol} + \text{OH}^-$	H_2O		120^c
$[\text{Ru}(\text{bpy})_3]^{2+*} + 4\text{-Ethylphenol} + \text{OH}^-$	H_2O		180^c
$[\text{Ru}(\text{bpy})_2(\text{bpz})]^{2+*} + \text{H}_2\text{Q}$	$\text{CH}_3\text{CN}/\text{H}_2\text{O}$	-0.55	0.45 ± 0.1^d

^a Reference 26. ^b Reference 27. ^c Reference 28. ^d Reference 29. TMP = trimethy pyridine

The free energy surfaces for PCET reactions can be presented as two dimensional paraboloids as shown in Figure 3.14.^{23a}

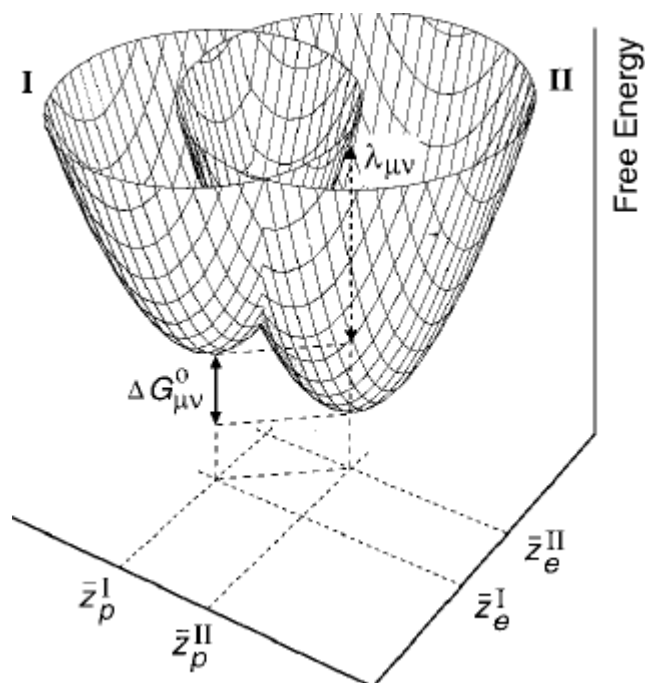
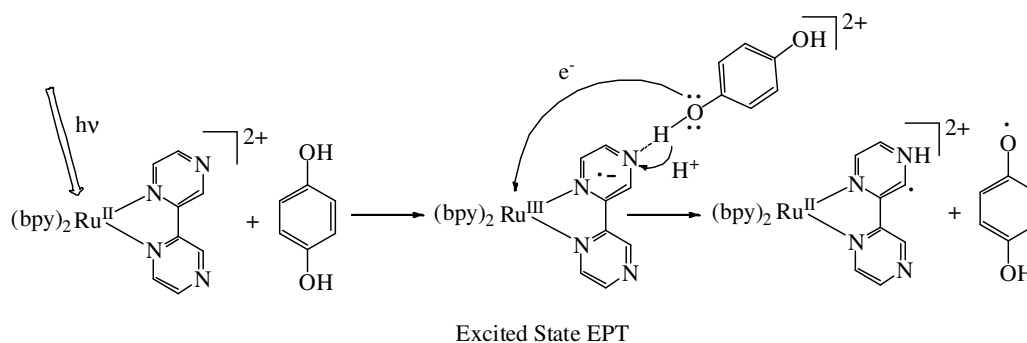


Figure 3.14 Graphical presentations of two paraboloids I $_{\mu}$ and II $_{\nu}$ as a function of the solvent coordinates Z_p and Z_e . $\lambda_{\mu\nu}$ is the reorganization energy and $\Delta G_{\mu\nu}^0$ is the equilibrium free energy difference. (Reprinted with permission from reference 29, Copyright © 2001 American Chemical Society).

At this juncture, a PCET reaction is illustrated as a transition from the reactant paraboloid set to a product paraboloid set which is a multidimensional analogue of Marcus theory for single electron transfer relating to the one dimension parabolas.³⁰

Meyer *et al.*³⁰ reported a PCET reaction which involves the reductive quenching of $[Ru^{III}(bpy)_2(bpz)^{-}]^{2+*}$ by H_2Q as shown in Scheme 3.11.

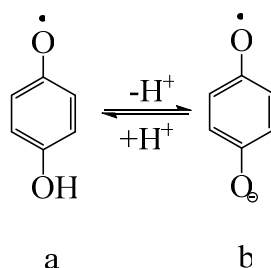


Scheme 3.11 An example of proton coupled electron transfer.³⁰

Photoirradiation of $[Ru(bpy)_2(bpz)]^{2+}$ increases the electron density of the bpz ligand in the MLCT excited states and an H-bond is formed between H_2Q and the bpz ligand of $[Ru(bpy)_2(bpz)]^{2+*}$. The quenching reaction takes place through a concerted proton transfer from H_2Q to the N of bpz and electron transfer from the oxygen of H_2Q to Ru(III) on a ~ 100 ns time scale. For the reductive quenching of $[Ru^{III}(bpy)_2(bpz^{\cdot-})]^{2+*}$ by H_2Q through electron transfer (ET), ΔG° is +0.06 eV. However, when the quenching process occurs through electron proton transfer (EPT), ΔG° is -0.55 eV, which reveals that EPT avoids high energy ET or PT intermediates. Later on, Meyer and co-workers³¹ extended their investigation and studied the pH dependence of the excited state of a PCET reaction that involves reductive quenching of the MLCT excited state of $[Ru(bpy)_2(bpz)]^{2+}$ by a series of substituted hydroquinones with transient absorption (TA) and time resolved electron paramagnetic resonance spectroscopy (TREPR). TREPR is a useful technique to detect radical (HQ^\cdot) without the interference of the ligand-based radical $[Ru^{II}(bpy)_2(bpzH^\cdot)]^{2+}$, as this radical is TREPR silent due to rapid electron spin relaxation induced by the metal center. Modification of the substituent on H_2Q ring can

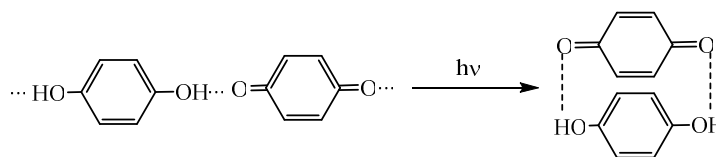
influence the acid/base dependence of a PCET reaction. Laser, flash photolysis results revealed that in strong basic solutions and with an electron withdrawing group on the H₂Q ring system, the mechanism changes from a PCET to direct ET quenching. On the other hand, variation of ligands on the Ru complex can alter the acid/base dependence of the PCET through a series of complex equilibria between protonated and deprotonated hydroquinone radicals and anions.³¹

In CH₃CN, HQ[•] exists as an organic radical as illustrated in Scheme 3.12(a). However, in CH₃CN/H₂O system, deprotonation of HQ[•] results in formation of a semiquinone anion radical as shown in Scheme 3.12(b).²⁶



Scheme 3.12 HQ[•] radical in equilibrium in CH₃CN/H₂O.

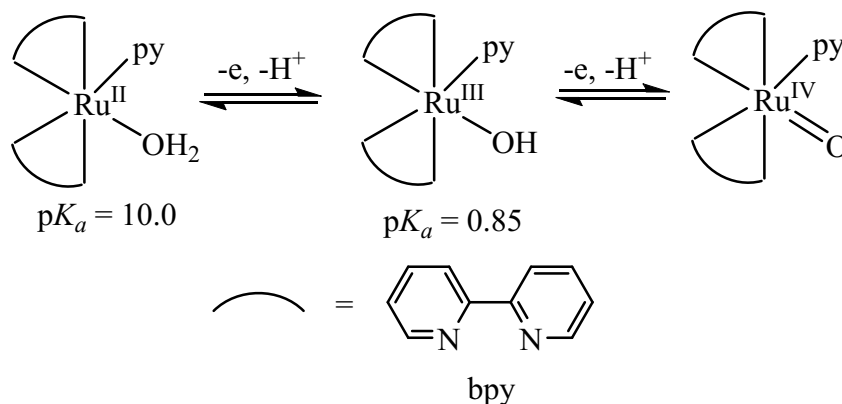
Hydroquinones have been identified as H-bonded charge transfer complexes.¹⁹ Quinone and hydroquinone interact with each other through the formation of H-bonds in concentrated solutions as shown in Scheme 3.13. This is evident from the low energy absorption bands that arise due to the H₂Q→Q charge transfer as shown below.



Scheme 3.13 H-bonded charge transfer in Hydroquinones.²²

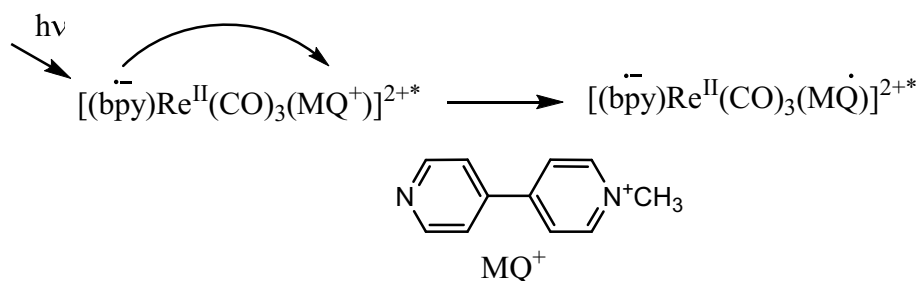
3.2 Thermodynamics of PCET Reactions

When electron transfer occurs in concert with proton transfer, the net result is that the formation of high-energy intermediates is circumvented (section 3.1.7). Electron transfer, along with proton transfer has an important effect on the rate of a reaction. Electron transfer increases acidity with a loss of an electron and eventually influences the redox potentials of a reaction. However, there are some limiting cases where the pK_a value is lower as the oxidation number increases. For $[Ru^{II}(bpy)_2(py)(H_2O)]^{2+}$,¹⁹ the pK_a value is 10.7; whereas in higher oxidation state or $[Ru^{III}(bpy)_2(py)(OH)]^{2+}$ the value is remarkably lower at 0.85, Scheme 3.14.



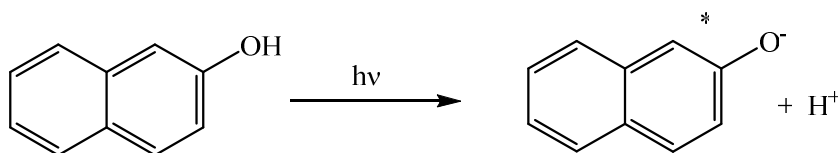
Scheme 3.14 Variation of pK_a value with change in oxidation number.

For $[Re(bpy)(CO)_3(MQ^+)]^{2+}$,²⁰ the excited state is more basic than the ground state. Here, intramolecular $\pi^*(bpy^{-*}) \rightarrow \pi^*(MQ^+)$ electron transfer takes place in the excited state as shown in Scheme 3.15.



Scheme 3.15 Excited state reaction of $[Re(bpy)(CO)_3(MQ^+)]^{2+}$.

In the ground state 2-naphthol²¹ has the pK_a value ~ 8 , whereas in the excited state the pK_a^* value is ~ 2.8 , Scheme 3.16.



Scheme 3.16 Excited state reaction of 2-naphthol.

A pH dependent redox couple is given by the following equation



where Ox is the oxidized species and Red is the reduced species. The half-wave potential ($E_{1/2}$) can be predicted by the Nernst equation,¹⁹ having pH dependency, is given by

$$E_{1/2} = E^{o'} - [0.059/n] \log(D_o/D_r)^{1/2} - 0.059(m/n)pH \quad (3.25)$$

where D_o and D_r are the respective diffusion coefficients of the oxidized and reduced species, m is the number of protons, n is the number of electrons, $E^{o'}$ is the formal potential at $pH = 0$. The dependence of redox potentials upon hydrogen ion concentration can be conveniently plotted and a plot of $E_{1/2}$ vs pH for a redox couple which is known as

a Pourbaix diagram. The Pourbaix diagram summarizes equilibrium information of oxidation-reduction reactions that take place in a solution.²²

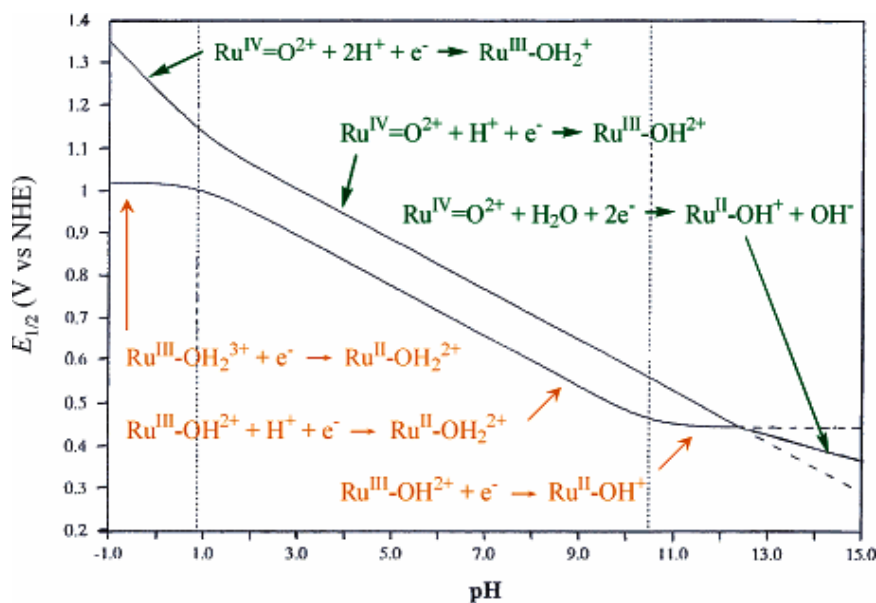
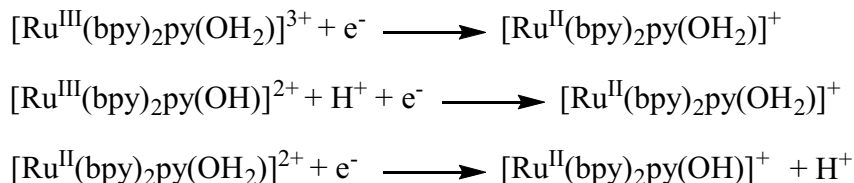


Figure 3.15 Pourbaix diagram for Ru(IV/III) and Ru(III/II) couples of $[\text{Ru}^{\text{II}}(\text{bpy})_2(\text{py})(\text{H}_2\text{O})]^{2+}$. (Reprinted with permission from reference 22, Copyright © 2007 American Chemical Society).

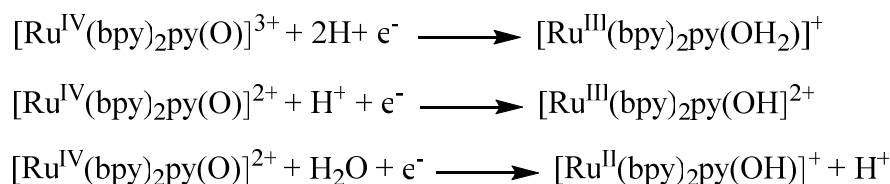
The Pourbaix diagrams for the $\text{cis}-[\text{Ru}^{\text{IV}}(\text{bpy})_2(\text{py})(\text{O})]^{2+}/[\text{Ru}^{\text{III}}(\text{bpy})_2(\text{py})(\text{OH})]^{2+}$ and $\text{cis}-[\text{Ru}^{\text{III}}(\text{bpy})_2(\text{py})(\text{OH})]^{2+}/[\text{Ru}^{\text{II}}(\text{bpy})_2(\text{py})(\text{H}_2\text{O})]^{2+}$ couples is shown in Figure 3.15 where the variation of $E_{1/2}$ with pH for the Ru(IV/III) and Ru(III/II) couples of $[\text{Ru}^{\text{II}}(\text{bpy})_2(\text{py})(\text{H}_2\text{O})]^{2+}$ are summarized. The vertical dotted lines indicate $pK_a = 10.6$ for $\text{cis}-[\text{Ru}^{\text{II}}(\text{bpy})_2(\text{py})(\text{H}_2\text{O})]^{2+}$ ($\text{Ru}^{\text{II}}\text{-OH}_2^{2+}$) and $pK_a = 0.85$ for $\text{cis}-[\text{Ru}^{\text{III}}(\text{bpy})_2(\text{py})(\text{H}_2\text{O})]^{3+}$ ($\text{Ru}^{\text{III}}\text{-OH}_2^{3+}$). $\text{Cis}-[\text{Ru}^{\text{IV}}(\text{bpy})_2(\text{py})(\text{O})]^{2+}$ and $\text{cis}-[\text{Ru}^{\text{III}}(\text{bpy})_2(\text{py})(\text{OH})]^{2+}$ are given as ($\text{Ru}^{\text{IV}}=\text{O}^{2+}$) and ($\text{Ru}^{\text{III}}\text{-OH}^{2+}$), respectively in the diagram. Over the range of pH 2-9, $\text{cis}-[\text{Ru}^{\text{II}}(\text{bpy})_2(\text{py})(\text{H}_2\text{O})]^{2+}$ and $\text{cis}-[\text{Ru}^{\text{III}}(\text{bpy})_2(\text{py})(\text{OH})]^{2+}$ species predominate for the

Ru(III/II) couple. The $E_{1/2}$ decreases with pH by $0.05916 \text{ V}/pH$. The reactions are given in Scheme 3.17:



Scheme 3.17 Reactions for Ru(III/II) couples of $[Ru^{II}(bpy)_2(py)(H_2O)]^{2+}$.

In contrast, at $pH < 0.85$, $cis\text{-}[Ru^{IV}(bpy)_2(py)(O)]^{2+}$ and $cis\text{-}[Ru^{III}(bpy)_2(py)(OH)]^{2+}$ species dominate for Ru(IV/III) couple. The reactions are given in Scheme 3.18:



Scheme 3.18 Reactions for Ru(IV/III) couples of $[Ru^{II}(bpy)_2(py)(H_2O)]^{2+}$.

$E_{1/2}$ decreases with pH by $118 \text{ mV}/pH$ as the pH is decreased as shown in the diagram. This is in agreement with the loss of two protons when oxidation takes place.

The pH dependence of H_2Q redox couples can also be represented as in Pourbaix diagrams. For example, in the quinone/hydroquinone (Q/H_2Q) system, the equilibrium between quinone (Q) and hydroquinone (H_2Q) involves a one electron oxidation semiquinone intermediate HQ^\bullet , as shown in the Figure 3.16.³² In strong acidic solutions, the quinone is protonated to give a QH^+ species and the equilibrium is represented by the vertical line at $pH = pK_a = -1$. At higher pH , hydroquinone undergoes two consecutive

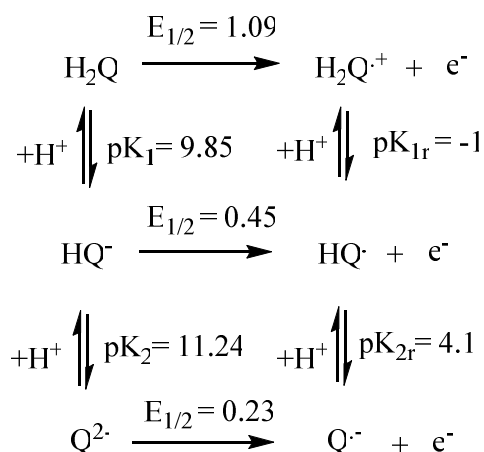


Figure 3.17 Quinone/hydroquinone (Q/H₂Q) system.

3.3 Other Excited State Measurements

At room temperature, $[\text{Ru}(\text{tpy})_2]^{2+}$ is non-emissive with a lifetime of 250 ps in H₂O.³³ The luminescence lifetime for $[\text{Ru}(\text{tpy})_2]^{2+}$ is 8.0 μs in H₂SO₄/H₂O and HSO₃F/H₂O glasses (25% v/v) at 77 K, and 10.2 μs in D₂SO₄/D₂O (25% v/v).³³ However, $[\text{Ru}(\text{bpy})_3]^{2+}$ and $[\text{Ru}(\text{tpy})_2]^{2+}$ do not display any thermal or photochemical reactivity in these strongly acidic media at room temperature. The addition of moderate concentrations of the powerful oxidizing agent $[\text{Fe}(\text{OH})_6]^{3+}$ leads to accelerated and highly non-exponential $[\text{Ru}(\text{tpy})_2]^{2+}$ decay kinetics where the electron transfer driving force is greater than 1.5 eV in aqueous solution.

H₂O as a medium for electron transfer has a unique position as it plays an important role in many chemical and biological reactions. However, the large dielectric constant of H₂O creates a barrier for electron transfers.³³ The efficiency of H₂O as a tunnelling medium has not been clearly reported. From this motivation, Gary *et al.*,³³ investigated electron transfer in aqueous acidic glasses to identify β values, an

exponential distance decay constant (β) that is sensitive to the composition of the medium separating the electron donor (D) and acceptor (A). Figure 3.18 shows the luminescence decay kinetics for $[\text{Ru}(\text{tpy})_2]^{2+}$ in the absence and presence of $[\text{Fe}(\text{OH}_2)_6]^{3+}$ where the traces are for 0.0, 0.05, 0.10, 0.25, 0.50 M from top to bottom.

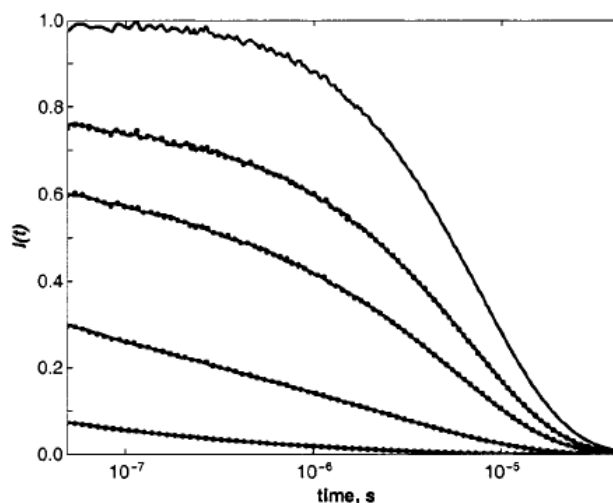


Figure 3.18 Luminescence decay kinetics for $\text{Ru}(\text{tpy})_2^{2+}$ in a $\text{H}_2\text{SO}_4/\text{H}_2\text{O}$ glass (at 77 K) in the presence of $[\text{Fe}(\text{OH}_2)_6]^{3+}$.³³ (Reprinted with permission from reference 33, Copyright © 2000 American Chemical Society).

3.4 Effect of Deuteration on Radiative and Non-radiative Decay

Deuteration of ligands in a transition metal complex plays an important role on the excited state decay.³⁴ The position of deuteration on a 2,2'-bpy yields important insights into the mechanism for non-radiative decay processes.³⁴ The deuteration of ruthenium polypyridyl complexes enhances their luminescent quantum yield and excited state lifetime.³⁴ Van Houten and Watts reported³⁴ that the deuteration of $[\text{Ru}(\text{bpy})_3]^{2+}$ increases the lifetime of $^3\text{MLCT}$ states, with $k_H/k_D \sim 1.3$. The effect of deuteration has been explained by Van Houten and Watts in terms of an excited state model concerning partial

charge transfer to the solvent (CTTS), which was incorrect.³⁴ However, this interpretation has been revised by Kincaid *et al.*,³⁵ and the position of deuteration was considered to be attenuated by the promoting modes that mix the thermalized ³MLCT ground state transition. Kincaid experimentally illustrated the lifetime differences for three isotopically substituted analogs of $[\text{Ru}(\text{bpy})_3]^{2+}$ and determined the lifetime and non-radiative decay constants given in the Table 3.4.³⁵

Table 3.4 ³MLCT lifetime and k_{nr} values for substituted $[\text{Ru}(\text{bpy})_3]^{2+}$.³⁵

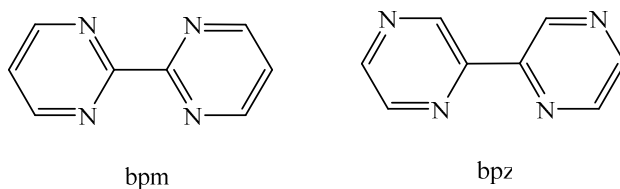
Complex	lifetime \pm 10ns in H ₂ O	k_{nr} s ⁻¹
$[\text{Ru}(\text{bpy})_3]^{2+}$	580	12.2×10^5
$\text{Ru}(\text{bpy}-d_8)_3^{2+}$	690	9.45×10^5
$\text{Ru}(\text{bpy}-3,3'-d_2)_3^{2+}$	580	12.2×10^5
$\text{Ru}(\text{bpy}-6,6'-d_2)_3^{2+}$	645	10.5×10^5
$\text{Ru}(\text{bpy}-3,3', 5,5'-d_4)_3^{2+}$	655	10.3×10^5

As shown in the table, deuteration at the 3,3'-positions has no significant effect on k_{nr} , while other deuterated complexes reveal lifetimes that are longer and k_{nr} values that are lower than that of $[\text{Ru}(\text{bpy})_3]^{2+}$. This is due to the low electron density at the 3,3'-positions as H/D exchange occurs on the metal complex at these positions.³⁵

3.5 Objectives

In heteroleptic ruthenium polypyridyl complexes containing bpy and N heterocycles such as 2,2'-bipyrimidine (bpm) and 2,2'-bipyrazine (bpz), the bpm and bpz ligands offer external N-atoms which can act as proton acceptors as shown in Scheme 3.11.

Likewise, there is a pendant pyridine in $[\text{Ru}(\text{bpy})_2(\eta^2\text{-tpy})]^{2+}$, which possesses an external N-atom.



In chapter 2 the fluxional behaviour of tpy in $[\text{Ru}(\text{bpy}-d_8)_2(\eta^2\text{-tpy})]^{2+}$ was discussed. The purpose of this chapter is as follows:

- i) To obtain fundamental insight into electronic coupling on the excited state surface of the protonated pendant pyridine ring in $[\text{Ru}(\text{bpy})_2(\eta^2\text{-tpy})]^{2+}$.
- ii) Explanation of the novel photophysics of $[\text{Ru}(\text{bpy})_2(\eta^2\text{-tpy})]^{2+}$ and its protonated form.
- iii) To study the effect of conformational changes on the photophysical properties of $[\text{Ru}(\text{bpy})_2(\eta^2\text{-tpy})]^{2+}$ *i.e.* to observe if there is any relationship between the ground state fluxionality and k_{nr} .
- iv) As the pendant pyridine in $[\text{Ru}(\text{bpy})_2(\eta^2\text{-tpy})]^{2+}$ contains an external N-atom, it might also open a new direction to study electron-proton transfer (EPT) reactions.

3.6 Results

3.6.1 Steady-State Absorption, Emission and Excited State Redox Potentials

Comparative ground state physical properties of $[\text{Ru}(\text{bpy})_2(\text{L})]^{n+}$ (where L = dpp, 2-phenylphen, 6-Mebpy, 6-bpy-cyclamM (M = Ni^{2+} or 2H^+) as shown in Figure 3.19) are collected in Table 3.5.

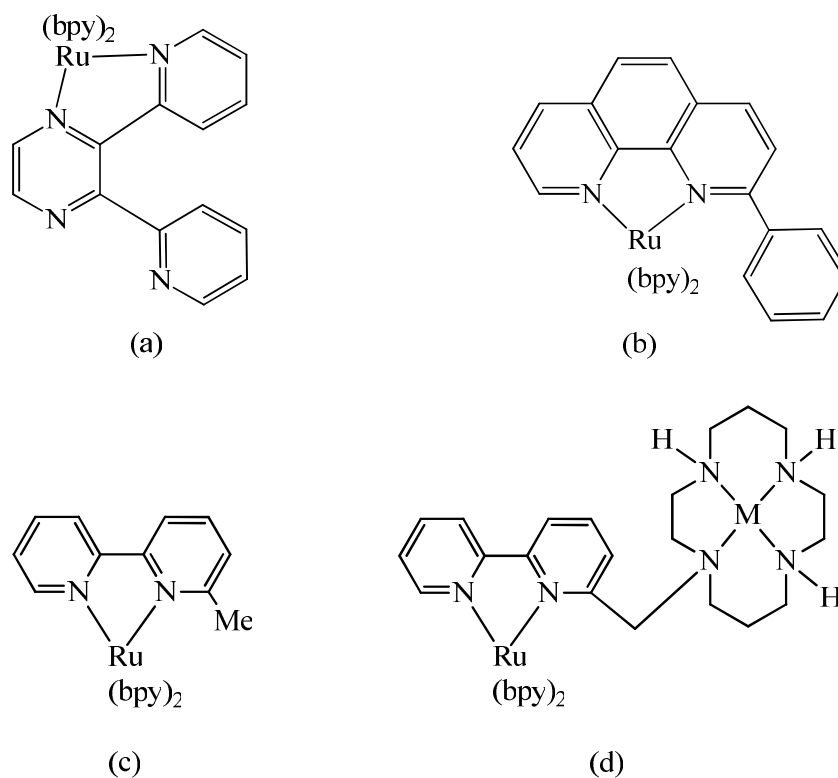


Figure 3.19 Structures for (a) $[\text{Ru}(\text{bpy})_2\text{dpp}]^{2+}$ (b) $[\text{Ru}(\text{bpy})_2(2\text{-phenyl-phen})]^{2+}$ (c) $[\text{Ru}(\text{bpy})_2(6\text{-Mebpy})]^{2+}$ and (d) $[\text{Ru}(\text{bpy})_2(6\text{-bpy-cyclamM})]^{2+}$ (M = Ni^{2+} or 2H^+).

The overlaid UV-vis spectra of $[\text{Ru}(\text{bpy})_2(\eta^2\text{-tpy})]^{2+}$ and $[\text{Ru}(\text{bpy})_3]^{2+}$ and assignments of the electronic transitions are shown in Figure 3.20.

Table 3.5 Physical properties of $[\text{Ru}(\text{bpy})_2(\text{L})]^{2+}$

L =	bpy ^a	Mebpy ^a	bpy-cyclamH ₂ ^a	η^2 -tpy ^b	2-phenyl-phen ^c
λ_{max} , nm($\epsilon \times 10^{-3}$) Lowest Energy Transition	451(14.4)	450(14.3)	448(12.1)	448 (14.0)	447(4.28)
$E_{1/2}$, (Ru ^{III/II}) vs SCE	1.27	1.27	1.34	1.30 ^c	1.32
$E_{1/2}$, (Ru ^{IV/I}) vs SCE	-1.34	-1.34	-1.33	-1.33 ^c	-1.28
Ru-N bond distance, Å	av. 2.056		av. 2.076	av. 2.083	av. 2.075

^a Reference 36. ^b For $[\text{Ru}(\text{bpy})_2(\eta^2\text{-tpy})]^{2+}$ $\lambda_{\text{max}}^{\text{abs}} = 448$ nm, $\epsilon = 14086 \text{ M}^{-1}\text{cm}^{-1}$. ^c The Ru^{III/II} and Ru^{IV/I} redox potentials are the average of the reduction potentials for $[\text{Ru}(\text{bpy})_2(6\text{-Mebpy})]^{2+}$ and $[\text{Ru}(\text{bpy})_2(\text{bpy-cyclam})]^{2+}$. ^c Reference 40.

The visible spectra of the $[\text{Ru}(\text{bpy})_2(\eta^2\text{-tpy})]^{2+}$ and $[\text{Ru}(\text{bpy})_3]^{2+}$ in CH_3CN are dominated by the well-documented $[(d\pi)^6] \rightarrow {}^1[(d\pi)^5(\pi_1^*)^1]$ MLCT transitions at ~ 450 nm and ligand based $\pi \rightarrow \pi^*$ transitions in the 270-300 nm region.³⁷ The MLCT envelopes ($\lambda_{\text{max}}^{\text{abs}} = 400\text{-}500$ nm) are broad due to a series of MLCT transitions and their associated vibronic progression ($\hbar\omega_j \sim 1600$ cm^{-1}).³⁷

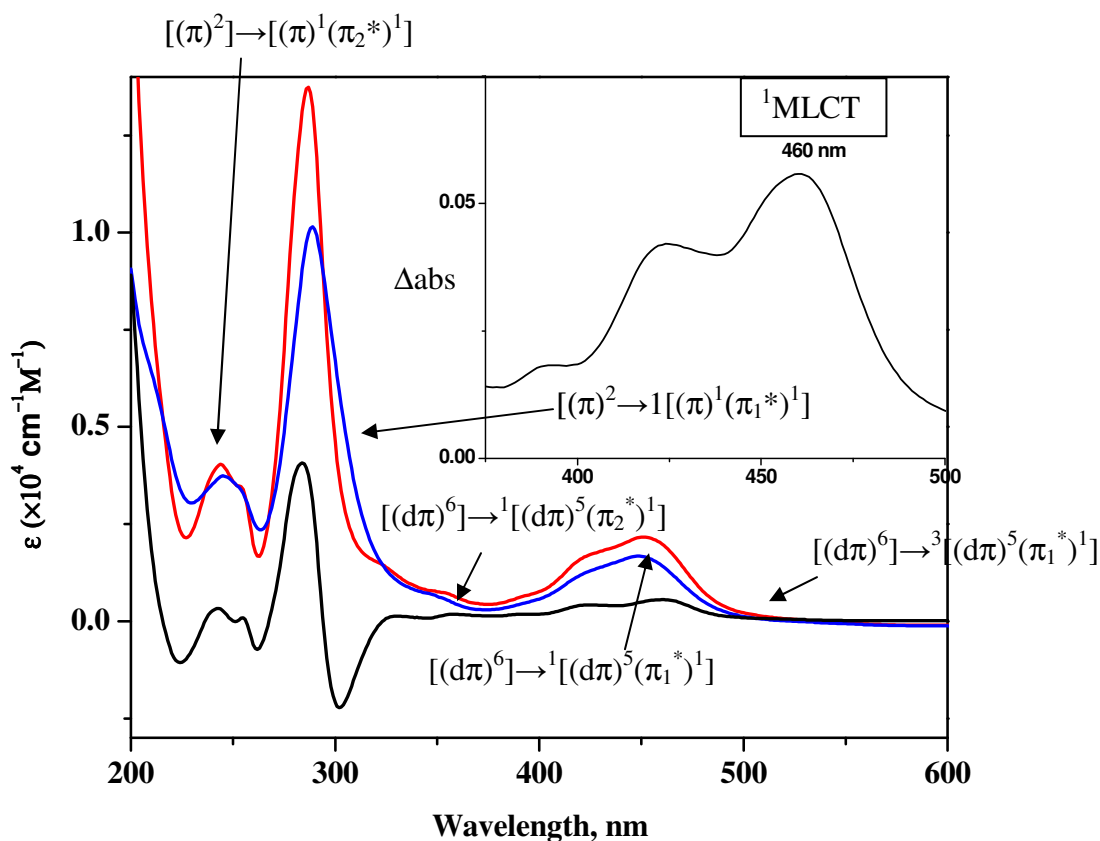


Figure 3.20 Overlaid UV-vis absorption spectra of $[\text{Ru}(\text{bpy})_2(\eta^2\text{-tpy})]^{2+}$ (blue) (1.1×10^{-6} M) and $[\text{Ru}(\text{bpy})_3]^{2+}$ (red) (1.3×10^{-6} M) in CH_3CN at $298 (\pm 3)$ K. Calculated difference spectrum (black) between $[\text{Ru}(\text{bpy})_3]^{2+}$ and $[\text{Ru}(\text{bpy})_2(\eta^2\text{-tpy})]^{2+}$ is enlarged in the inset.

The absorption spectrum of $[\text{Ru}(\text{bpy})_2(\eta^2\text{-tpy})]^{2+}$ displays a similar broad metal-to-ligand charge transfer (MLCT) absorption band with λ_{max} at ~ 450 nm

($\hbar\omega \sim 1600 \text{ cm}^{-1}$) to the absorption of $[\text{Ru}(\text{bpy})_3]^{2+}$ in same solvent ($\sim 3\text{-}5 \text{ nm}$ blue shifted), inset Figure 3.20. The absorption (ΔA) difference between the bands 460 nm and 422 nm is $0.013 \text{ cm}^{-1}\text{M}^{-1}$; and for 422 nm and 390 nm, the difference is $0.024 \text{ cm}^{-1}\text{M}^{-1}$. The MLCT maxima and extinction coefficients in Table 3.5 for $[\text{Ru}(\text{bpy})_2(\text{L})]^{n+}$ analogous (where L = bpy, 6-Mebpy, 6-bpy-cyalamM, $\eta^2\text{-tpy}$, 2-phenylphen ligands) as shown above, have similar MLCT energetics and intensities.

In the weak coupling limit the ground state absorption should be comparable to that of $[\text{Ru}(\text{bpy})_3]^{2+}$, Figure 3.20. It should be noted that the similarity of the UV-vis spectra of $[\text{Ru}(\text{bpy})_2(\eta^2\text{-tpy})]^{2+}$ and $[\text{Ru}(\text{bpy})_3]^{2+}$ point to weak coupling between the pendant pyridine and the $[\text{Ru}(\text{bpy})_3]$ like coordination sphere in $[\text{Ru}(\text{bpy})_2(\eta^2\text{-tpy})]^{2+}$ in the ground state. The crystal structure yields a dihedral angle of 52° between the pendant pyridine and bpy fragment. The UV $\pi \rightarrow \pi^*$ transitions for the $\eta^2\text{-tpy}$ system vary slightly in intensities with a heteroleptic mixed ligand Ru(II) complex as expected.³⁸ The low energy tail is assigned to a spin forbidden $[(d\pi)^6 \rightarrow^3[(d\pi)^5(\pi_1^*)^1]]$ transition which gains intensity due to mixing of the $^1\text{MLCT}$ and $^3\text{MLCT}$ states by spin-orbit coupling.³⁹ As such, the use of spin labels is an approximation.

The absorption and emission spectra of $[\text{Ru}(\text{bpy})_2(\eta^2\text{-tpy})]^{2+}$ in CH_3CN solution are shown in Figure 3.21. The $^3\text{MLCT}$ emission from $[\text{Ru}(\text{bpy})_2(\eta^2\text{-tpy})]^{2+}$ with λ_{em}^{\max} at 615 nm is much weaker ($\Phi_{em} = 7.2 \times 10^{-5}$) than the emission of $[\text{Ru}(\text{bpy})_3]^{2+}$ ($\Phi_{em} = 0.062$), but there is no apparent shift in the energy of the $^3\text{MLCT} \rightarrow$ ground state transition. The values are quite distinct from those measured by Schmechl *et al.*⁴⁰ for most

of the $[\text{Ru}(\text{bpy}-d_8)_2(\text{phen}-\text{R})]^{2+}$ complexes in CH_3CN where $\phi_{\text{em}} \sim 7 \times 10^{-5}$. It should be noted that the rigidity of the phen ligand results in increased lifetimes and emission quantum yields.⁴¹ The similarity of absorption and emission data compared to $[\text{Ru}(\text{bpy})_3]^{2+}$ spectroscopic data confirm that in solution $[\text{Ru}(\text{bpy})_2(\eta^2\text{-tpy})]^{2+}$ has a six coordinated structure with three bidentate ligands. The X-ray structures in the solid state are described in chapter two.

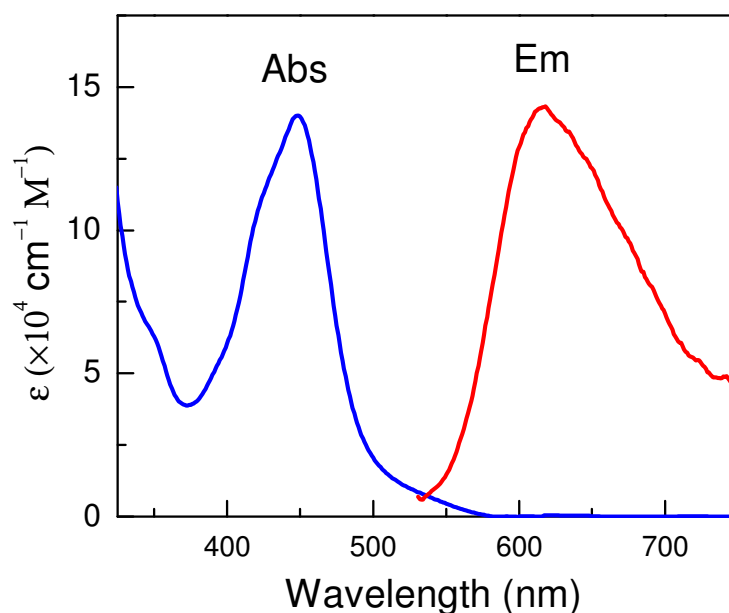


Figure 3.21 Absorption (blue) and emission (red) spectra of $[\text{Ru}(\text{bpy})_2(\eta^2\text{-tpy})]^{2+}$ in acetonitrile at $298 (\pm 3)$ K, under 1 atm Ar.

Comparative excited state properties of $[\text{Ru}(\text{bpy})_2(\text{L})]^{n+}$ complexes (where L is a 6-R-bpy ligand; R = H, Me, 6-cyclam, py) are given in Table 3.6. Room temperature luminescence is observed from all $[\text{Ru}(\text{bpy})_2(\text{L})]^{n+}$ complexes with maxima between 600 and 625 nm.

Table 3.6 Excited State Properties of $[\text{Ru}(\text{bpy})_2(\text{L})]^{2+}$ complexes in CH_3CN

L =	2-phenyl-phen ^c	bpy	6-Mebpy ^a	6-cyclam-bpy ^a	$\eta^2\text{-tpy}^b$
λ_{em}^{max}, nm (eV)	622 (2.0)	620 (2.0)		621 (1.98)	615 (2.05)
ϕ_{em}	7×10^{-4}	0.062			7×10^{-5}
τ, ns (298 K)	5	670	8	2	0.082
τ, ns (165 K)		1920	1600	1200, 170	
$E_{1/2}, (\text{Ru}^{\text{III/II}^*})$ Vvs SCE	-0.68	-0.92		-0.64	-0.74 ^c
$E_{1/2}, (\text{Ru}^{\text{II}^*/\text{I}})$ Vvs SCE	+0.72	+0.85		+0.64	+0.74 ^c

^a Reference 36. ^b The $\text{Ru}^{\text{III/II}^*}$ and $\text{Ru}^{\text{II}^*/\text{I}}$ excited state redox potentials are calculated using equation 3.28 and 3.29. See text for details. ^c Reference 40.

The estimated reduction potentials for the excited states acting as oxidants



or reductants



are included in Table 3.6. The excited state reduction potentials were calculated from the ground-state potentials by using the following equation.³⁰

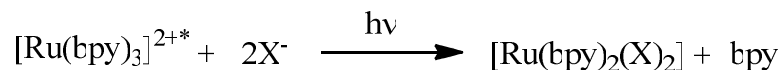
$$E_{1/2}(\text{Ru}^{\text{II}*/\text{I}}) = E_{1/2}(\text{Ru}^{\text{II}/\text{I}}) + E_{\text{em}}^{\text{max}} \quad (3.28)$$

$$E_{1/2}(\text{Ru}^{\text{III}/\text{II}*}) = E_{1/2}(\text{Ru}^{\text{III}/\text{II}}) - E_{\text{em}}^{\text{max}} \quad (3.29)$$

The $E_{1/2}$ and $E_{\text{em}}^{\text{max}}$ are the ground state redox potentials and emission maxima of $[\text{Ru}(\text{bpy})_2(\eta^2\text{-tpy})]^{2+}$ in Volts, respectively.

3.6.2 Photochemistry

Steady-state photolysis of $[\text{Ru}(\text{bpy})_3]^{2+}$ in the presence of a series of anions (such as Cl^- , Br^- , NCS^-)³⁰ leads to photoinduced ligand substitution given by



Scheme 3.19 Photoinduced ligand substitution reaction.

$[\text{Ru}(\text{bpy})_2(\eta^2\text{-tpy})]^{2+}$ was photolyzed with broad band light excitation (400 W Xe Arc Lamp) and no significant changes were observed in the UV-vis spectrum over a period of one hour, under 1 atm N_2 . No photochemistry occurred for $[\text{Ru}(\text{bpy})_2(\eta^2\text{-$

$\text{tpy}]^{2+}$, which implies that the complex is relatively inert to photosubstitution in line with the observations described by Schmechl for $[\text{Ru}(\text{bpy})_2(2\text{-phenylphen})]^{2+}$.⁴⁰ This is an important observation given the steric demands of the tpy ligand, yet the compound appears to be photoinert. This point will be elaborated on below.

3.6.3 Time-Resolved Spectroscopy

Transient absorption difference spectra obtained following laser flash excitation of $[\text{Ru}(\text{bpy})_2(\eta^2\text{-tpy})]^{2+}$ are shown in Figure 3.22.

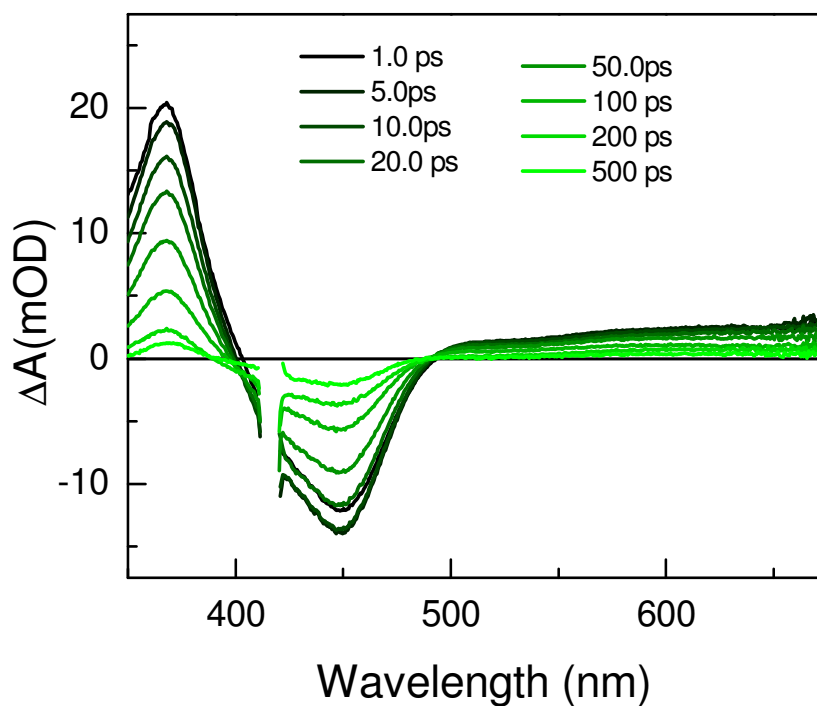


Figure 3.22 Transient absorption spectra for $[\text{Ru}(\text{bpy})_2(\eta^2\text{-tpy})]^{2+}$ where where $\lambda_{\text{exc}} = 405$ nm in CH_3CN at $298 (\pm 3)$ K.

At the earliest time the transient absorption difference spectra displayed a prompt growth which is assigned to a $(\pi \rightarrow \pi^*)$ transition of a reduced $\text{bpy}^{\cdot-}$ ligand at $\lambda = 370$. There is concomitant bleaching at 460 nm which is due to loss of the $[(d\pi^6 \rightarrow {}^1[d\pi]^5\pi_1^*)]$ ground state absorption. Furthermore, there is a prompt weak transient absorption that extends from 460 to 650 nm, which is assigned to an excited state $[\pi^2(d\pi)^5 \rightarrow \pi(d\pi)^6]$ LMCT.³⁰ The TA spectra evolve in time and the spectral features closely parallel those found for $[\text{Ru}(\text{bpy})_3]^{2+}$, however, the lifetime is five orders of magnitude larger than that of $[\text{Ru}(\text{bpy})_3]^{2+}$.³⁰ Following excitation and inter system crossing (ISC) to the emissive ${}^3[\text{MLCT}]$ state one observes an exponential decay with a life-time of 82 ps with a point at ~ 470 nm ($\Delta A(\text{mOD}) = 0$) which is consistent with a single kinetic step without detectable formation of transient intermediates (Figure 3.23). The kinetics were found to be independent of excitation and monitoring wavelength.

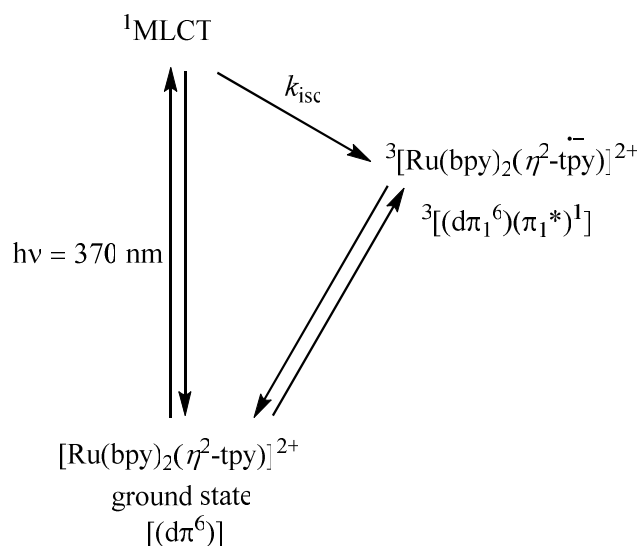


Figure 3.23 Diagram for the excitation and relaxation of $[\text{Ru}(\text{bpy})_2(\eta^2\text{-tpy})]^{2+}$.

The excited state emission lifetime of $[\text{Ru}(\text{bpy})_2(\eta^2\text{-tpy})]^{2+}$ in CH_3CN , is shown in Figure 3.24.

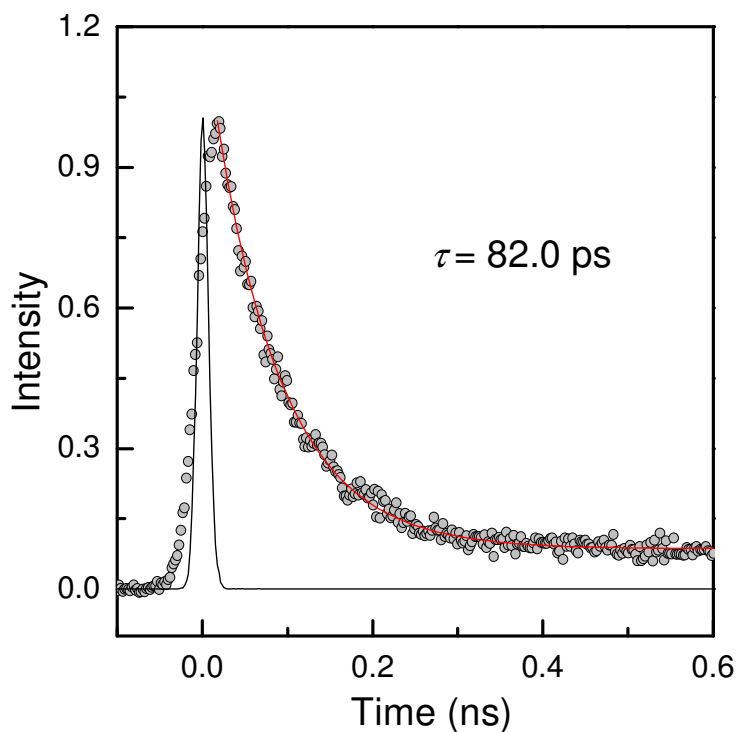


Figure 3.24 Emission lifetime spectrum for $[\text{Ru}(\text{bpy})_2(\eta^2\text{-tpy})]^{2+}$, where $\lambda_{exc} = 365 \text{ nm}$; $\lambda_{max} = 620 \text{ nm}$ in CH_3CN at $298 (\pm 3) \text{ K}$. The time-resolved emission of $[\text{Ru}(\text{bpy})_2(\eta^2\text{-tpy})]^{2+}$ with fitting (solid)

3.6.4 Protonation of Pendant Pyridine

Addition of two equivalents of trifluoroacetic acid (TFA) to a CH_3CN solution containing $[\text{Ru}(\text{bpy})_2(\eta^2\text{-tpy})]^{2+}$ results in subtle changes in the intensity of the $[(d\pi)^6 \rightarrow (d\pi)^5(\pi_1^*)^1]$ envelope, Figure 3.25. The addition of TFA gives rise to increased absorptivity between 325 nm and $\sim 540 \text{ nm}$.

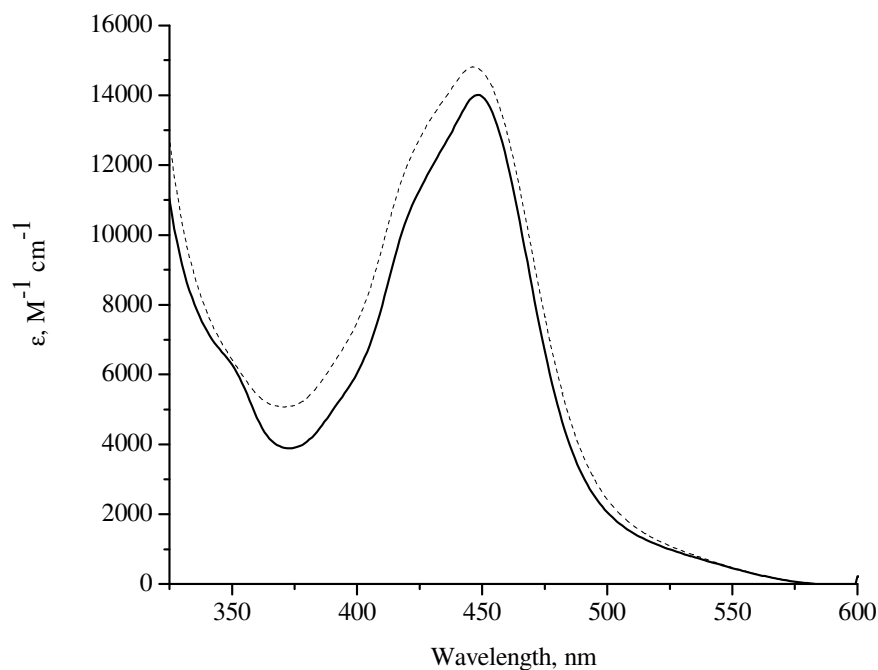
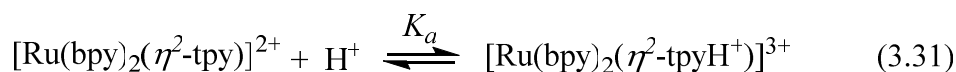


Figure 3.25 UV-vis spectra for $[\text{Ru}(\text{bpy})_2(\eta^2\text{-tpy})](2.49 \times 10^{-5} \text{ M})$, before (—) and after (---) the addition of two equivalents of TFA; $[\text{TFA}] = 0.1 \text{ M}$ in CH_3CN at $298 (\pm 3) \text{ K}$, under 1 atm N_2 .

These spectral changes are due to the protonation of the pendant pyridine $[\text{Ru}(\text{bpy})_2(\eta^2\text{-tpy})]^{2+}$ given by



The equilibrium constant for the protonation of the pendant pyridine is

$$K_a = \frac{[[\text{Ru}(\text{bpy})_2(\eta^2\text{-tpy})]^{3+}]}{[[\text{Ru}(\text{bpy})_2(\eta^2\text{-tpy})]^{2+}][\text{H}^+]} \quad (3.32)$$

There is evidence for several new transitions based in the difference spectrum shown in Figure 3.26.

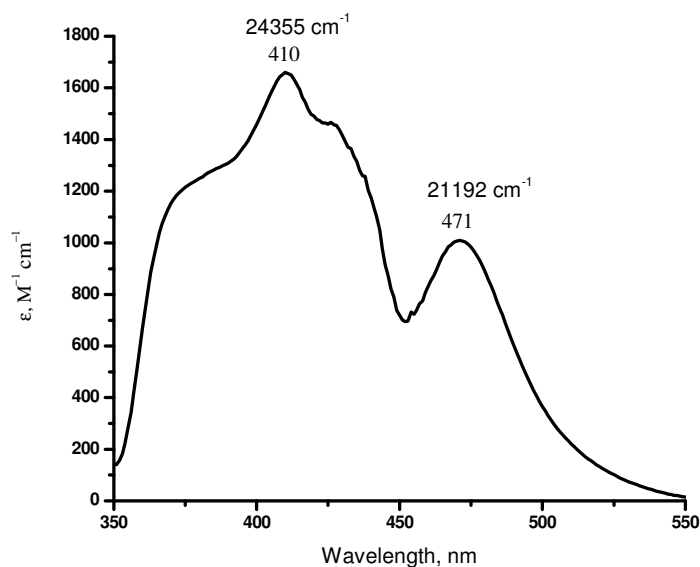


Figure 3.26 Difference spectrum for $[\text{Ru}(\text{bpy})_2(\eta^2\text{-tpyH}^+)]^{3+}$ relative to $[\text{Ru}(\text{bpy})_2(\eta^2\text{-tpy})]^{2+}$, as calculated from the data shown in the Figure 3.25.

The band centered at 21192 cm^{-1} ($\lambda_{\text{max}} = 471 \text{ nm}$) appears in concert with a new emission band at 550 nm (see below). The difference spectrum also shows a complex band envelope in the $22000\text{-}28000 \text{ cm}^{-1}$ region.

The emission spectra of $[\text{Ru}(\text{bpy})_2(\eta^2\text{-tpy})]^{2+}$ and its protonated form in acetonitrile are shown in Figure 3.27.

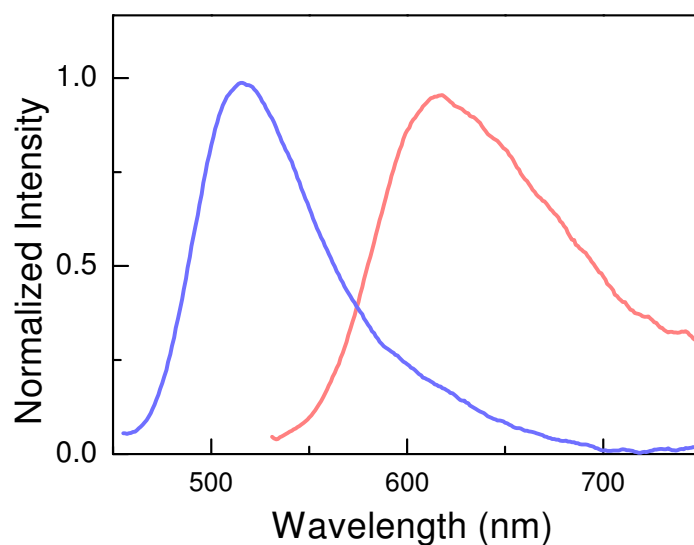


Figure 3.27 The emission spectra of $[\text{Ru}(\text{bpy})_2(\eta^2\text{-tpy})]^{2+}$ (red) and $[\text{Ru}(\text{bpy})_2(\eta^2\text{-tpyH}^+)]^{2+}$ (blue) in acetonitrile at 298 (± 3) K. Excitation energy, $\lambda_{\text{exc}} = 355$ nm.

The emission band appears at lower wavelength for the protonated $[\text{Ru}(\text{bpy})_2(\eta^2\text{-tpyH}^+)]^{2+}$ compared to $[\text{Ru}(\text{bpy})_2(\eta^2\text{-tpy})]^{2+}$. With λ_{exc} at 355 nm, the emission intensity of $[\text{Ru}(\text{bpy})_2(\eta^2\text{-tpyH}^+)]^{2+}$ shows a band at 520 nm with greater quantum efficiency ($\Phi_{\text{em}} = 2.0 \times 10^{-4}$) than that of $[\text{Ru}(\text{bpy})_2(\eta^2\text{-tpy})]^{2+}$ at 615 nm (Figure 3.27).

An emission lifetime spectrum of protonated $[\text{Ru}(\text{bpy})_2(\eta^2\text{-tpyH}^+)]^{2+}$ is shown in Figure 3.28. The excited state lifetime of $[\text{Ru}(\text{bpy})_2(\eta^2\text{-tpyH}^+)]^{2+}$ is 2.6 ns, greater than that of the parent complex, 0.082 ns. This is a remarkable observation as protonation enhances the lifetime which may open a new dimension of research. Increase in lifetime may lead to the exploration of new types of excited state reactions such as charge transfer, electron transfer, proton coupled electron transfer and other catalytic substitution reactions.

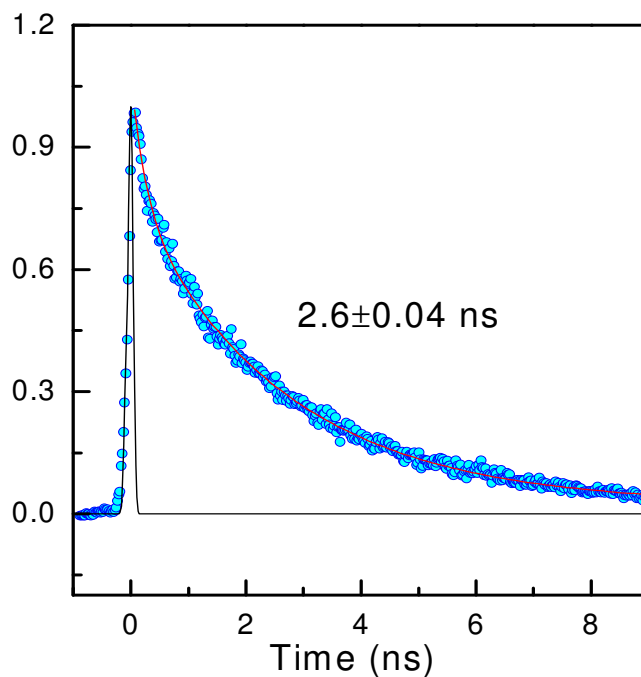


Figure 3.28 Emission life time spectrum of $[\text{Ru}(\text{bpy})_2(\eta^2\text{-tpyH}^+)]^{2+}$. The time-resolved emission of $[\text{Ru}(\text{bpy})_2(\eta^2\text{-tpyH}^+)]^{2+}$ with fitting (solid).

Transient absorption difference spectra were also obtained following laser flash excitation of $[\text{Ru}(\text{bpy})_2(\eta^2\text{-tpyH}^+)]^{2+}$ at 388 nm (5 mJ/pulse). Selected time traces from the transient absorption spectra are shown in Figure 3.29.

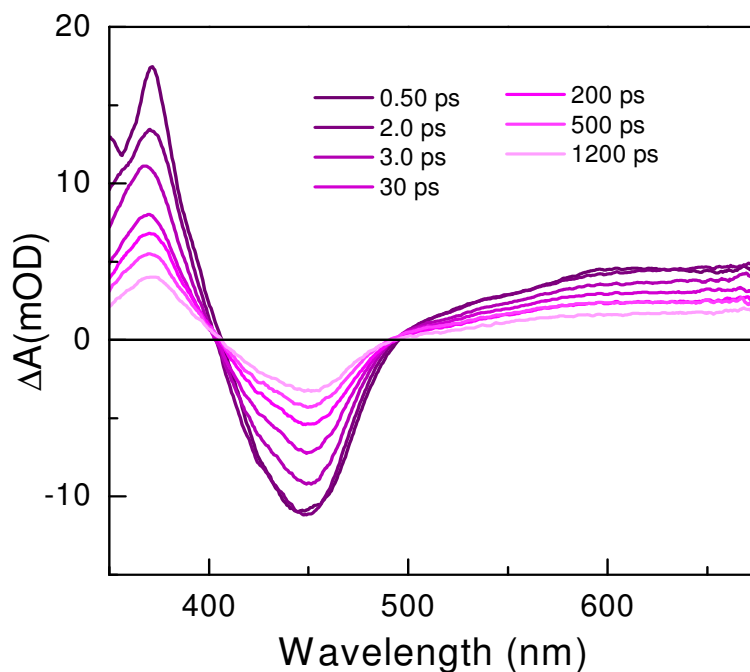


Figure 3.29 Femtosecond transient absorption of $[\text{Ru}(\text{bpy})_2(\eta^2\text{-tpy})]^{2+} + 5$ equivalents H^+ in acetonitrile.

Femtosecond transient absorption of $[\text{Ru}(\text{bpy})_2(\eta^2\text{-tpy})]^{2+}$ and its protonated form were taken in CH_3CN , Figure 3.30(A).³⁴ The kinetic traces at 450 nm of $[\text{Ru}(\text{bpy})_2(\eta^2\text{-tpy})]^{2+}$ and $[\text{Ru}(\text{bpy})_2(\eta^2\text{-tpyH}^+)]^{2+}$ are given in Figure 3.30(B).

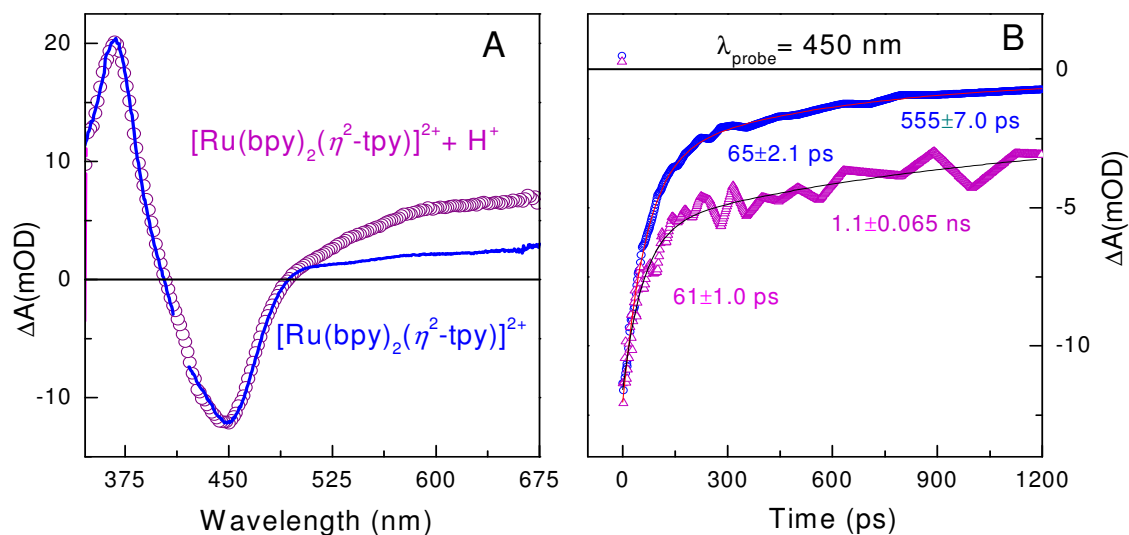


Figure 3.30 (A) Femtosecond transient absorption of $[\text{Ru}(\text{bpy})_2(\eta^2\text{-tpy})]^{2+}$ in acetonitrile (blue line) and femtosecond transient absorption of $[\text{Ru}(\text{bpy})_2(\eta^2\text{-tpy})]^{2+} + 5$ equivalents H^+ in acetonitrile (purple circle). (B) Kinetic traces at 450 nm of $[\text{Ru}(\text{bpy})_2(\eta^2\text{-tpy})]^{2+}$ (blue) and $[\text{Ru}(\text{bpy})_2(\eta^2\text{-tpy})]^{2+} + 5$ equivalents H^+ (purple).

Sub-ns transient absorption spectra of protonated $[\text{Ru}(\text{bpy})_2(\eta^2\text{-tpy})]^{2+}$ in acetonitrile are shown in, Figure 3.31(A), together with kinetics at 375 nm and 450 nm in Figure 3.31(B).

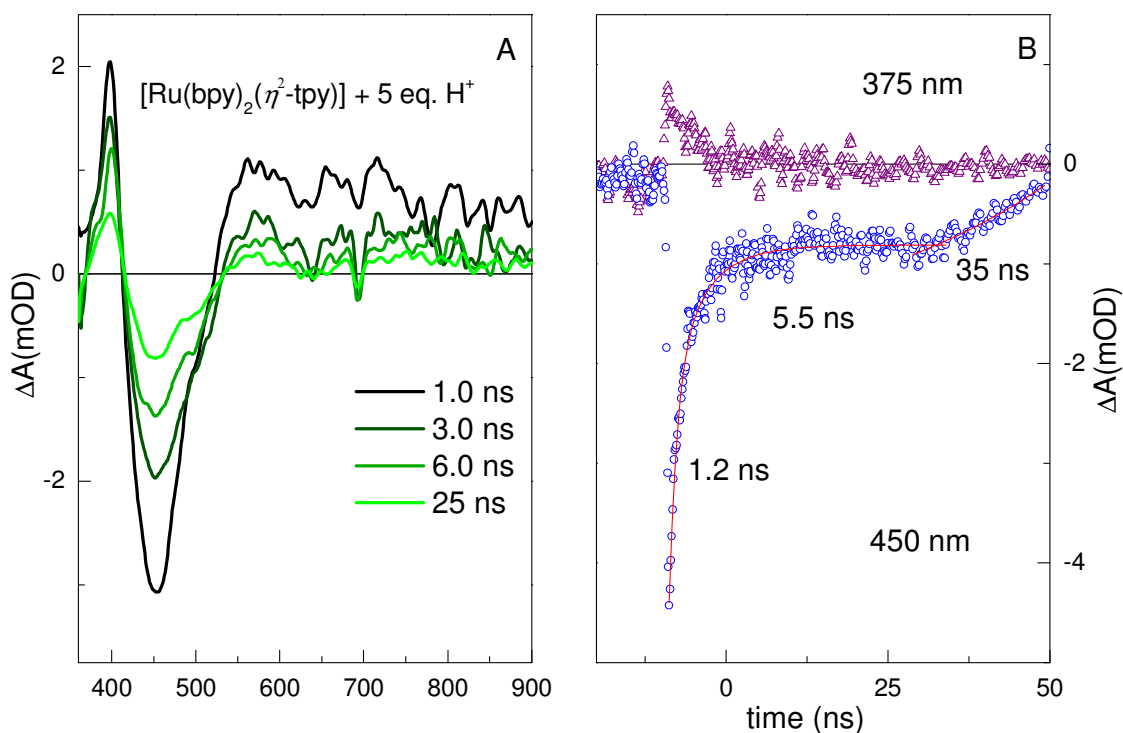


Figure 3.31 (A) Sub-ns transient absorption of $[\text{Ru}(\text{bpy})_2(\eta^2\text{-tpy})]^{2+} + 5$ equivalent H^+ in acetonitrile. (B) Kinetics at 375 nm and 450 nm.

Table 3.7 summarizes the emission data for the unprotonated and protonated complexes and the respective values of the radiative, k_r and nonradiative k_{nr} , rate constants derived from the following relationships:

$$\tau = 1/k_r + k_{nr} \quad (3.33)$$

$$\Phi_{em} = \eta_{isc} \frac{k_r}{k_{nr} + k_r + \sum_0^i \lambda_i} \quad (3.34)$$

Table 3.7 Photophysical parameters and radiative and nonradiative rate constants for $^3[\text{Ru}(\text{bpy})_2(\eta^2\text{-tpy})]^{2+*}$, $^3[\text{Ru}(\text{bpy})_2(\eta^2\text{-tpyH})]^{3+*}$ and $[\text{Ru}(\text{bpy})_3]^{2+*}$:

Parameters	$^3[\text{Ru}(\text{bpy})_2(\eta^2\text{-tpy})]^{2+*}$	$^3[\text{Ru}(\text{bpy})_2(\eta^2\text{-tpyH})]^{3+*}$	$[\text{Ru}(\text{bpy})_3]^{2+*}$
$\lambda_{\text{max}}^{\text{em}}, \text{nm}$	615	515	620
$E_{\text{em}}, \text{cm}^{-1} (\text{eV})$	16580 (2.06)	19310 (2.40)	16200 (2.0)
$\tau, \text{ns} (298\text{K})$	0.082	2.6	670
ϕ_{em}	7×10^{-5}	2×10^{-4}	0.062
$E_{\text{ss}}, \text{cm}^{-1}$	5640	1980	1700
k_r, s^{-1}	8×10^8	9.52×10^{-4}	5.9×10^5
$k_{\text{nr}}, \text{s}^{-1}$	1×10^{10}	5×10^8	1.0×10^6

3.7 Discussion

3.7.1 Spectroscopic Analysis

Absorption spectra of $[Ru(bpy)(\eta^2\text{-tpy})]^{2+}$ and the protonated complex in CH_3CN are shown in Figure 3.25. Evidence for a new transition in the difference spectrum is given in Figure 3.26. The band centered at 21192 cm^{-1} ($\lambda_{\text{max}} = 470\text{ nm}$) appears in concert with a new emission band at 550 nm and is presumably due to polarization of the electronic wave function (ψ_{π^*}) on to the pyridyl ring adjacent to the PyH^+ substituent. It follows that removal of electron density in the σ -bonded framework would lower the π and π^* energies of the pyridyl ring as it would experience an increased positive electrostatic attraction from the carbon atoms that make up the pyridyl ring. As such the π^* levels would be stabilized.⁴⁰

A Franck-Condon analysis⁴² of the intra ligand charge transfer (ILCT) transition is revealing. The bandwidth is related to CT energy (E_{IT}) and the free energy differences between the electron donor and electron acceptor by

$$(\Delta\nu_{1/2})^2 = 16(E_{IT} - \Delta G^o)k_B T \ln 2 \quad (3.37)$$

with $\Delta\nu_{1/2}$ of 1900 cm^{-1} , $E_{IT} = 21192\text{ cm}^{-1}$, $\Delta G^o = 19620\text{ cm}^{-1}$ ($\Delta E = 2.43\text{ eV}$) and $T = 298\text{ K}$.⁴² The $Ru^{III/II}$ based reduction potential is -1.30 V vs SCE and the oxidation potential of the pyH^+ acceptor is calculated to be -1.16 V vs SCE and is comparable to -0.9 V for the MQ^{+} Couple, Table 3.5.

The oscillator strength (f_{osc}) of the $Ru^{II} \rightarrow pyH^+$ transition is related⁴² to the transition dipole moment by

$$f_{osc} = \int \varepsilon(\bar{\nu}) d\bar{\nu} = \frac{8\pi m_e \bar{\nu}_{\max}}{3he^2} |\bar{\mu}_{12}|^2 \quad (3.38)$$

where $\int \varepsilon(\bar{\nu}) d\bar{\nu}$ is the integrated band intensity; m_e is mass of the electron, $\bar{\nu}_{\max}$ is the energy of the band maximum, h is Plank's constant, e is the charge of the electron and $\bar{\mu}_{12}$ is the transition dipole moment. The magnitude of the f_{osc} of a Gaussian charge transfer band can be determined experimentally by⁴²

$$f_{osc} = 4.61 \times 10^{-9} (\varepsilon_{\max} \Delta\nu_{1/2}) \quad (3.39)$$

where ε_{\max} is the extinction coefficient at $\bar{\nu}_{\max}$ and $\Delta\nu_{1/2}$ is bandwidth which has been defined above. Using $\varepsilon_{\max} = 1000 \text{ M}^{-1}\text{cm}^{-1}$ and $\Delta\nu_{1/2} = 1900 \text{ cm}^{-1}$, the magnitude of the calculated oscillator strength (f_{osc}) for $[\text{Ru}(\text{bpy})_2(\eta^2\text{-tpy})]^{2+}$ CT band is 0.0876, close to the value of calculated oscillator strength (f_{osc}) of $[\text{Ru}(\text{bpy})_3]^{2+}$, Table 3.8.

Table 3.8 Spectroscopic parameters derived from a Mulliken-Hush analysis of the spectral band envelopes for the $\text{Ru} \rightarrow \text{pyH}^+$ and MLCT transition

Parameter	$[(d\pi)^6] \rightarrow {}^1[(d\pi)^5(\pi^*_{\text{pyH}})]$	$[(d\pi)^6] \rightarrow {}^1[(d\pi)^5(\pi_1^*)]$
$\lambda_{\text{max}}^{\text{abs}}, \text{nm}(\text{cm}^{-1})$	471 (21192)	451 (22173)
$\varepsilon, M^{-1}\text{cm}^{-1}$	1000	14.4×10^3
$\Delta v_{1/2}, \text{cm}^{-1}$	1900	752
f_{osc}	0.0876	0.0498
$\bar{\mu}_{12}, e \text{ \AA}$	0.2	0.11
$H_{\text{DA}}, \text{cm}^{-1}(d, \text{ \AA})$	2300 (3.0)	2705(1.6)
α	0.11	0.12
$\varepsilon_s, \text{cm}^{-1}$	200	340

The magnitude of $\bar{\mu}_{12}$ for the $[\text{Ru}(\text{bpy})_2(\eta^2\text{-tpy})]^{2+}$ CT transition is given by rearrangement of eqn. 3.38 as

$$|\bar{\mu}_{12}|^2 = \frac{f_{\text{osc}}}{(1.08 \times 10^{-5}) \bar{\nu}_{\text{max}}} \quad (3.40)$$

where the constants given in equation 3.38 are 1.08×10^{-5} , $\bar{\nu}_{\text{max}}$ is 21192 cm^{-1} , and $\bar{\mu}_{12}$ is $0.2 e\text{ \AA}$, consistent with the proposed $\text{Ru}^{\text{II}} \rightarrow \text{pyH}^+$ photoinduced charge transfer transition and close to the value of the calculated transition dipole moment ($\bar{\mu}_{12}$) of $[\text{Ru}(\text{bpy})_3]^{2+}$ ($0.1 e\text{ \AA}$).⁴³

The extent of orbital mixing between the $d\pi$ and π^* orbitals is given by the electronic coupling element H_{DA} . The Mulliken-Hush expression⁴⁴ for determining the electronic coupling matrix element H_{AD} is given by

$$H_{DA} = \left(\frac{0.0205}{d}\right) [\varepsilon_{\max} \Delta \bar{\nu}_{1/2} \cdot \bar{\nu}_{\max}]^{1/2} \quad (3.41)$$

where d is the charge transfer distance between the donor and the acceptor. ε_{\max} is the extinction coefficient in $\text{M}^{-1}\text{cm}^{-1}$, $\Delta \bar{\nu}_{1/2}$ is the full width at half-height in cm^{-1} and $\bar{\nu}_{\max}$ is the energy of the peak maximum in cm^{-1} . Here, d is the charge transfer distance between bpy and the pendant pyridine of $[\text{Ru}(\text{bpy})_2(\eta^2\text{-tpyH}^+)]^{3+}$ and is estimated to be $\sim 3.0 \text{ \AA}$ and the electronic coupling matrix element H_{DA} is 2300 cm^{-1} . Similar types of strong coupling were observed in $[\text{Ru}(\text{bpy})_3]^{2+}$ and the calculated electronic coupling matrix element H_{DA} is 2705 cm^{-1} for $[\text{Ru}(\text{bpy})_3]^{2+}$.⁴⁴

Strong electronic coupling between a donor and acceptor can result in configurational mixing and thus modifies the properties of both donor and acceptor perturbationally.³⁸ According to this perturbation theory analysis, the ground state is stabilized by an amount ε_s and can be calculated from the following relation⁴⁴

$$\begin{aligned} \varepsilon_s &= [(H_{DA})^2 / (1 - \alpha^2)] / E_{DA} & (3.42) \\ &= 200 \text{ cm}^{-1} \end{aligned}$$

where $H_{DA} = \langle \psi_{e.s} | H | \psi_{g.s} \rangle$ is the electronic coupling matrix element, $\psi_{e.s}$ and $\psi_{g.s}$ are the unmixed wavefunction of the excited state and ground state; H is a Hamiltonian operator. The Frank-Condon excited state is destabilized by an equal amount as shown in Figure 3.32.

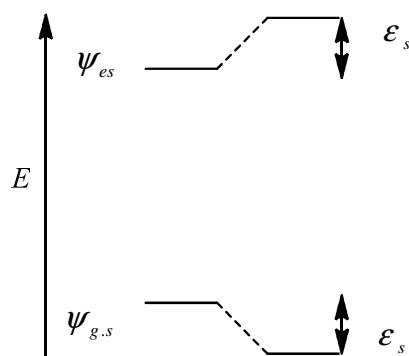


Figure 3.32 The effect of configuration interactions for the pendant pyridine.

In a strongly coupled donor-acceptor system, $\alpha = H_{DA} / E_{DA}$ where α is the mixing parameter that describes the extent of mixing of electronic wave functions. E_{DA} is the energy difference between the ground and excited states. The values for the oscillator strength (f_{osc}), the transition dipole moment ($\bar{\mu}_{12}$); the electronic coupling element (H_{DA}) and the mixing parameter α for $[\text{Ru}(\text{bpy})_2(\eta^2\text{-tpyH}^+)]^{3+}$ CT and $[\text{Ru}(\text{bpy})_3]^{2+}$, calculated with the eqn. 3.37-3.42, are given in Table 3.8.

The absence of photochemistry for $[\text{Ru}(\text{bpy})_2(\eta^2\text{-tpy})]^{2+}$ is counter intuitive given the steric bulk of the pendant pyridine which gives rise to longer Ru-N bond lengths relative to $[\text{Ru}(\text{bpy})_3]^{2+}$. Since the cofacial orientation of the pendant pyridine of the tpy ligand with the adjacent bpy in $[\text{Ru}(\text{bpy})_2(\eta^2\text{-tpy})]^{2+}$ may facilitate π -stacking with the adjacent bpy similar to that of $[\text{Ru}(\text{bpy})_2(\text{phen-R})]^{2+}$ complexes, this may contribute to the barrier for ligand loss.⁴⁰ The temperature-dependent luminescence data for $[\text{Ru}(\text{bpy})_2(\text{phen})]^{2+}$ demonstrates the weakened ligand field that permits the crossover

from the $^3\text{MLCT}$ to ^3LF state. The efficiency of populating the ^3LF state $\eta_{\text{LF}} = 1.0$ for $[\text{Ru}(\text{bpy})_2(\text{phen})]^{2+}$, was estimated using eqn. 3.43.⁴⁰

$$\eta_{\text{LF}} = [k' \exp(-E_a / RT)] / k_o + k' \exp(-E_a / RT) \quad (3.43)$$

where $E_a = 1660 \text{ cm}^{-1}$ $k' = 7 \times 10^{11} \text{ s}^{-1}$; $k_o = \tau^{-1} = k_r + k_{nr}$

The ligand field state is known to be more labile than the MLCT state. However, photochemical and photophysical data reveal that the LF state of $[\text{Ru}(\text{bpy})_2(2\text{-phenylphen})]^{2+}$ is stabilized which may be attributed to the $\pi\text{-}\pi$ interactions between 2-phenylphen and adjacent bpy.⁴⁶

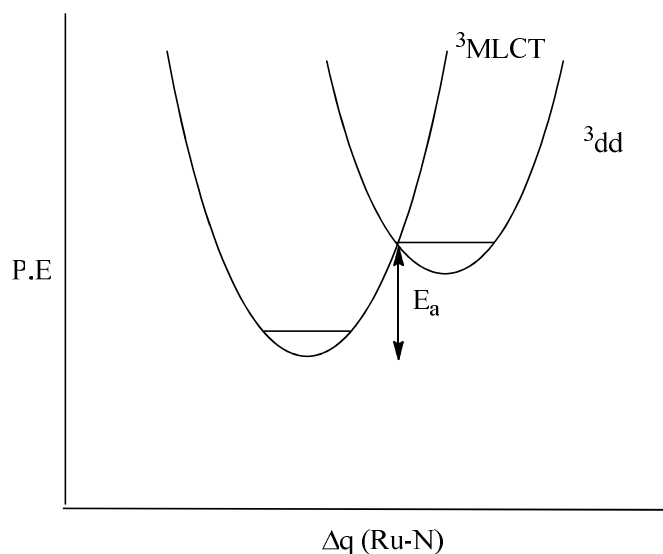


Figure 3.33 Potential energy surface diagram illustrating the $^3\text{MLCT}$ state.

Electrostatic models have been developed to explain the octahedral ligand splitting as a function of the five metal-ligand distances.⁴⁶ Accordingly, $10 Dq$ for $[\text{Ru}(\text{bpy})_2(\eta^2\text{-tpy})]^{2+}$ have been calculated using the following eqn:

$$\frac{10 \text{ Dq } [\text{Ru}(\text{bpy})_2(\eta^2\text{-tpy})]^{2+}}{10 \text{ Dq } [\text{Ru}(\text{bpy})_3]^{2+}} = \left(\frac{\text{Ru-N } [\text{Ru}(\text{bpy})_3]^{2+}}{\text{Ru-N } [\text{Ru}(\text{bpy})_2(\eta^2\text{-tpy})]^{2+}} \right)^5 \quad (3.44)$$

$$\frac{10 \text{ Dq } [\text{Ru}(\text{bpy})_2(\eta^2\text{-tpy})]^{2+}}{3.89 \text{ eV}} = \left(\frac{2.056 \text{ \AA}}{2.083 \text{ \AA}} \right)^5$$

$$10 \text{ Dq } [\text{Ru}(\text{bpy})_2(\eta^2\text{-tpy})]^{2+} = 3.64 \text{ eV}$$

This indicates that the dd states are more accessible and result in rapid non-radiative decay in $[\text{Ru}(\text{bpy})_2(\eta^2\text{-tpy})]^{2+}$ through a ${}^3\text{MLCT-}dd$ state transition followed by rapid decay of the metal centred excited state.⁴⁶ The 10 Dq values for $[\text{Ru}(\text{bpy})_2(\text{bpy-cyclam})]^{2+}$ and $[\text{Ru}(\text{bpy})_2(2\text{-phenylphen})]^{2+}$ are 3.70 eV and 3.71 eV, respectively. The potential energy diagram for $[\text{Ru}(\text{bpy})_3]^{2+}$ and $[\text{Ru}(\text{bpy})_2(\eta^2\text{-tpy})]^{2+}$ is shown in Figure 3.34.

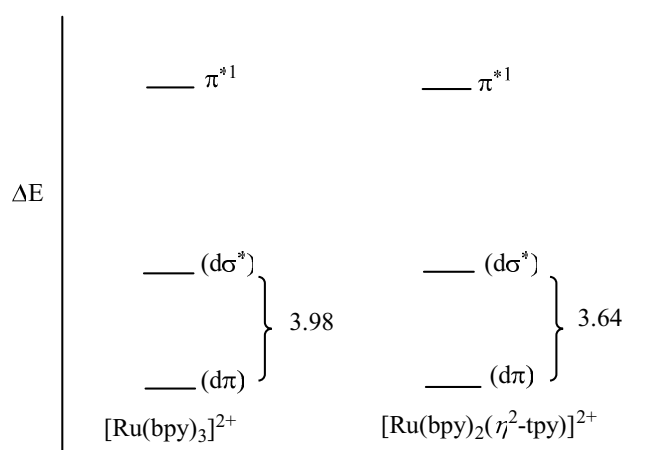


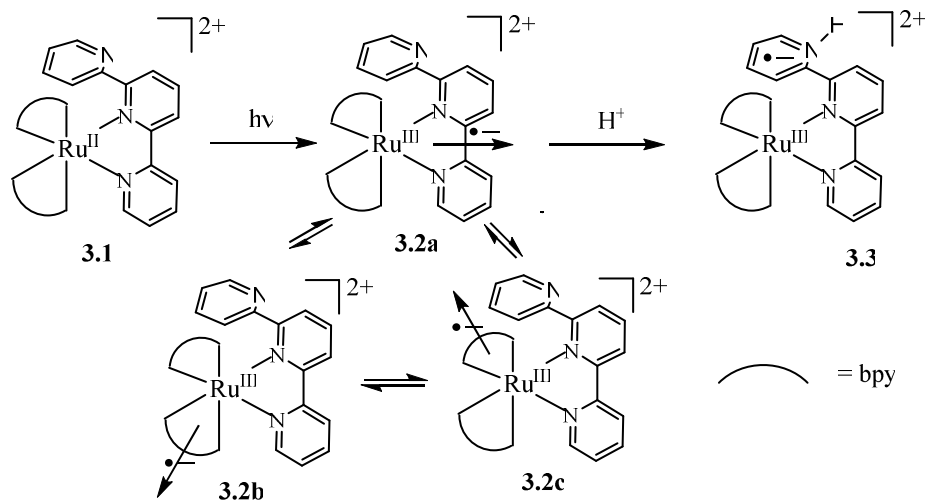
Figure 3.34 Potential energy diagram for $[\text{Ru}(\text{bpy})_3]^{2+}$ and $[\text{Ru}(\text{bpy})_2(\eta^2\text{-tpy})]^{2+}$.

The variation in the life-time and intensity of quenching of $[\text{Ru}(\text{bpy})_2(\eta^2\text{-tpy})]^{2+}$ by H^+ clearly indicates the dynamic behaviour of the reaction. The increase in life-time when the pendant pyridine is protonated is an important observation which to the best of our knowledge is unprecedented in transition metal systems. Conformational changes play an important role and have a significant effect on the life-time and intensities of bipyridine-based metal to ligand charge transfer (MLCT) transitions. In $[\text{Ru}(\text{bpy})_2(\eta^2\text{-tpy})]^{2+}$, the pendant pyridine ring of the terpyridine ligand has access to π - π interactions with the adjacent bpy ligand which might stabilize the ligand field states.

3.7.2 Transient Absorption Spectral Analysis

Transient absorption difference spectra were obtained following laser flash excitation of protonated $[\text{Ru}(\text{bpy})_2(\eta^2\text{-tpy})]^{2+}$. Selected time traces from the transient absorption spectra have been shown in Figure 3.29. The initial traces (pink) feature a bleach near 450 nm corresponding to the depletion of the ground state MLCT absorption, concomitant with a broad absorption at longer wavelengths which is attributed to the ligand-to-metal charge transfer (LMCT) transition from the neutral bpy to the Ru^{3+} center and a $\pi \rightarrow \pi^*$ transition arising from the reduced bpy. These features are characteristic of a thermally relaxed $^3\text{MLCT}$ excited state.³⁷ This state is achieved within approximately 1 ps. Subsequent traces show decay in these features as well as a positive absorbance growing in at 500 nm. In the last time trace (black), the broad long wavelength absorbance has not decayed back to zero. The high energy emission and increase in lifetime for the protonated $[\text{Ru}(\text{bpy})_2(\eta^2\text{-tpy})]^{2+}$ can be attributed to the formation of a

ligand-based radical of the $[\text{Ru}(\text{bpy})_2(\eta^2\text{-tpy})]^{2+}$ complex. Scheme 3.20 illustrates the proposed mechanism for the formation of that ligand-based radical species.



Scheme 3.20 Proposed mechanism for the protonated excited state of $[\text{Ru}(\text{bpy})_2(\eta^2\text{-tpy})]^{2+}$.

After photo excitation of **3.1** at 355 nm (Scheme 3.20), there is an increase in the electron density on the ligands due to the MLCT transition. Scheme 3.20 illustrates the two bpy ligands and one tpy ligand in $[\text{Ru}(\text{bpy})_2(\eta^2\text{-tpy})]^{2+}$ with the excited electron in the lowest triplet MLCT state $^3(d\pi^5 \pi^{*1})$ $^3\text{MLCT}$ in π^*_{1} of the tpy ligand. The corresponding hole is $d\pi^5$ aligned along the π^* acceptor in the dipole state which maximizes electrostatic interactions with the excited electron. As the electron resides mainly on the tpy ligand (Scheme 3.20, **3.2a**), the other two additional MLCT excited states of bpy are off set to higher energy. Protonation of the pendant pyridine of the tpy ligand drives the electron towards this ring and the electron becomes localized on the protonated pyridine, **3.3**, as shown in Scheme 3.20. The transient absorption spectrum of the protonated complex

(Figure 3.30) shows a prompt growth at 600 nm which has been assigned to the formation of a $[\text{Ru}(\text{bpy})_2(\eta^2\text{-tpyH})^{\bullet-}]^{2+}$ ligand-based radical. The high energy emission from the protonated complex at 520 nm might be due to the formation of this ligand-based radical.

Resonance stabilization energy can be approximated by the degree of overlap of the $2p_z$ orbitals of the six carbon atoms of pyH^+ with the $2p_z^1$ orbitals of the adjacent ring *i.e.* the magnitude of the overlap integral between two rings.⁴⁷ The overlap integral for hydrogenic $2p_z$ orbitals is given by⁴⁷

$$\langle 2p_z | 2p_z \rangle = K^2(2a/Z - L)[\exp(-ZL/2a)]\cos\theta \quad (3.45)$$

where K is a constant, Z is the effective nuclear charge, a is the Bohr radius, L is the distance between two nuclei and θ is the dihedral angle. The term $\cos\theta$ is the origin of the dihedral angle dependence of π electronic coupling. If the two rings are coplanar $\theta = 0^\circ$, and $\cos\theta = 1$ and the overlap is maximum.

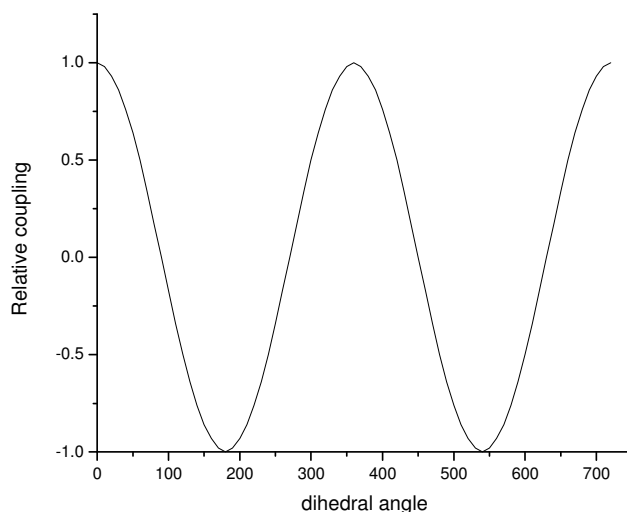


Figure 3.35 Relation between the dihedral angle and the relative coupling.

On the other hand, when the rings are perpendicular, $\theta = 90^\circ$ and $\cos\theta = 0$, where there is no π electron delocalization. Figure 3.35 illustrates the relationship between the dihedral angle and the relative coupling.

There exists a strong body of resonance Raman data on $[\text{Ru}(\text{mmb})_3]$ and $[\text{Ru}(\text{py-pyz})_3]^{2+}$ where the excited state spin density is localized on the ring system bearing a Me group for $[\text{Ru}(\text{mmb})_3]$ and pyz fragment in $[\text{Ru}(\text{py-pyz})_3]^{2+}$ (Figure 3.36).⁴⁸

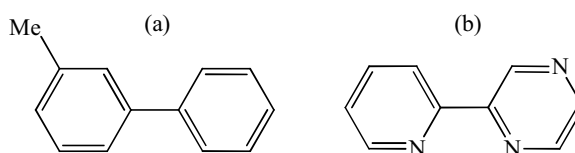


Figure 3.36 Structure of a) 4-methyl bipyridine and b) 2-(2-pyridyl)pyrazine.

In the case of the $[\text{Ru}(\text{bpy})_2(\eta^2\text{-tpy})]^{2+}$ complex, the pendant pyridine of the tpy ligand rotates, and the coupling between the pendant pyridine and the adjacent bpy ligand depends on the dihedral angle and changes as shown in the Figure 3.35. However, protonation of the pendant pyridine restricts the rotation and thus stabilizes the complex. Thus, the lifetime for the protonated species increases over that of the complex itself. Also, the polarization of the electron density towards the protonated pyridine will result in lower π and π^* levels of the pyridine because the π and π^* levels will experience a greater electrostatic interaction with the nuclei of the pyridyl atoms and thus the MOs will be stabilized.⁴⁰

3.8 Conclusion

The ground and excited state dynamics of $[\text{Ru}(\text{bpy})_2(\eta^2\text{-tpy})]^{2+}$ have been discussed. In the ground state, electronic coupling between the pendant pyridine and adjacent bpy in $[\text{Ru}(\text{bpy})_2(\eta^2\text{-tpy})]^{2+}$ is very weak, which is evident from the overlaid absorption spectra of $[\text{Ru}(\text{bpy})_2(\eta^2\text{-tpy})]^{2+}$ and $[\text{Ru}(\text{bpy})_3]^{2+}$. However, addition of trifluoroacetic acid (TFA) results in slight spectral changes which have been assigned to protonation of the pendant pyridine of $[\text{Ru}(\text{bpy})_2(\eta^2\text{-tpy})]^{2+}$. A new transition band has been identified, assigned to a $^3\text{MLCT}$ interligand charge transfer transition, based on the differences between the spectra of $[\text{Ru}(\text{bpy})_2(\eta^2\text{-tpyH}^+)]^{3+}$ and $[\text{Ru}(\text{bpy})_2(\eta^2\text{-tpy})]^{2+}$.

The excited state lifetime of $[\text{Ru}(\text{bpy})_2(\eta^2\text{-tpy})]^{2+}$ is 82 ps. However, there is a remarkable increase in lifetime of the protonated $[\text{Ru}(\text{bpy})_2(\eta^2\text{-tpy})]^{2+}$ complex. With $\lambda_{\text{exc}} = 355$ nm, the emission intensity of the protonated $[\text{Ru}(\text{bpy})_2(\eta^2\text{-tpy})]^{2+}$ is at 520 nm with quantum efficiency $\Phi_{\text{em}} = 2.0 \times 10^{-4}$ and increased lifetime of 2.6 ns. The high energy emission and increase in lifetime for the protonated $[\text{Ru}(\text{bpy})_2(\eta^2\text{-tpy})]^{2+}$ can be attributed to the formation of a ligand-based radical of $[\text{Ru}(\text{bpy})_2(\eta^2\text{-tpyH}^+)]^{2+}$ complex.

Mulliken-Hush analysis of the ILCT of $[\text{Ru}(\text{bpy})_2(\eta^2\text{-tpy})]^{2+}$ has been done and compared with that of $[\text{Ru}(\text{bpy})_3]^{2+}$. The value for the electronic coupling element (H_{DA}) for $[\text{Ru}(\text{bpy})_2(\eta^2\text{-tpyH}^+)]^{3+}$ suggests that the electronic coupling between bpy and the pendant pyridine is quite strong. In $[\text{Ru}(\text{bpy})_2(\eta^2\text{-tpy})]^{2+}$, the pendant pyridine of the tpy ligand rotates and the coupling between the pendant pyridine and adjacent bpy ligand

depends on the dihedral angle. However, protonation of the pendant pyridine restricts the rotation and thus stabilizes the complex.

3.9 References

1. Juris A.; Balzani, V. *Coor. Chem. Rev.* **1988**, *84*, 85.
2. Alstrum-Acevedo, J. H.; Brennaman, M. K.; Meyer, T. J. *Inorg. Chem.* **2005**, *44*, 6802. b) Balzani, V.; Juris, A.; Venturi, M. *Chem. Rev.* **1996**, *96*, 759. c) Gaillard, E. R.; Whitten, D. G. *Acc. Chem. Res.* **1996**, *29*, 292.
3. a) Meyer, T. J. *Pure Appl. Chem.* **1986**, *58*, 1193. b) Bock, C. R.; Meyer, T. J.; Whitten, D. G. *J. Am. Chem. Soc.* **1974**, *96*, 4710. (c) Demas, J. N.; Adamson, A. W. *J. Am. Chem. Soc.* **1973**, *95*, 5159. (d) Adamson, A. W.; Demas, J. N. *J. Am. Chem. Soc.* **1971**, *93*, 1800. e) Sun, H.; Yoshimura, A.; Hoffman. M. Z. *J. Phys. Chem.* **1994**, *98*, 5058.
4. (a) Turró, C; Zaleski, J. M.; Karabatsos, Y. M.; Nocera, D. J. *J. Am. Chem. Soc.* **1996**, *118*, 6060. b) Gould, I. R.; Farid, S. *Acc. Chem. Res.* **1996**, *29*, 522.
5. (a) Dougherty, E. V. A.; Dennis. A. *Modern Physical Organic Chemistry*; University Science Books, **2006**. (b) Meyer, G. J. *Molecular Level Artificial Photosynthetic Materials (Progress in Inorganic Chemistry)*, John Wiley & Sons, Inc. *44*, **1997**
6. Deronzier, A.; Meyer, T. J. *Inorg. Chem.* **1980**, *19*, 2912.
7. Wang, L.; Puodziukynaite, E.; Vary, R. P.; Grumstrup, E. M.; Walczak, R. M.; Zolotarskaya, O. Y.; Schanze, K. S.; Reynolds, J. R.; Papanikolas, J. M. *J. Phys. Chem. Lett.* **2012**, *17*, 2453.

8. Lee, E. J.; Wrighton, M. S. *J. Am. Chem. Soc.* **1991**, *113*, 8562.
9. Sullivan, B. P.; Abruna, H.; Finklia, H. O.; Salmon, D. J.; Nagle, J. K.; Meyer, T. J.; Sprintschnik, H. *Chem. Phys. Lett.* **1978**, *58*, 389.
10. a) Treadway, J. A.; Rutherford, T. J.; Chen, P.-Y.; Keene, F. R.; Meyer, T. J. *J. Phys. Chem. A* **1997**, *101*, 6824. b) Danielson, E.; Elliott, C. M.; Merkert, J. W.; Meyer, T. *J. Am. Chem. Soc.* **1987**, *109*, 2519.
11. Collin, J.-P.; Guillerez, S.; Sauvage, J.-P.; Barigelletti, F.; De Cola, L.; Flamigni, L.; Balzani, V. *Inorg. Chem.* **1991**, *30*, 4230.
12. (a) Collin, J.-P.; Guillerez, S.; Sauvage, J.-P.; Barigelletti, F.; De Cola, L.; Flamigni, L.; Balzani, V. *Inorg. Chem.* **1992**, *31*, 4112. (b) Coe, B. J.; Friesen, D. A.; Thompson, D. W.; Meyer, T. J. *Inorg. Chem.* **1996**, *35*, 4575.
13. Sauvage, J. -P.; Collin, J. -P.; Chambron, J. -C.; Guillerez, S.; Coudret, C.; Balzani, V.; Barigelletti, F.; Cola, L. De.; Flamigni, L. *Chem. Rev.* **1994**, *94*, 993.
14. Creutz, C.; Sutin, N. *J. Am. Chem. Soc.* **1988**, *110*, 2418.
15. Giordano, P. J.; Bock, C. R.; Wrighton, M. S.; Interrante, L. V.; Williams, R. F. X. *J. Am. Chem. Soc.* **1977**, *99*, 3187.
16. Lay, P. A.; Sasse, W. H. F. *Inorg. Chem.* **1984**, *23*, 4123.
17. Zambrana, J. L.; Ferloni, J. E. X.; Gafney, H. D. *J. Phys. Chem. A* **2009**, *113*, 13457.
18. Sun, H.; Hoffman, M. Z. *J. Phys. Chem.* **1993**, *97*, 5014.
19. Slattery, S. J.; Blaho, J. K.; Lehn, J.; Goldsby, K. A. *Coord. Chem. Rev.* **1998**, *174*, 391.
20. Chen, P.; Danielson, E.; Meyer, T. J. *J. Phys. Chem.* **1988**, *92*, 3708.

21. Tolbert, L. M.; Solntsev, K. M. *Acc. Chem. Res.* **2002**, *35*, 19.
22. Huynh, M. H. V.; Meyer, T. J. *Chem. Rev.* **2007**, *107*, 5004.
23. Irebo, T.; Reece, S. Y.; Sjödin, M.; Nocera, D. G.; Hammarström, L. *J. Am. Chem. Soc.* **2007**, *129*, 15462.
24. Mayer, J. M.; Hrovat, D. A.; Thomas, J. L.; Borden, W. T. *J. Am. Chem. Soc.* **2002**, *124*, 11142.
25. Costentin, C.; Evans, D. H.; Robert, M.; Savéant, J. M.; Singh, P. S. *J. Am. Chem. Soc.* **2005**, *127*, 12490.
26. Biczok, L.; Gupta, N.; Linschitz, H. *J. Am. Chem. Soc.* **1997**, *119*, 12601.
27. Swarnalathaa, K.; Rajkumarb, E.; Rajagopalb, S.; Ramarajb, R.; Banuc, I. S.; Ramamurthy, P. *J. Phy. Org. Chem.* **2011**, *24*, 14.
28. Miedlar, K.; Das, P. K. *J. Am. Chem. Soc.* **1982**, *104*, 7462.
29. Hammens-Sciffer S. *Acc. Chem. Res.* **2001**, *34*, 273.
30. Concepcion, J. J.; Brennaman, M. K.; Deyton, J. R.; Lebedeva, N. V.; Forbes, M. D. E.; Papanikolas, J. M.; Meyer, T. J. *J. Am. Chem. Soc.* **2007**, *129*, 6968.
31. Lebedeva, N. V.; Schmidt, R. D.; Concepcion, J. J.; Brennaman, M. K.; Stanton, I. N.; Therien, M. J.; Meyer, T. J.; Forbes, M. D. E. *J. Phys. Chem. A.* **2011**, *115*, 3346.
32. Bailey, S. I.; Ritchie, I. M.; Hewgill, F. R. *J. Chem. Soc., Perkin. Trans. 2.* **1983**, 645.
33. Ponce, A.; Gray, H. B.; Winkler, J. R. *J. Am. Chem. Soc.* **2000**, *122*, 8187.
34. Houten, J. V.; Watts, R. J. *J. Am. Chem. Soc.* **1975**, *97*, 3843.
35. McClanahan, S. F.; Kincaid, J. R. *J. Am. Chem. Soc.* **1986**, *108*, 3840.
36. Fujita, E.; Milder, S. J.; Brunshwig, B. S. *Inorg. Chem.* **1992**, *31*, 2079.

37. (a) Thompson, D. W.; Ito, A.; Meyer, T. J. *Pure Appl. Chem.* **2013** *in press.* (b) Cannizzo, A.; Mourik, F. V.; Gawelda, W.; Zgrablic, G.; Bressler, C.; Chergui, M. *Angew. Chem. Int. Ed.* **2006**, *45*, 3174.
38. Anderson, P. A.; Strouse, G. F.; Treadway, J. A.; Keene, F. R.; Meyer, T. J. *Inorg. Chem.* **1994**, *33*, 3863.
39. Schoonover, J. R.; Strouse, G. F. *Chem. Rev.*, **1998**, *98*, 1335.
40. Wu, F.; Riesgo, E.; Pavalova, A.; Kipp, R. A.; Schmehl, R. H.; Thummel, R. P. *Inorg. Chem.* **1999**, *38*, 5620.
41. Kober, E. M.; Caspar, J. V.; Lumpkin, R. S.; Meyer, T. J. *J. Phys. Chem.* **1986**, *90*, 3722.
42. Chen, P.; Meyer, T. J. *Chem. Rev.*, **1998**, *98*, 1439.
43. Yang, M.; Thompson, D. W.; Meyer, G. J. *Inorg. Chem.* **2002**, *41*, 1254.
44. Pablo, A.; Rossi, M. B.; Baraldo, L. M.; Slep, L. D. *Inorg. Chem.* **2006**, *45*, 10595.
45. Seneviratne, D. S.; Uddin, M. J.; Swayambunathan, V.; Schlegel, H. B.; Endicott, J. *F. Inorg. Chem.* **2002**, *41*, 1502.
46. Gawelda, W.; Johnson, M.; Groot, F. M. F.; Abela, R.; Bressler, C.; Chergui, M. *J. Am. Chem. Soc.* **2006**, *128*, 5001.
47. Chen, P.; Curry, M.; Meyer, T. J. *Inorg. Chem.* **1989**, *28*, 2271.
48. Treffert-Ziemelis, S. M.; Golus, J.; Strommen, D. P.; Kincaid, J. R. *Inorg. Chem.* **1993**, *32*, 3890.

Chapter 4 Time Resolved Ligand Loss from *cis*-[Ru(bpy)₂(py)₂]²⁺

4.1 Introduction

Ruthenium polypyridyl complexes are recognized for their unique combination of chemical stability, redox properties, reactivity, and their extensively documented excited state dynamics.¹ These complexes have metal-to-ligand charge transfer (MLCT) excited states which can be frequently used in a variety of applications. Several attempts have been made to understand the structures and reactivity of the excited states which includes temperature-dependent lifetime, resonance Raman, emission spectral fitting and most recently laser flash photolysis experiments.²

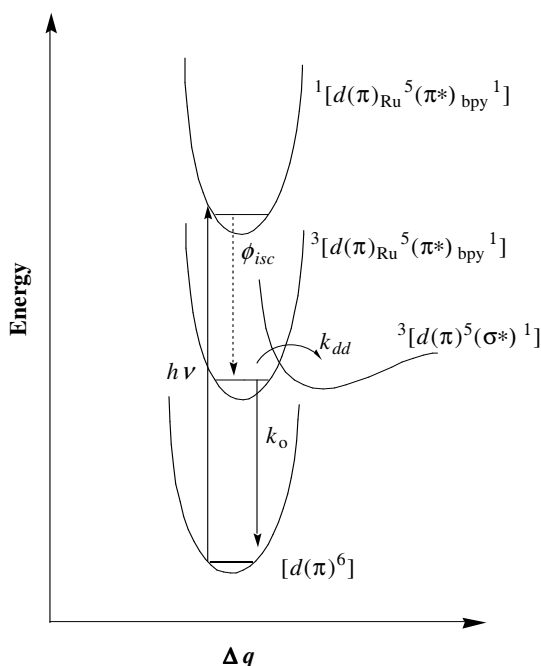


Figure 4.1: Potential Energy Diagram for $(d\pi)^6$ MLCT excited states.²

At low temperature, excitation of the MLCT band of a chromophore leads to the population of low-lying states where the deactivation process is dominated by radiative (k_r) or nonradiative (k_{nr}) decay. However, at higher temperature, dd states are populated and influence the photophysical and photochemical properties of the complexes.³ The energies of dd states vary as a function of ligand field strength and the electronic energy level pattern is distorted with respect to ground state. These states are formed by a thermally activated electron transfer and the excited electron moves from a $\pi^*(bpy)$ to a $d\sigma^*$ orbital which is anti-bonding in character, $(d\pi)^5(\pi^*)^1 \rightarrow (d\pi)^5(d\sigma^*)^1$. The low lying dd states are close in energy to the emitting MLCT states as shown in Figure 4.1. The dd states can play a significant role in the photochemical and photophysical properties of a complex as they are short lived and their anti-bonding character leads to ligand loss, and decomposition of the complex. However, photochemistry of the dd states can be exploited by Photoinitiated ligand loss for various applications such as

- i. Forming a vacant co-ordination site on a metal oxide for H₂O oxidation,
- ii. Drug delivery (Photodynamic Therapy),
- iii. Exploration of interactions of very labile weak ligands with ruthenium,
- iv. Solar energy conversion,
- v. Molecular switches,
- vi. O₂ and C-H activation.

The *dd* transitions in [Ru(bpy)₃]²⁺ and analogous complexes have not been directly observed since the metal centered transitions are masked by the more intense charge transfer and intraligand transitions. However, the involvement of *dd* states decreases the lifetimes of [Ru(bpy)₃]²⁺ oxidation states as is evident from the study of temperature-dependent emission yields and lifetime measurements.² In order to study the *dd* states of [Ru(bpy)₃]²⁺ extensively, Sutin *et al.*,⁴ generated high-lying excited states through sequential two-photon capture by [Ru(bpy)₃]²⁺ or electron capture by [Ru(bpy)₃]²⁺ as shown in Figures 4.2 and 4.3. The pulse radiolysis experiments suggest that solvated electron capture by [Ru(bpy)₃]²⁺ takes place at close to the diffusion-controlled rate and forms three species. The yields of the ground state complex, ³MLCT excited state and nonemitting transient species were 7, 38 and 55 percent, respectively.⁴

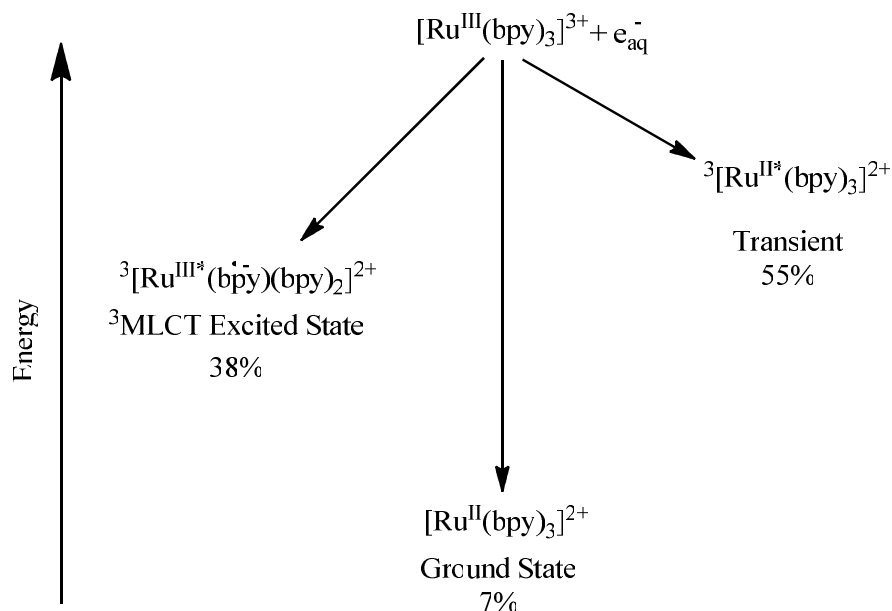


Figure 4.2 Electron capture by [Ru(bpy)₃]²⁺. (Adapted from Reference 4)

However, sequential two photon excitation of [Ru(bpy)₃]²⁺ followed the mechanism shown in Figure 4.3.⁴ In the ground state, [Ru(bpy)₃]²⁺ absorbs a single photon to form the ¹MLCT excited state followed by intersystem crossing to the ³MLCT excited state. The ³MLCT excited state is long-lived and thus there is a significant probability of photon capture using 355 nm excitation to create a higher excited state ³[Ru(bpy^{•-})(bpy)₂]²⁺ that was found to be 5.6 eV above the ground state.

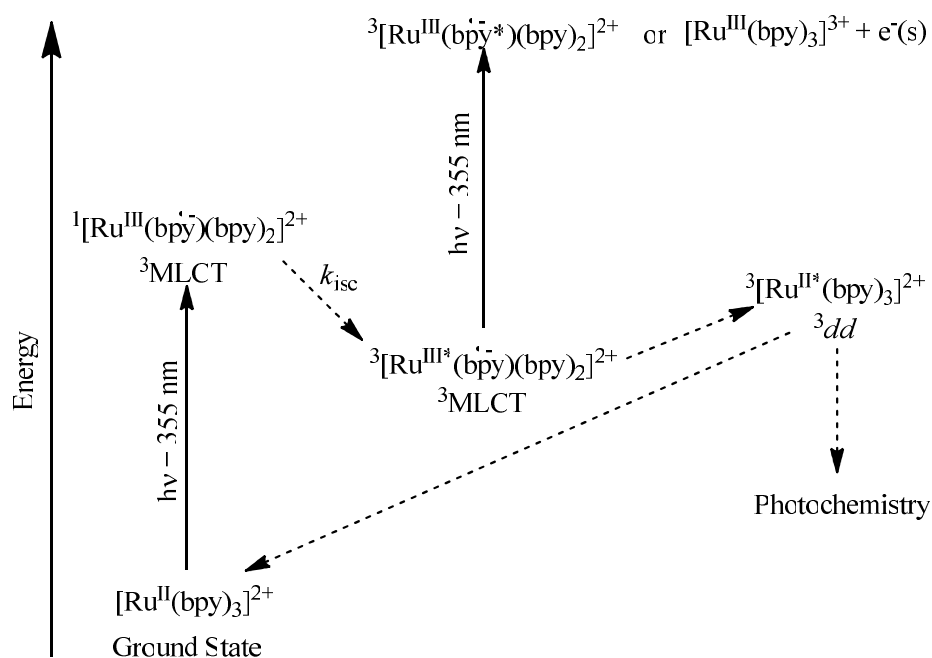


Figure 4.3 Sequential two photo excitation of [Ru(bpy)₃]²⁺. (Adapted from Reference 4)

The deactivation process of the higher lying *dd* excited states (higher than the singlet MLCT excited states) of [Ru(bpy)₃]²⁺ is given in Figure 4.4.

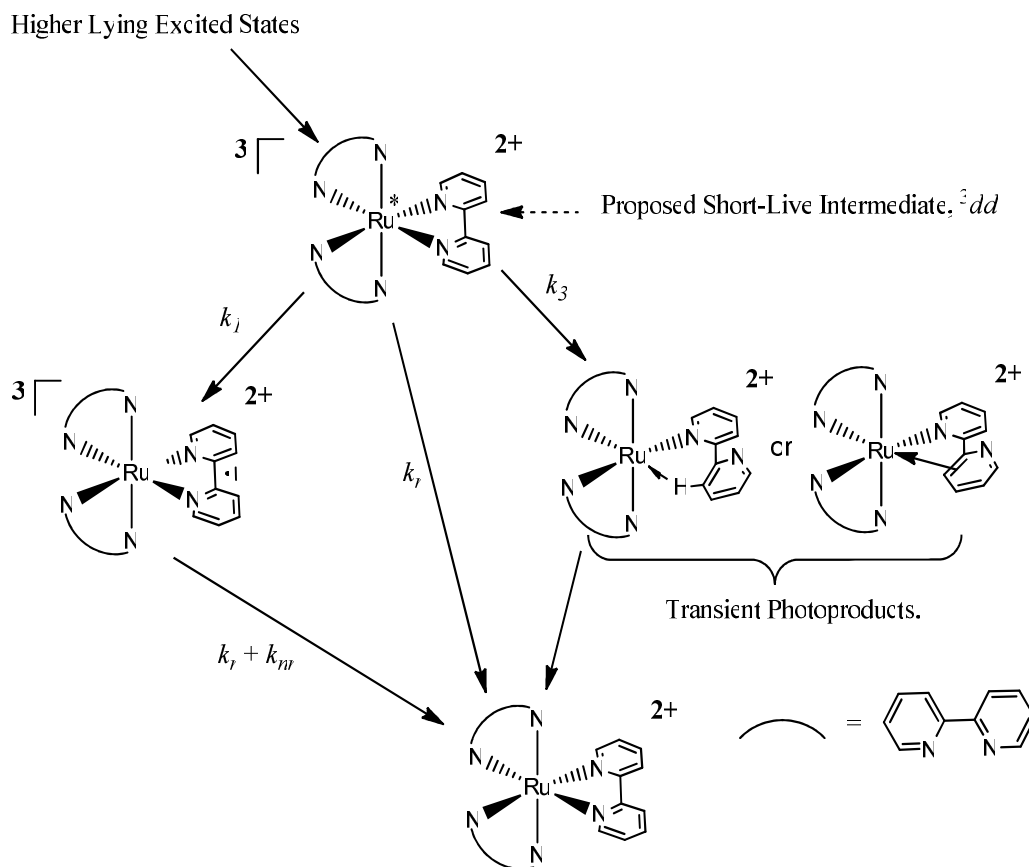


Figure 4.4 Sequential two photo excitation of $[Ru(bpy)_3]^{2+}$.⁴

The deactivation process may take place in three different ways. It may come back through intersystem crossing to the 3MLCT state or directly deactivate to the ground state, or cleavage of a Ru-pyridyl bond may occur together with ligand rearrangement to form $[Ru(bpy)_3]^{2+}$. It was anticipated that the cleavage of a Ru-N bond in $[Ru(bpy)_3]^{2+}$ forms $[Ru(bpy)_2(\eta^1\text{-bpy})]^{2+}$, followed by a pyridyl ring rotation or transient formation of a $[Ru(bpy)_2(\pi\text{-bpy})]^{2+}$ complex where the pendant ring is ligated in an η^1 or π fashion or through a three centered agostic bonding motif, Figure 4.5.⁴

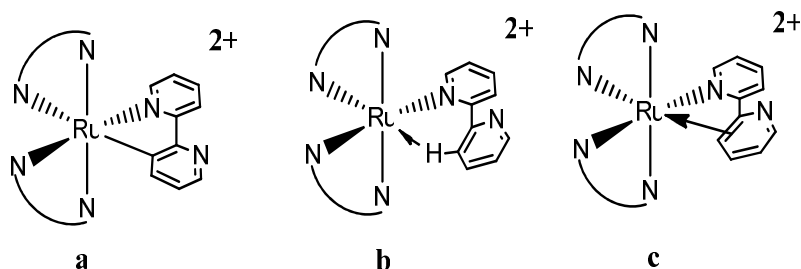
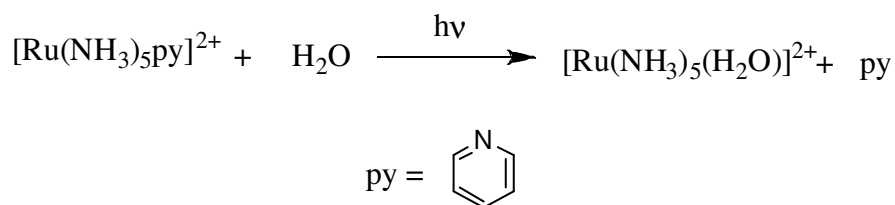


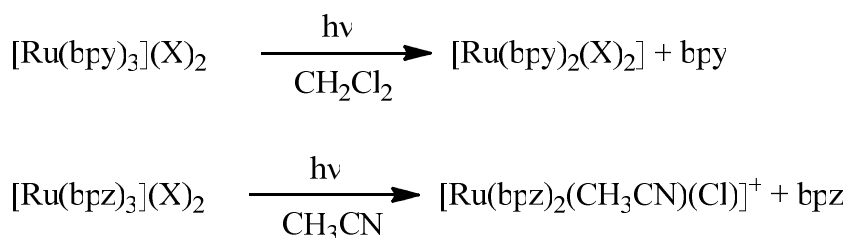
Figure 4.5 Bonding pattern. a) η^1 b) three centred agostic c) π fashion.

Photosubstitution reactions of ruthenium pentaammine complexes $[Ru(NH_3)_5L]^{2+}$ in aqueous solution (where L is a py, substituted pyridine, or a related aromatic nitrogen heterocycle) are well-documented.⁵ Ford *et al.*^{5a} investigated the flash photolysis of ruthenium(II)-amine complexes $[Ru(NH_3)_5(py-X)]^{2+}$ in aqueous solution (where py-X is a substituted pyridine). Irradiation into the visible MLCT band of $[Ru(NH_3)_5(py)]^{2+}$ results in the photosubstitution of pyridine with H_2O (Scheme 4.1). This was evident from the bleaching of the charge transfer absorption band. The complex ion $[Ru(NH_3)_5(H_2O)]^{2+}$ exhibits an intense and broad absorption band at 407 nm due to a MLCT transition.



Scheme 4.1 Photosubstitution reaction of pyridine with H_2O .⁵

The absorption spectra of polypyridyl complexes of Ru(II) are dominated by the MLCT transitions $[\text{Ru}^{\text{II}}(\text{bpy})_3]^{2+} \rightarrow [\text{Ru}^{\text{III}}(\text{bpy})_2(\text{bpy}^{\bullet-})]^{2+}$. However, in the excited state, the appearance of thermally activated low-lying *dd* states results in rapid decay of the excited complex to the ground state or leads to photoinduced ligand loss chemistry as shown in the Scheme 4.2.⁶



Scheme 4.2 Photosubstitution reactions of $[\text{Ru}(\text{bpy})_3]^{2+}$ and $[\text{Ru}(\text{bpz})_3]^{2+}$.⁶

Recently, Turro *et al.*,⁷ reported the direct measurement of ligand exchange kinetics on the picosecond time scale and detected a pentacoordinated Ru(II) intermediate of $[\text{Ru}(\text{bpy})_2(\text{CH}_3\text{CN})_2]\text{Cl}_2$ that is formed upon irradiation. Steady state irradiation of $[\text{Ru}(\text{bpy})_2(\text{CH}_3\text{CN})_2]\text{Cl}_2$ in H₂O results in the replacement of CH₃CN with H₂O and forms a monoaqua complex $[\text{Ru}(\text{bpy})_2(\text{CH}_3\text{CN})(\text{H}_2\text{O})]^{2+}$ which is evident from the changes in the electronic absorption spectrum during the photolysis. The process for the formation of the pentacoordinated Ru(II) intermediate and monoaqua complex $[\text{Ru}(\text{bpy})_2(\text{CH}_3\text{CN})(\text{H}_2\text{O})]^{2+}$ are shown in Figure 4.6. The formation of monoaqua $[\text{Ru}(\text{bpy})_2(\text{CH}_3\text{CN})(\text{H}_2\text{O})]^{2+}$ complex from the pentacoordinated Ru(II) intermediate occurs within 77 ps.

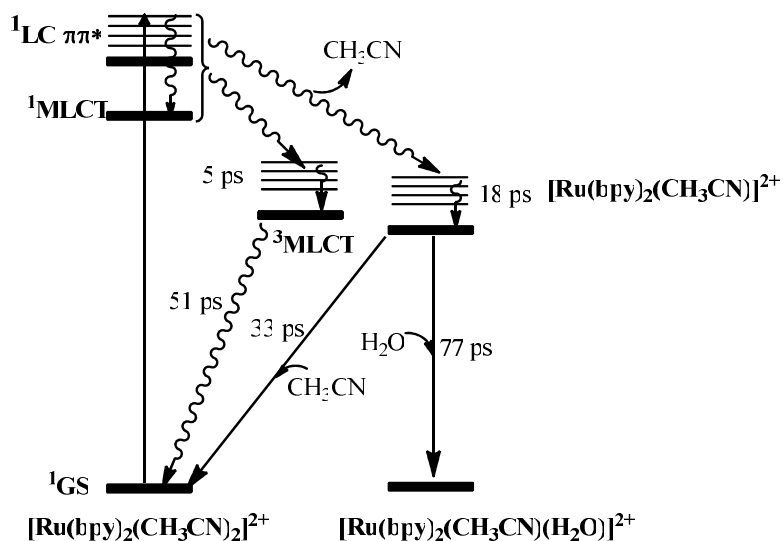


Figure 4.6 Diagram for the ultrafast dynamics of $[\text{Ru}(\text{bpy})_2(\text{CH}_3\text{CN})_2]\text{Cl}_2$ in H_2O . (Adapted from Reference 7).

Similar types of results were obtained from the steady state irradiation of $\text{Ru}(\text{bpy})_2(\text{CH}_3\text{CN})_2\text{Cl}_2$ in CH_3CN which provide additional support for the ligand loss and recombination of $\text{Ru}(\text{bpy})_2(\text{CH}_3\text{CN})_2\text{Cl}_2$ in H_2O as shown in Figure 4.7.

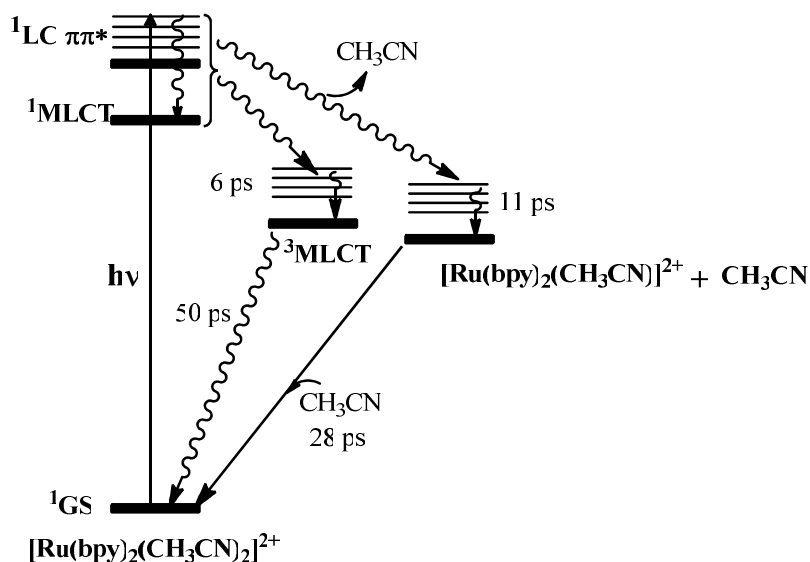


Figure 4.7 Diagram for the ultrafast dynamics of $[\text{Ru}(\text{bpy})_2(\text{CH}_3\text{CN})_2]\text{Cl}_2$ in CH_3CN . (Adapted from Reference 7).

Most recently, Lamberti *et al.*,⁸ introduced a Time-Resolved Wide Angle X-ray Scattering (TR-WAXS) technique to study the photochemistry of $[Ru(bpy)_2(py)_2]Cl_2$. Upon excitation of the MLCT band of $[Ru(bpy)_2(py)_2]Cl_2$, one pyridine ligand is released and consequently a solvent molecule (H_2O) coordinates. The TR-WAXS technique was employed to detect the release of the pyridine ligand and the coordination of the solvent molecule within 800 ns of laser excitation as shown in Figure 4.8.

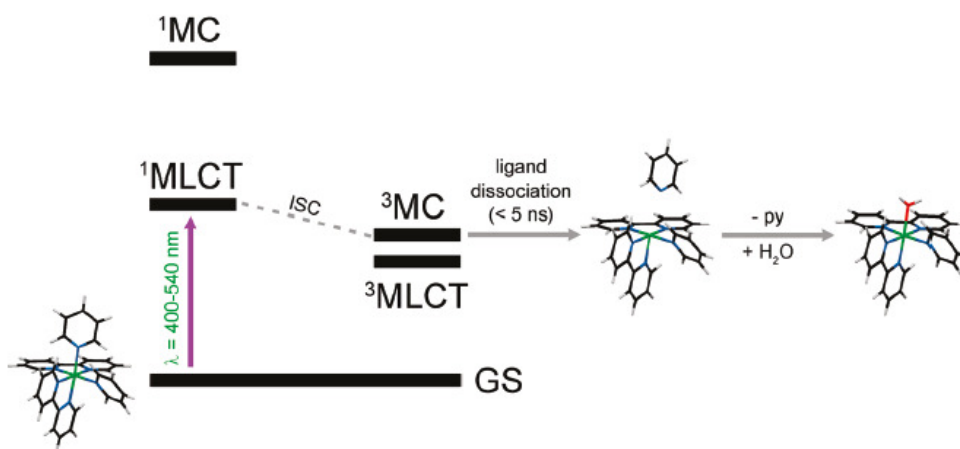


Figure 4.8 Photodissociation scheme for $cis-[Ru(bpy)_2(py)_2]^{2+}$ in H_2O . (Reprinted with permission from reference 8, Copyright © 2010 American Chemical Society).

4.2 Objectives

Ruthenium complexes containing labile ligands have been studied extensively in the field of pharmaceutical chemistry.² They have high intensity metal-to-ligand charge transfer (MLCT) absorption bands and long lived excited states. Upon excitation with visible light, an electron moves to ¹MLCT, followed by an intersystem crossing to ³MLCT through internal conversion due to spin-orbit coupling. Photosubstitution reactions have been reported for *cis*-[Ru(bpy)₂(L)₂]²⁺ (L = py, NH₃, CH₃CN) with H₂O. Here, preliminary results of a flash photolysis study of *cis*-[Ru(bpy)₂(py)₂]²⁺ and [(tpm)Ru(bpy)(py)]²⁺ in THF are reported.

The purposes of our study are as follows:

- i) To study the excited state dynamics of *cis*-[Ru(bpy)₂(py)₂]²⁺ and [(tpm)Ru(bpy)(py)]²⁺ in THF.
- ii) To observe the loss of THF as a ligand in photosubstituted products that can be exploited in O₂ and C-H activation and some other potential applications.
- iii) To compare the results with those that obtained for the previously reported similar types of compounds.

4.3 Results and Discussion

4.3.1 Steady-State Absorption

$Cis-[Ru(bpy)_2(py)_2][PF_6]_2$ and $[(tpm)Ru(bpy)(py)][PF_6]_2$ were prepared according to published procedures as discussed in Chapter 5.

The electronic absorption spectra for $cis-[Ru(bpy)_2(py)_2]^{2+}$ and $[(tpm)Ru(bpy)(py)]^{2+}$, have been previously reported.¹ The absorption spectrum obtained in this work for $cis-[Ru(bpy)_2(py)_2]^{2+}$ in CH_3CN is shown in Figure 4.9.

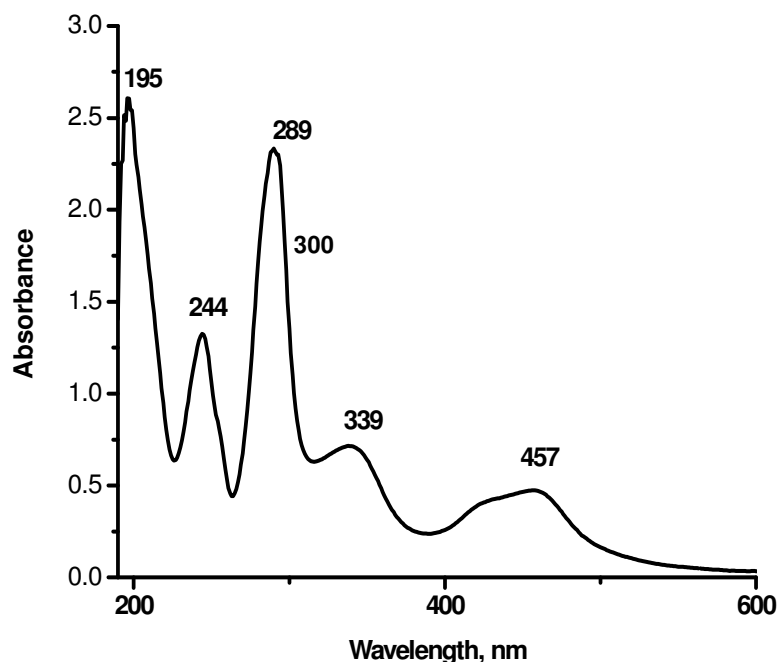


Figure 4.9 Absorption spectrum of $[cis-[Ru(bpy)_2(py)_2][PF_6]_2$ in CH_3CN at 298 (± 3) K.

The absorption spectrum shows $\pi \rightarrow \pi^*$ transitions centred on the bpy ligand that appear at 244 and 289 nm. A shoulder from 300 nm to 350 nm has been assigned to

$n \rightarrow \pi^*$ transitions.² The broad intense absorption in the visible region at 457 nm is due to the metal-to-ligand charge transfer (MLCT) transition.

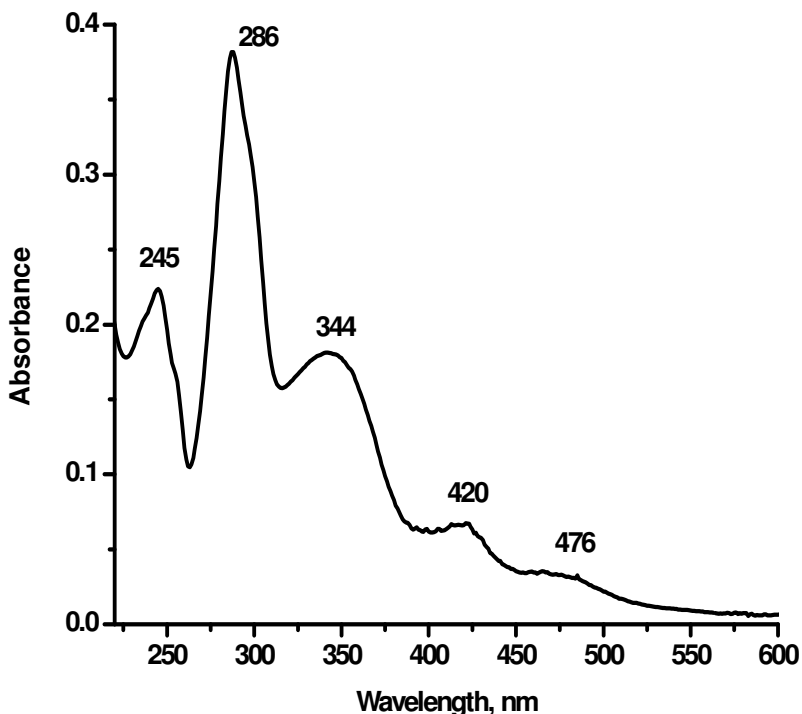


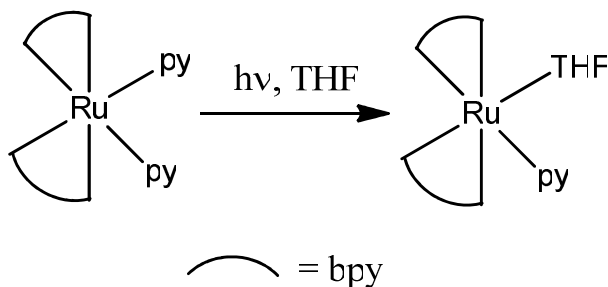
Figure 4.10 Absorption spectrum of [(tpm)Ru(bpy)(py)][PF₆]₂ in CH₃CN at 298 (±3) K.

The absorption spectrum for [(tpm)Ru(bpy)(py)][PF₆]₂ in CH₃CN is shown in Figure 4.10. The absorption spectrum shows a broad band at 344 nm which has been previously assigned⁹ as the overlapping contributions from $d\pi \rightarrow \pi^*$ (tpm), $d\pi \rightarrow \pi^*$ (py), and $d\pi \rightarrow \pi^*$ (bpy) transitions. At higher energies, the spectrum is dominated by $\pi \rightarrow \pi_1^*$ (bpy) and $\pi \rightarrow \pi_1^*$ (tpm), at 286 nm and by a $\pi \rightarrow \pi_2^*$ (bpy) transition at 245 nm. However, the low-energy absorption bands at 420 nm and 476 nm are due to a $d\pi \rightarrow \pi^*$ (bpy) transition which is characteristic of bpy-containing complexes.⁹

At room temperature $cis-[Ru(bpy)_2(py)_2]^{2+}$ is not emissive.¹⁰ On the other hand, significant emission is observed for $[(tpm)Ru(bpy)(py)]^{2+}$ complex.

4.3.2 Photolysis in THF

Spectral changes take place from the photolysis of $cis-[Ru(bpy)_2(py)_2]^{2+}$ in the presence of TFA (4 eq) by using broad band, white light excitation, which leads to a shift in λ_{max} from 458 nm to 472 nm, consistent with the substitution reaction of the pyridine by THF (Scheme 4.3). The product that is formed from the photolysis is monosubstituted, $cis-[Ru(bpy)_2(THF)(py)]^{2+}$ and has an absorption maximum of 472 nm.⁷



Scheme 4.3 Photosubstitution reaction of the pyridine by THF.

Pyridine (4.0 eq) was added with a vision to restore the starting $cis-[Ru(bpy)_2(py)_2]^{2+}$ complex. However, there was no spectral change after adding pyridine. This can be explained by the formation of pyridinium ion in the presence of TFA in solution which prevents the pyridine ligand from replacing THF.

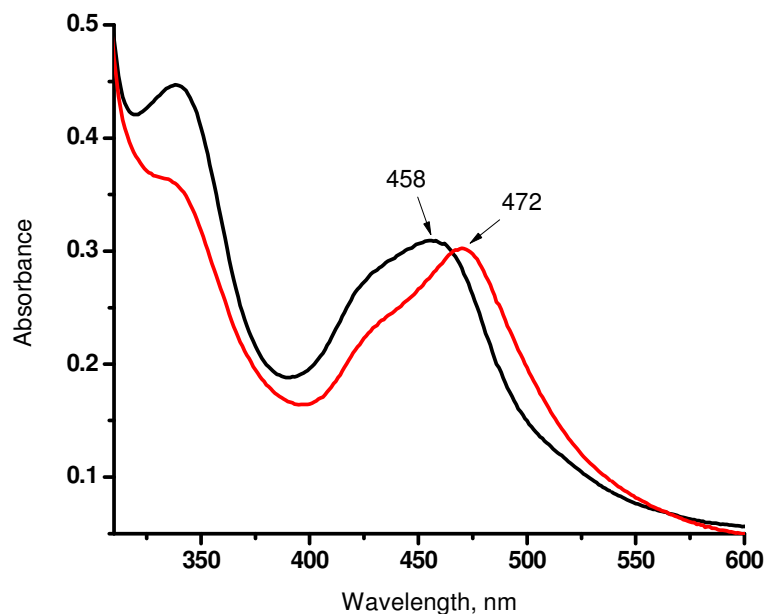


Figure 4.11 Change in absorption spectrum after photolysis of $[Ru(bpy)_2(py)_2]^{2+}$ in presence of TFA(4eq) ; before (black) and after photolysis.

4.3.3 Charge Transfer

Visible spectra of $cis-[Ru(bpy)_2(py)_2]^{2+}$ in the absence and presence of pyridinium ion are shown in Figure 4.12. There is a difference between the low-energy ultraviolet spectral regions in the presence of pyridinium ion which can be attributed to the effect of ion pairing on the intramolecular transitions.¹¹ The low-energy charge transfer (CT) band that is observed at 458 nm is shifted to 476 nm. This is due to the pairing of ions which helps to minimize the energy level which is evident from the spectral change.

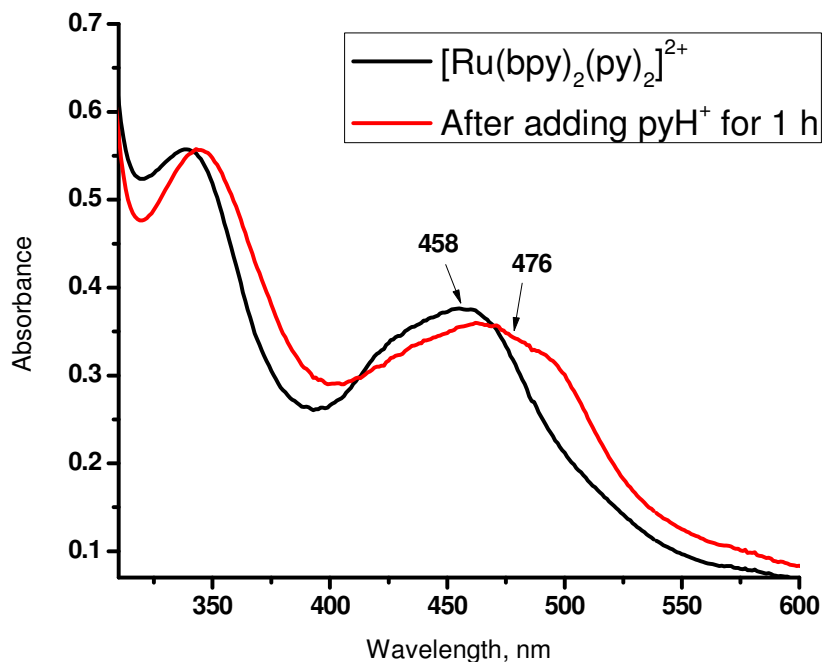


Figure 4.12 Absorption spectra of [Ru(bpy)₂(py)₂]²⁺ (1.2×10^{-5} M); before (black) and after addition of pyridinium ion (pyH⁺).

4.3.4 Flash Photolysis Study

Laser flash photolysis experiments were carried out to investigate the excited state of [Ru(bpy)₂(py)₂]²⁺ in THF. Excitation at different wavelengths was recorded and gave rise to the kinetic traces. Following excitation a very fast bleach and recovery with wavelength dependent amplitude was observed. Exponential decay fits for the kinetic traces of [Ru(bpy)₂(py)₂]²⁺ in THF at $\lambda = 370, 390, 420$ and 450 nm are shown in Figure 4.13.

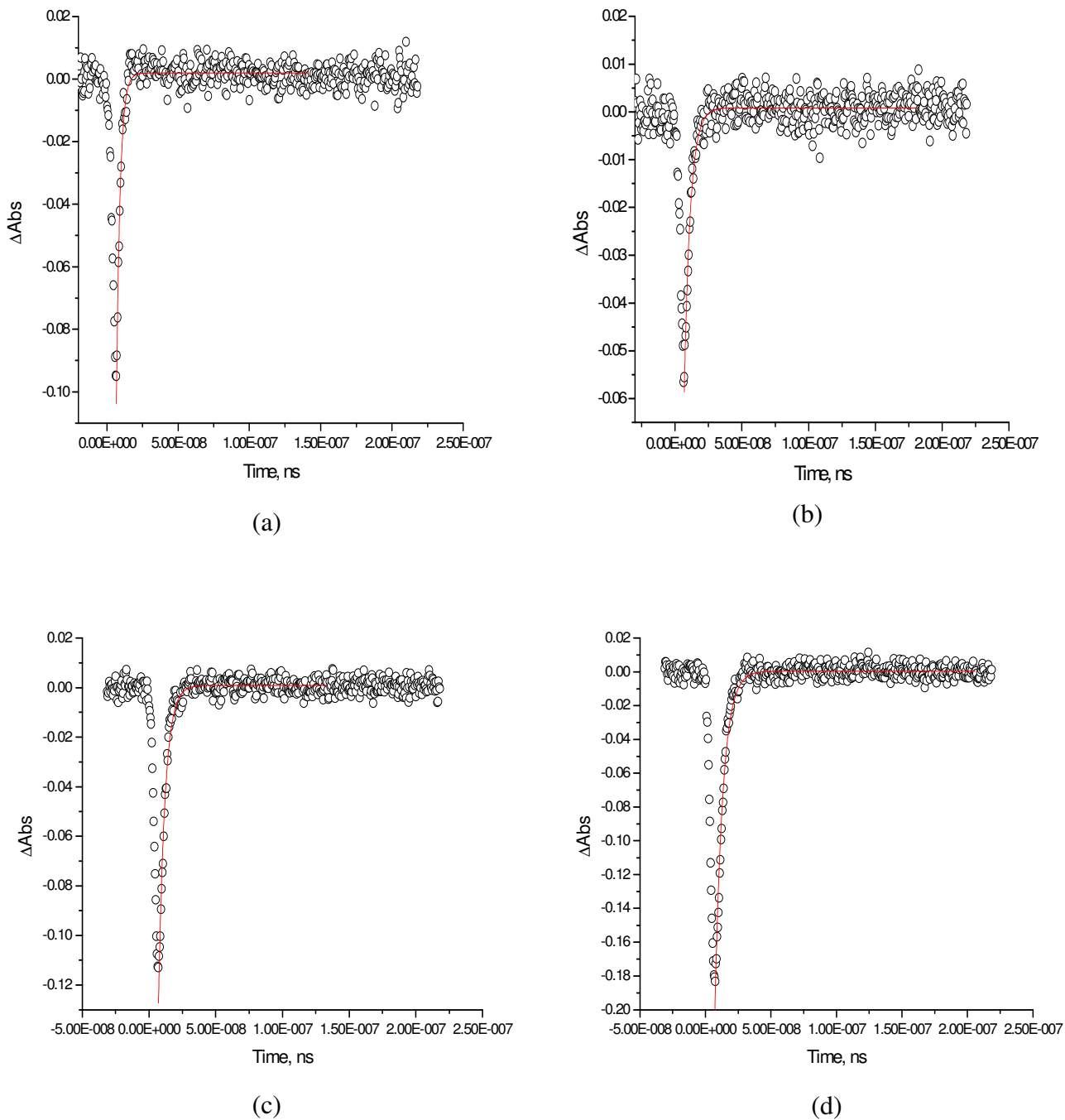
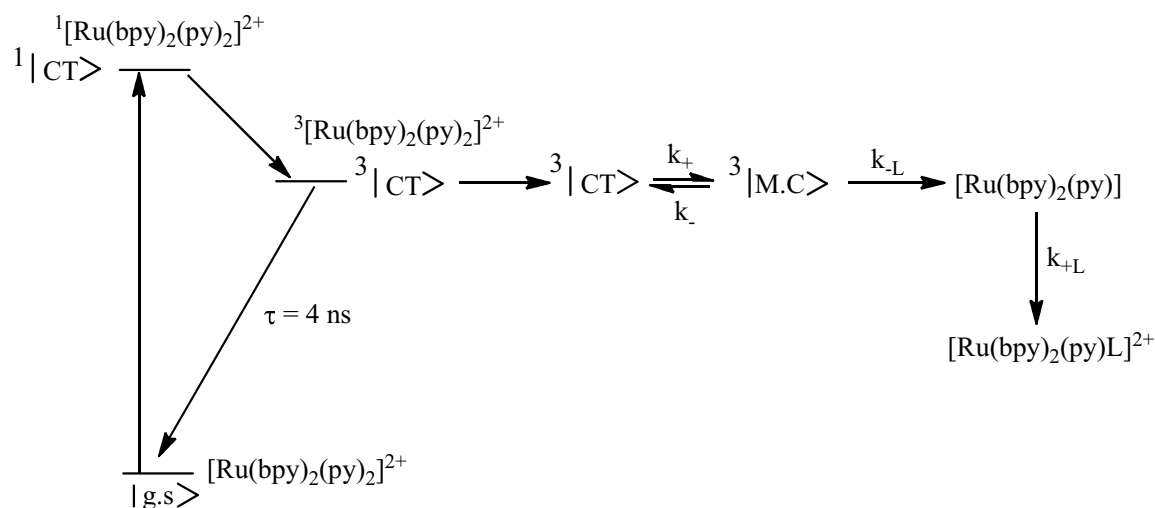


Figure 4.13 Exponential decay fits for kinetic traces of $[\text{Ru}(\text{bpy})_2(\text{py})_2]^{2+}$ in THF at excitation wavelength (a) $\lambda = 370$ nm, (b) $\lambda = 390$ nm, (c) $\lambda = 420$ nm, (d) $\lambda = 450$ nm.

These are the initial results that were obtained from the study of photoinduced ligand loss of [Ru(bpy)₂(py)₂]²⁺. On the basis of these results and review from the literature a mechanism of the excited state reaction of [Ru(bpy)₂(py)₂]²⁺ in THF has been proposed in Scheme 4.4. Following its formation by MLCT excitation and MLCT-*dd* barrier crossing, the *dd* state returns to the MLCT state and then decays to the ground state by a combination of nonradiative decay and ligand loss followed by recoordination.² On the basis of our analysis, decay through this state is comparable in time scale to decay of the MLCT state and they are kinetically coupled. *k*_{dd} represents all decay pathways which deactivate the *dd* excited state. This includes radiative and nonradiative decay (we found no evidence for *dd* emission in our studies) and photoinduced ligand loss. In solution the MLCT-*dd* barrier crossing is irreversible because ligand loss is rapid relative to reverse barrier crossing.²



Scheme 4.4 Proposed mechanism for the photoinduced ligand loss of [Ru(bpy)₂(py)₂]²⁺ in THF.

Similar types of experiments were performed for [(tpm)Ru(bpy)(py)]²⁺. However, we did not get any kinetic traces to report.

4.4 Conclusion

Photoinduced ligand exchange in metal complexes is an emerging field. Here, flash photolysis of [Ru(bpy)₂(py)₂]²⁺ in THF was studied. It has been reported previously that in [Ru(bpy)₂(L)₂]²⁺ (L= py, CH₃CN, NH₃, etc), ligand L gets replaced by the solvent.⁷ The solvent coordinated complexes are labile enough to get replaced by another ligand. In [Ru(bpy)₂(py)₂]²⁺, pyridine was replaced by THF, which is evident from a very fast bleach and recovery with wavelength dependent amplitude in the flash photolysis experiment. Moreover, spectral changes take place from the photolysis of [Ru(bpy)₂(py)₂]²⁺ in THF which is consistent with the substitution reaction of the pyridine by THF.

4.9 References

1. Juris A.; Balzani, V. *Coor. Chem. Rev.* **1988**, *84*, 85.
2. Thompson, D. W.; Fleming, C. N.; Myron, B. D.; Meyer, T. J. *J. Phys. Chem. B* **2007**, *111*, 6930.
3. Meyer, T. J. *Pure & Appl. Chem.* **1986**, *58*, 1193.
4. Thompson, D. W.; Wishart, J. F.; Brunschwig, B. S.; Sutin, N. *J. Phys. Chem. A*, **2001**, *105*, 8117.
5. a) Matsubara, T.; Ford, P. C. *Inorg. Chem.* **1978**, *17*, 1147. b) Durante, V. A.; Ford, P. C. *Inorg. Chem.* **1979**, *18*, 588. c) Hintze, R. E.; Ford, P. C. *Inorg. Chem.* **1975**, *14*, 1211.
6. Durham, B.; Caspar, J. V.; Nagle, J. K.; Meyer, T. J. *J. Am. Chem. Soc.* **1982**, *104*, 4803.
7. Liu, Y.; Turner, D. B.; Singh, T. N.; Angeles-Boza, A. M.; Chouai, A.; Dunbar, K. R.; Turro, C. *J. Am. Chem. Soc.* **2009**, *131*, 26.
8. Salassa, L.; Borfecchia, E.; Ruiu, T.; Garino, C.; Gianolio, D.; Gobetto, R.; Sadler, P. J.; Cammarata, M.; Wulff, M.; Lamberti. *C. Inorg. Chem.* **2010**, *49*, 11240.
9. Barqawi, K. R.; Llobet, A.; Meyer, T. J. *J. Am. Chem. Soc.* **1988**, *110*, 7151
10. Fleming, C. N.; Dattelbaum, D. M.; Thompson, D. W.; Ershov, A. Y.; Meyer, T. J. *J. Am. Chem. Soc.* **2007**, *129*, 9622.
11. Kober, E. M.; Sullivan, B. P.; Meyer, T. J. *Inorg. Chem.* **1984**, *23*, 2098.

Chapter 5 Experimental

This chapter describes the sources of the reagents and the protocols followed for the syntheses of the complexes. The synthesis and purification of all compounds in this thesis have been reported previously. These procedures are included here for completeness. At this juncture it is useful to review the synthetic protocols to illustrate some findings.

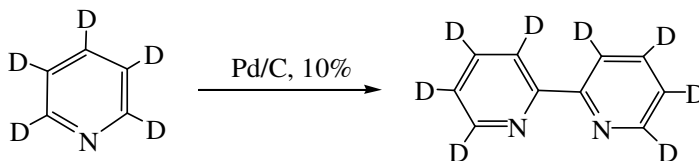
5.1 Review of the Literature

We report here on the polypyridyl complexes of ruthenium based on terpyridine (tpy) and pyridine (py) containing $[\text{Ru}(\text{bpy}-d_8)_2\text{X}]$ and $[\text{Ru}(\text{bpy})_2\text{X}]$ [where X = Cl_2 , tpy, (py) $_2$] chromophoric units:

- a. $[\text{Ru}(\text{bpy}-d_8)_2\text{Cl}_2]$
- b. $[\text{Ru}(\text{bpy}-d_8)_2(\eta^2\text{-tpy})](\text{PF}_6)_2$
- c. $[\text{Ru}(\text{bpy})_2\text{Cl}_2]$
- d. $[\text{Ru}(\text{bpy})_2(\text{py})_2](\text{PF}_6)_2$

Deuteration is a powerful approach that simplifies identification of many complexes.¹ The use of $\text{bpy}-d_8$ as a co-ligand to simplify the identification of complexes is well-established in the literature. In the beginning, we started with a procedure which is time consuming, dangerous and ends up with incomplete deuteration, for the synthesis of $\text{bpy}-d_8$.² Afterwards, a simplified and straightforward procedure was followed where complete deuteration takes place and no high pressure reactors are required.³

Commercially available pyridine- d_5 is refluxed with 10% Pd/C to yield bpy- d_8 through a dedeuteration followed by coupling reaction (Scheme 5.1).³



Scheme 5.1 Preparation of bpy- d_8 .

This process can be made cost effective by recycling the unreacted solvents through distillation and the Pd/C catalyst by removing the ligand by washing. The ^1H NMR spectrum (aromatic region) of bpy- d_8 in CDCl_3 is given in Figure 5.1.

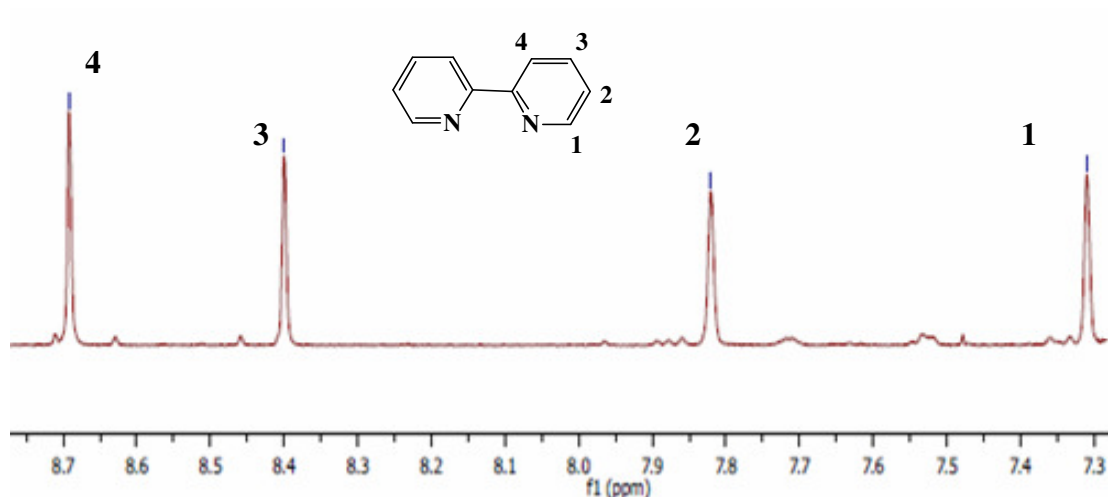
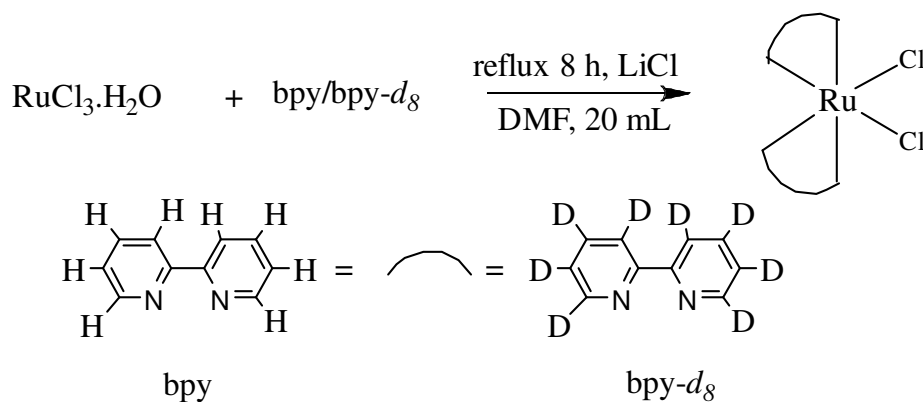


Figure 5.1 500 MHz ^1H NMR spectrum (aromatic region) of bpy- d_8 in CDCl_3 at 298 K.

The ^1H NMR spectrum of bpy- d_8 exhibited four peaks at δ 8.69 (s, 1H), 8.40 (s, 1H), 7.82 (s, 1H), 7.31 (s, 1H) due to protic impurities.

The complexes $[\text{Ru}(\text{L})_2\text{Cl}_2]$ (Where L = 2,2'-bipyridine, 2,2'-bipyridine- d_8) were prepared from the reaction of the ruthenium chloride monohydrate and the coordinating ligand L (Scheme 5.2).⁴

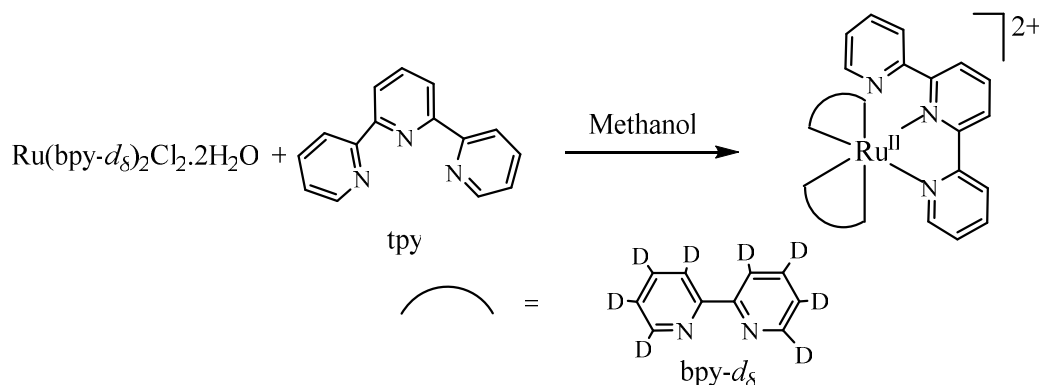


Scheme 5.2 Preparation of $[\text{Ru}(\text{L})_2\text{Cl}_2]$ (Where L = bpy or bpy- d_8).

The structure of $[\text{RuCl}_3] \cdot \text{H}_2\text{O}$ is not known. It exists as a polymer which has never been characterized (taken as 40% ruthenium by mass). In order to suppress the formation of $[\text{Ru}(\text{L})_3]^{2+}$ species, the reaction was carried out in the presence of an excess of chloride ions in the form of LiCl in the reaction. The reaction was carried out in dimethyl formamide (DMF, 97%). The main impurities in DMF are amines (NR_3). However, amine helps to reduce Ru^{III} to Ru^{II} with formation of a putative $[\text{Ru}^{\text{II}}(\text{DMF})_4\text{Cl}_2]$ complex which is extremely labile. Finally, $[\text{Ru}^{\text{II}}(\text{DMF})_4\text{Cl}_2]$ reacts with ligand L (bpy or bpy- d_8) to form $[\text{Ru}(\text{L})_2\text{Cl}_2]$. A common impurity in this reaction is $[\text{Ru}(\text{L})_3]\text{Cl}_2$ which is removed by washing the isolated solid with several aliquots of H_2O as $[\text{Ru}(\text{L})_3]\text{Cl}_2$ is soluble in H_2O and $[\text{Ru}(\text{L})_2\text{Cl}_2]$ is not, followed by diethyl ether. The methanolic solution of $[\text{Ru}(\text{L})_2\text{Cl}_2]$ is red as the -OH group of methanol coordinate with the Cl. However, the solid is purple.

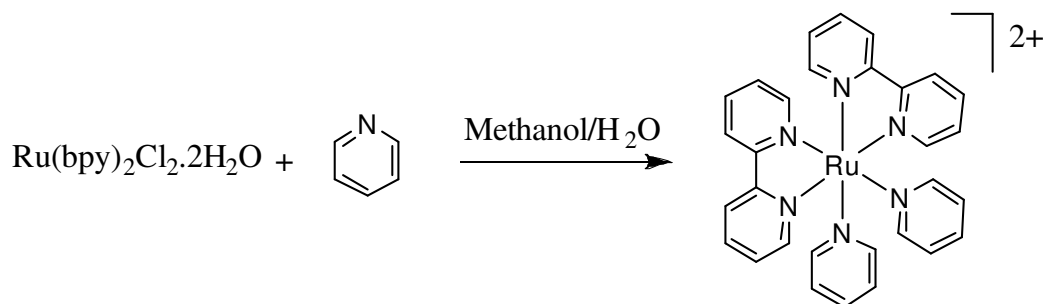
$[\text{Ru}(\text{bpy-}d_8)_2(\eta^2\text{-tpy})]^{2+}$ was prepared from the reaction of $[\text{Ru}(\text{bpy-}d_8)_2\text{Cl}_2]$ and tpy in methanol (Scheme 5.3).⁵ The complex was characterized on the basis of ^1H NMR

spectroscopy, and UV-vis spectroscopic methods. Details have been discussed in Chapters 2 and 3.



Scheme 5.3 Preparation of $[\text{Ru}(\text{bpy-}d_8)_2(\eta^2\text{-tpy})]^{2+}$

Complex $[\text{Ru}(\text{bpy})_2(\text{py})_2]^{2+}$ was prepared from the reaction of $[\text{Ru}(\text{bpy})_2\text{Cl}_2]$ with pyridine in methanol/ H_2O (Scheme 5.4).⁶



Scheme 5.4 Preparation of $[\text{Ru}(\text{bpy})_2(\text{py})_2]^{2+}$.

The ^1H NMR spectrum of *cis*- $[\text{Ru}(\text{bpy})_2(\text{py})_2]^{2+}$ is given in Figure 6.3. The spectrum consists of doublets and triplets as expected. The spectrum shows peaks at δ 8.90 (d, 2H), 8.34 (d, 2H), 8.26 (m, 6H), 8.12 (t, 2H), 7.90 (m, 4H), 7.84 (t, 2H), 7.76 (t, 2H), 7.35 (t, 2H) and 7.28 (t, 4H). Multiplets at δ 8.26 and 7.90 arise due to the overlapping of two doublets and one doublet triplet, respectively.⁶

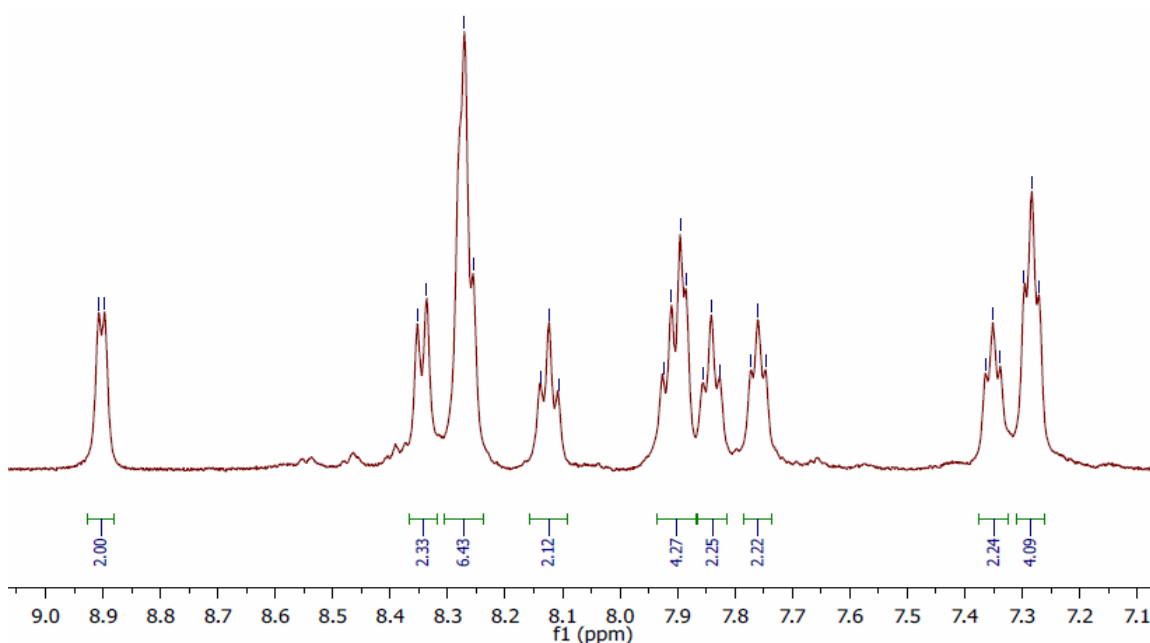


Figure 5.2 ^1H NMR spectrum (aromatic region) of $[\text{Ru}(\text{bpy})_2(\text{py})_2][\text{PF}_6]_2$ in CDCl_3 at 298 K in 500 MHz.

We also prepared compounds containing $[\text{Ru}(\text{tpm})(\text{bpy})\text{X}]^{2+}$ ($\text{X} = \text{Cl}, \text{H}_2\text{O}, \text{py}$) chromophoric units. Here, tris(1-pyrazolyl)methane (tpm) is a tridentate ligand which conforms to a facial geometry at the metal.

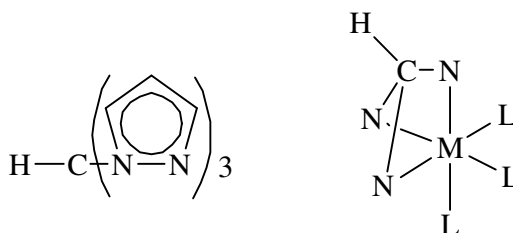
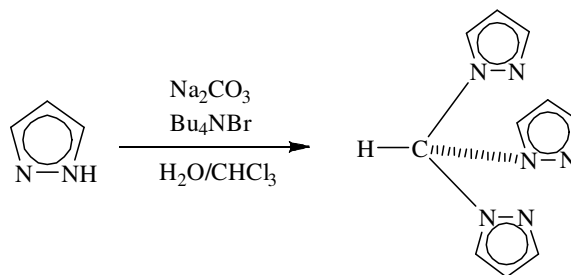


Figure 5.3 Structure of tpm and its geometry.

As part from our program to synthesize the metal complexes of tpm we carefully investigated the preparative procedure of the ligand. The original procedure⁷ was direct reaction of the appropriate pyrazolate and CHCl_3 and for one case, a liquid-liquid phase

transfer condition was used.⁷ However, it has been determined that standard $\text{CHCl}_3\text{-H}_2\text{O}$ phase transfer conditions and replacing the K_2CO_3 with a large excess of Na_2CO_3 , leads to higher yields (60%) and substantially less darkening of the reaction solutions over the 3 days at reflux (Scheme 6.6).



Scheme 5.5 Preparation of tris(1-pyrazolyl)methane (tpm) ligand.

In this reaction tetra-*n*-butylammonium bromide (Bu_4NBr) acts as a phase transfer catalyst. The tpm ligand was characterized on the basis of ^1H NMR spectroscopy (Figure 6.6). The spectrum shows peaks at δ 8.72 (s, 1H), 7.87 (d, 3H for 3-H pz), 7.62 (d, 3H for 5-H pz), 6.40 (m, 3H for 4-H pz). Melting point 101°C .⁷

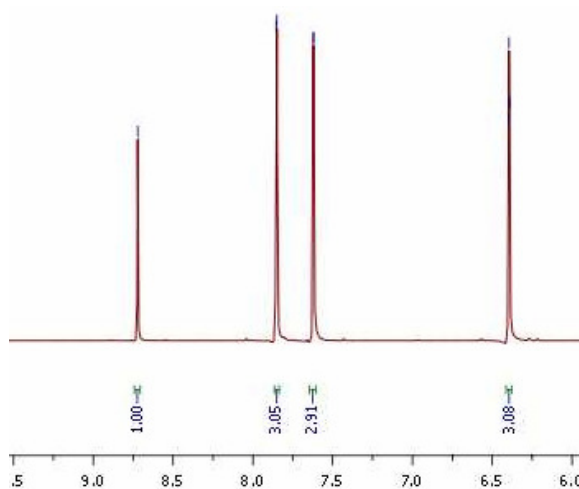
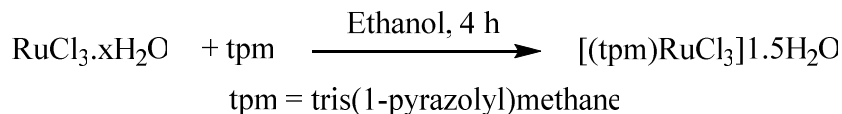


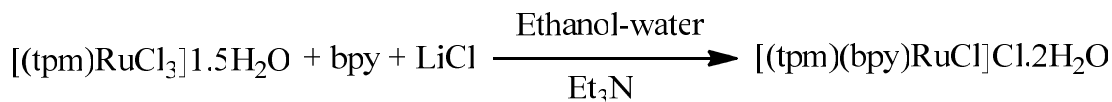
Figure 5.4 ^1H NMR spectrum for tris(1-pyrazolyl)methane in CD_3COCD_3 .

$[(\text{tpm})\text{RuCl}_3]1.5\text{H}_2\text{O}$ was prepared from the reaction of $[\text{RuCl}_3].x\text{H}_2\text{O}$ and tpm in ethanol(Scheme 5.6).



Scheme 5.6 Preparation of $[(\text{tpm})\text{RuCl}_3]1.5\text{H}_2\text{O}$.

Then, $[(\text{tpm})\text{RuCl}_3]1.5\text{H}_2\text{O}$ was heated to reflux with bpy in the presence of LiCl and Et_3N to yield the $[(\text{tpm})(\text{bpy})\text{RuCl}]\text{Cl}.2\text{H}_2\text{O}$ complex in ethanol-water (Scheme 5.7).⁷



Scheme 5.7 Preparation of $[(\text{tpm})(\text{bpy})\text{RuCl}]\text{Cl}.2\text{H}_2\text{O}$.

$[(\text{tpm})(\text{bpy})\text{RuCl}]\text{Cl}.2\text{H}_2\text{O}$ was treated with AgNO_3 and heated at reflux in acetone-water in the absence of light. AgCl was filtered off and NH_4PF_6 was added to the solution which results in formation $[(\text{tpm})(\text{bpy})\text{Ru}(\text{H}_2\text{O})][\text{PF}_6]_2$.⁶



Scheme 5.8 Preparation of $[(\text{tpm})(\text{bpy})\text{Ru}(\text{H}_2\text{O})][\text{PF}_6]_2$.

The ^1H NMR spectrum of $[(\text{tpm})\text{Ru}(\text{bpy})(\text{H}_2\text{O})][\text{PF}_6]_2$ is shown in the Figure 5.5. The spectrum shows peaks at δ 9.47 (s, 1H), 8.72 (d, 2H), 8.56 (d, 2H), 8.45 (d, 2H), 8.25 (m, 1H), 8.21(d, 2H), 8.08 (d, 2H), 7.51 (m, 2H), 6.73 (m, 2H), 6.56 (m, 1H), 6.19 (m, 1H). The singlet at δ 9.47 is due to the methylenic proton. The chemical shifts for tpm and bpy protons appear as reported previously.⁸

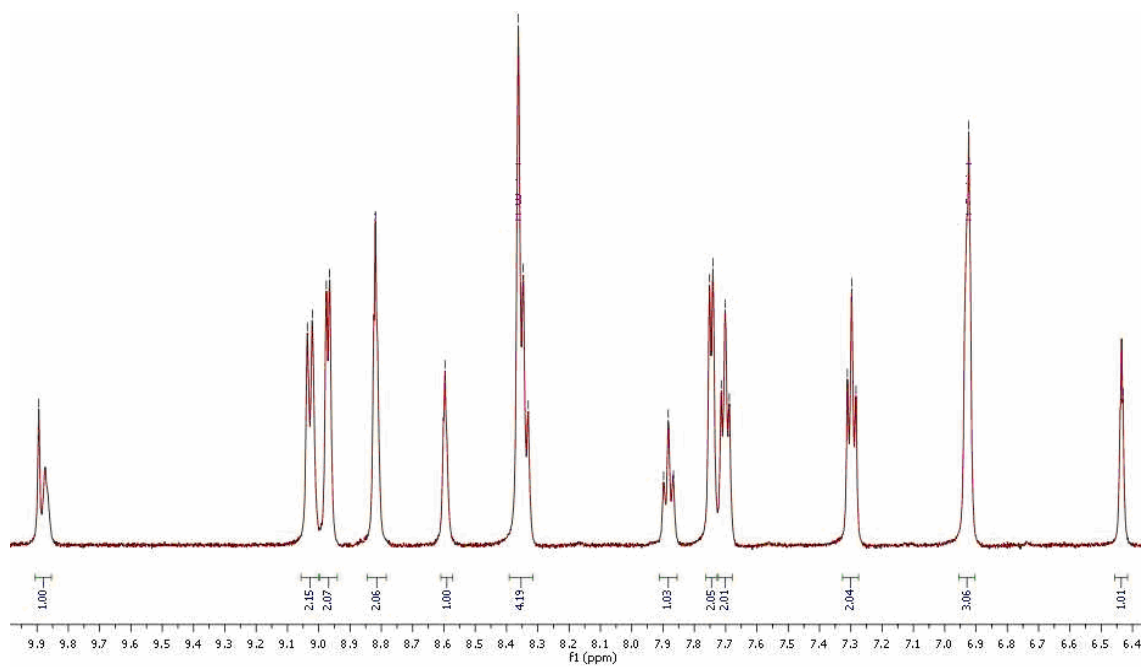


Figure 5.6 ^1H NMR spectrum (aromatic region) of $[(\text{tpm})\text{Ru}(\text{bpy})(\text{py})][\text{PF}_6]_2$ in CD_3COCD_3 at 298 K in 500 MHz.

5.2 Experimental Section

Materials. All reagents purchased were used without further purification. Materials purchased for this work include: Pd/C (Strem Chemicals, 10%), py-d₅ (Sigma-Aldrich, 99 atom %D), RuCl₃.H₂O (Sigma Aldrich), 2,2':6':2"-terpyridine (tpy) (Alfa Aesar, 97%), 2,2'-bipyridine (bpy) (Alfa Aesar, 98%), pyridine (Sigma-Aldrich, 99.5%), ammonium hexafluorophosphate (Alfa Aesar, 99.5%) tetra-n-butyl ammonium bromide [TBA] (Sigma Aldrich, 98%), diethyl ether (ACP, 99.5%) , sodium sulphate (Merck, 99%), chloroform (ACP, 99.8%), NaCO₃ (ACP, 99.5%), hydroquinone (H₂Q) (Fisher Scientific, 99%), Trifluoroacetic acid (TFA)(Sigma Aldrich, 99%), tetrahydrofuran (THF) (Sigma Aldrich, >99.5%), acetonitrile (MeCN)(Burdick and Jackson 98.0%), dimethyl foramide (DMF) and other chemicals were available from previous studies.

Preparations.

bpy-d₈. Pd/C (10%, 1.0 g) was heated in a 500 mL round bottom flask at 150 °C under vacuum for 1 h. Pyridine-d₅ (4 mL, 0.05 mol) was added, and the slurry heated to 140 °C under nitrogen for three days. The excess pyridine-d₅ was removed by vacuum distillation. Then the residual solid was heated at reflux successively in 100 mL each of toluene, chloroform and 10% methanol in chloroform (Volume of the solvents 300 mL), and then filtered while hot. Then the solvents were removed under vacuum to give a brown solid (0.6 g). The solid was purified by flash chromatography (silica gel, 250 mesh; chloroform/MeOH (99% v/v 1%)). Yield: 0.450 g, 5.5%.² ¹H NMR (CDCl₃): δ 8.69 (s, 1H), 8.40 (s, 1H), 7.82 (s, 1H), 7.31 (s, 1H).³

[Ru(bpy-*d*₈)₂Cl₂]. In a 100 mL round bottom flask, RuCl₃.H₂O (0.1 g, 0.19 mmol), bpy-*d*₈ (0.147 g, 0.90 mmol), LiCl (0.7 g) and DMF (20 mL) were heated at reflux for 8 h. Then the reaction mixture was cooled to room temperature and 100 mL of acetone was added. The resultant solution was cooled at 0 °C overnight. The solution was filtered to yield a red to red violet solution and a dark green-black micro-crystalline product. The solid was washed with six 25 mL portions of H₂O followed by three 25 mL portions of diethyl ether, and then dried in vacuo. Yield: 0.075 g, 75% (based on ruthenium).⁴

[Ru(bpy-*d*₈)₂(*η*²-tpy)](PF₆)₂. In a 100 mL round bottom flask, Ru(bpy-*d*₈)₂Cl₂.2H₂O (0.05 g, 0.1 mmol) and tpy were heated at reflux in 15 mL of methanol for 8 h. The colour of the solution changed from red to orange during this period. The solution was filtered and the solvents were removed in vacuo. The product was redissolved in acetone and precipitated with aqueous NH₄PF₆ (0.5 g, 10 mL H₂O). The orange solid was collected by filtration and dried by vacuum pump. Yield: 0.075g, 80%. ¹H NMR (CDCl₃): δ8.59(d, 2H), 8.10 (m, 3H), 7.51 (d, H), 7.33 (d,d 2H), 7.27(t, H), 6.95(t, H), 6.78 (s, H).⁵

[Ru(bpy)₂Cl₂]. In a 100 mL round bottom flask, RuCl₃.H₂O (0.1 g, 0.19 mmol), bpy (0.147 g, 0.90 mmol), LiCl (0.7 g) and DMF (20 mL) were heated at reflux for 8 h. The reaction mixture was cooled to room temperature and 100 mL of acetone was added. The resultant solution was cooled at 0 °C overnight. The solution was filtered to yield a red to violet solution and a dark green-black micro-crystalline product. The solid was

washed with three 25 mL portions of H₂O and three 25 mL portions of diethyl ether, and then dried by suction. Yield: 0.075 g, 75% (based on starting ruthenium).⁴

[Ru(bpy)₂(py)₂](PF₆)₂. A mixture of Ru(bpy)₂Cl₂·2H₂O (0.1 g, 0.103 mmol) and pyridine (0.2 mL) in methanol/H₂O was heated to reflux for 2 h. The bright orange solution was filtered and the product was precipitated with the addition of an excess of aqueous NH₄PF₆. Yield: 0.075 g, 75% (on the basis of starting ruthenium). ¹H NMR (CDCl₃): δ 8.90 (d, 2H), 8.34 (d, 2H), 8.26 (m, 6H), 8.12 (t, 2H), 7.90 (m, 4H), 7.84 (t, 2H), 7.76 (t, 2H), 7.35 (t, 2H) and 7.28 (t, 4H).⁶

Tris(1-pyrazolyl)methane (tpm). 30 mL distilled water was taken in a 250 mL round bottom flask containing a mixture of pyrazole (2.0 g) and tetra-n-butylammonium bromide (0.47 g). Sodium carbonate (18.7 g) was added gradually to the reaction mixture with vigorous stirring. Chloroform (14.5 mL) was added to the reaction mixture after cooling the solution near to room temperature. Then the flask was equipped with a reflux condenser and heated at gentle reflux for 3 days. The colour of the mixture turned pale yellow during this period. The mixture was allowed to cool to room temperature and filtered through a Buchner funnel to remove excess base. The filtrate was treated with diethyl ether (50 mL) and H₂O (30 mL). The combined organic layer was separated and the aqueous layer extracted with diethyl ether (20 mL × 3). The combined organic layer was treated with charcoal and dried over sodium sulfate. The mixture was filtered and the solvent removed by rotary evaporator. The resulting pale yellow solid was dried under vacuum. Yield: 1.20 g, 60%. ¹H NMR (CD₃COCD₃): δ 8.72 (s, 1H), 7.87 (d, 3H for 3-H pz), 7.62 (d, 3H for 5-H pz), 6.40 (m, 3H for 4-H pz). Melting point 101°C.⁷

[(tpm)RuCl₃]1.5H₂O. RuCl₃.xH₂O (1.00 g) and tpm (0.82 g) were taken in 500 mL round bottom flask and heated to reflux for 4 h in 350 mL of absolute ethanol. The color of the solution turned brown during this period. The greenish brown solid was filtered in Buchner funnel, washed with absolute ethanol and acetone and air dried. Yield: 1.28 g, 71%.⁷

[(tpm)(bpy)RuCl]Cl.2H₂O. [(tpm)RuCl₃]1.5H₂O (0.25 g) and bpy (0.10 g) were heated to reflux for 5 min in 50 mL of ethanol-water (3:1) containing 0.25 g of LiCl. 6 drops of NEt₃ were added and the solution was heated to reflux for another 10 min. The brown solution was filtered hot. The volume of the solution was reduced to 15 mL in rotary evaporator and chilled overnight. The resulting brown crystals were collected in a Buchner funnel, washed with a minimum amount of cold water and air dried. Yield: 0.16 g, 42%.⁸

[(tpm)Ru(bpy)(H₂O)][PF₆]₂. [(tpm)(bpy)RuCl]Cl.2H₂O (0.10 g, 0.17 mmol) and AgNO₃ (0.05 g, 0.294 mmol) were heated at reflux for 2 h in 20 mL of acetone-water (3:1) under dark. AgCl was filtered off and NH₄PF₆ (0.50 g) was added to the solution. The volume of the mixture was then reduced in a rotary evaporator and kept into refrigerator for overnight. The resulting orange crystals were filtered, washed with a small amount of cold water and air dried.⁶ ¹HNMR (D₂O): δ 9.47 (s, 1H), 8.72 (d, 2H), 8.56 (d, 2H), 8.45 (d, 2H), 8.25 (m, 1H), 8.21(d, 2H), 8.08 (d, 2H), 7.51 (m, 2H), 6.73 (m, 2H), 6.56 (m, 1H), 6.19 (m, 1H).⁸

[(tpm)Ru(bpy)(py)][PF₆]₂. 0.05 g of [(tpm)(bpy)Ru(H₂O)][PF₆]₂ was dissolved in 20 mL of a 0.1 M NH₄PF₆ ethanolic solution. 3 mL of pyridine was added to that

solution and refluxed for 6 h under nitrogen. Then the solution was cooled down to room temperature and 5 mL of distilled water was added. The volume of the solution was reduced on a rotary evaporator until orange crystalline solid began to form. The solid was filtered and washed with water (3 x 10 mL). Yield: 0.06 g, 70%. $^1\text{H NMR}$ (CD_3COCD_3): δ 9.75 (s, 1H), 8.75 (d, 2H), 8.51(t, 1H), 8.16 (dd, 4H), 8.02(s, 2H), 7.87 (d, 3H), 7.78 (d, 2H), 7.32 (t, 2H), 6.99 (d, 1H), 6.84(t, 2H), 6.81(dd, 2H), 6.51(d, 2H), 6.48 (t, 1H).⁸

5.3 Sample Preparation

The following protocols were carried out for all excited state measurements.

i) The absorption spectrum of the solvent was obtained using air as a reference. This allowed assessing the absorbing impurities of the solvent.

ii) Emission spectra of the solvent were obtained (to note emitting impurities), using 2-3 excitation wavelengths from 320 to 600 nm, depending on the nature of the chromophores.

iii) After screening the solvent, the sample was dissolved and the absorption spectrum was obtained. The absorption spectra for air sensitive samples were obtained after purging with N_2 .

iv) Emission spectra of the compound in the solvent.

v) UV/vis spectra were taken after laser flash photolysis experiments to monitor the integrity of the sample.

Thus, the procedure allows less time expended for trouble shooting for anomalous behaviour during analysis of the data. All the samples were prepared gravimetrically and

dissolved in the solvents using the above mentioned procedure. The samples were purged by N₂ (99.9%) for 5 minutes. UV-vis spectra were taken before and after data acquisition to ascertain that the sample did not degrade during the course of the experiment.

5.4 Measurements

Steady-State Techniques.

UV-Vis. Absorption spectra were acquired using an Agilent 8543 diode array spectrophotometer with a wavelength range from 190 to 1100 nm interfaced to a computer. Data analysis and manipulation of spectra were carried out using Chem-Station software provided by Agilent. A 1 cm path length UV-vis quartz cuvette, supplied by Starna was used for all measurements.

Emission Spectroscopy. Emission spectra were recorded using a Photon Technology International (PTI) Quantummaster 6000 emission spectrometer. The source of excitation energy was a 175 USH10 Xenon arc lamp. The emitted energy was collected at 90° to the excitation source and detected by a Hamamatsu R-928 photomultiplier tube (PMT) in photon counting mode. The measurements were recorded using high-quality quartz fluorescence cells.

Emission Lifetimes. The PTI laser subsystem equipped with N₂ GL-3000 laser (fundamental line at 337.1 nm) was used as the excitation source. Data collection was accomplished using a proprietary stroboscopic technique which requires a 40 ns delay time provided by a 40 foot fiber optic delay line. The intensity vs. time profiles are collected in a manner similar to a box car data acquisition system. The time intervals for

data integration are computer controlled; and the kinetic trace is a histogram of the photons emitted per time interval at set time delays. The stroboscopic technique then allows acquisition of decay data that occurs within the laser pulse. The pulsewidth of the N₂ laser is 450 ± 50 ns on a shot per shot basis. The integration coupled to prior acquisition of a high quality instrument response function (IRF) allows for the deconvolution of $\tau < 400$ ps to be extracted from the data.

The timing of the laser pulse and data acquisition was performed using a Stanford Research System Model DG535 four-channel digital delay pulse generator. Kinetic analysis of the lifetime data was accomplished using software provided by PTI or was exported and fit using Origin software. The IRF data were collected prior to data acquisition for the sample by use of a scattering solution (coffee mate in water).

Transient Absorption. The excitation source of the instrument utilized the third harmonic of a Q-switched Quanta-Ray Brilliant B DCR-2A Nd-TAG (neodymium-doped yttrium aluminum garnet) laser that generates pulses of light at 355 nm with duration of 8 ns. The time-resolved transient absorption signals were acquired using pulse laser excitation from a Quantel Brilliant B laser coupled to a tripling NLO crystal, for 355 nm (8 ns pulse width; 5-10 mJ/pulse; 20 Hz) pulsed excitation. The probe beam was oriented 90° to the excitation source.

NMR Spectroscopy. NMR spectra were recorded on a Bruker AVANCE 500 MHz spectrometer and references to residual protons in the deuterated solvent.

Infrared Spectroscopy. Infrared spectra were recorded as KBr pellets on a Bruker Tensor 27 FT-IR spectrometer.

5.5 References

1. Parker, C. A.; Rees, W. T. *Analyst (London)* **1960**, *85*, 857.
2. Cook, J.; Lewis, A. P.; McAuliffe, G. S. G.; Skarda, V.; Thomson, A. J.; Glasper, J. L.; Robbins, D. J. *J. Chem. Soc., Perkin. Trans.*, **1984**, 1293.
3. Glazer, E. C.; Belyea, B.; Tor Y., *Inorg. Chem. Commun.*, **2005**, *8*, 517.
4. Sullivan, B. P.; Salmon, D. J.; Meyer, T. J. *Inorg. Chem.*, **1978**, *17*, 3334.
5. Chotali, R.; Constable, E. C.; Hannonbn, M. J.; Tocher, D. A. *J. Chem. Soc. Dalton Trans.* **1995**, 3571.
6. Dwyer, F. P.; Goodwin, H. A.; Gyarfas, E. C. *Aus. J. Chem.*, **1963**, *16*, 544.
7. Reger, D. L.; Grattan, T. C.; Brown, K. J.; Little, C. A.; Lamba, J. J. S.; Rheingold, A. L.; Sommer, R. D. *J. Organomet. Chem.* **2000**, *607*, 120.
8. Barqawi, K. R.; Llobet, A.; Meyer, T. J. *J. Am. Chem. Soc.* **1988**, *110*, 7151.

Chapter 6 Future Work

Following the investigations illustrated in chapter 2 & 3 regarding $[\text{Ru}(\text{bpy})_2(\eta^2\text{-tpy})]^{2+}$, a number of projects can be carried out as mentioned below

- i. Further study can be done with derivatized tpy ligands in $[\text{Ru}(\text{bpy})_2(\eta^2\text{-tpy})]^{2+}$ which will allow comparative studies of the dynamic behaviour of tpy in $[\text{Ru}(\text{bpy})_2(\eta^2\text{-tpy})]^{2+}$. This might help to extend studies on the electron transfer, charge transfer and many types of catalytic reactions.
- ii. Photophysical investigation of derivatized $[\text{Ru}(\text{bpy})_2(\eta^2\text{-tpy})]^{2+}$ complexes may open a new arena in PCET reactions as these complexes have free nitrogen in the pendant tpy.

Secondly, the possibility of driving long-range energy-transfer processes in complexes of high nuclearity is a subject of current interest.

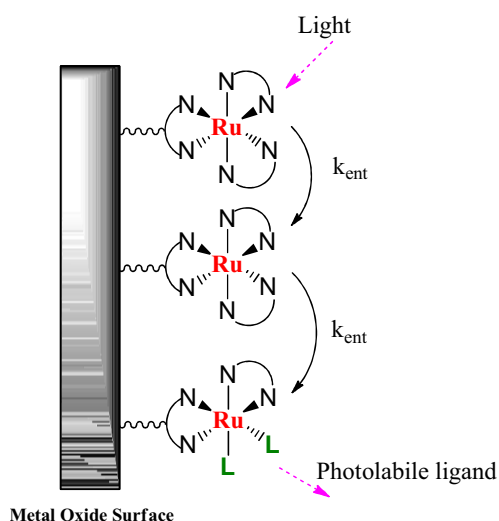


Figure 6.1 Sensitization of photolabile complexes via energy transfer.

Excited state ligand loss can create a co-ordinatively unsaturated metal complex for photo-redox catalysis, O₂ activation, production of H₂ from H₂O, CH₄ from CO and energy storage as shown in Figure 6.1. Photoinduced ligand loss of [Ru(bpy)₂(py)₂]²⁺ may play an important role in this regard. A long range future goal of this research project is the sensitization of photolabile complexes via energy transfer from antenna chromophores on metal oxide surfaces. These assemblies would find utility in creating catalytic sites for eletrocatalysis of substrates under bias conditions.

.....**O**.....